DIPOLAR RECOUPLING AND DECOUPLING IN SOLID STATE NUCLEAR MAGNETIC RESONANCE SPECTROSCOPY

by

Andrew E. Bennett

B. A. Chemistry
Wesleyan University (1986)

Submitted to the Department of Chemistry
in Partial Fulfillment of the Requirements for the
Degree of

DOCTOR OF PHILOSOPHY
in Chemistry
at the

Massachusetts Institute of Technology

September 1995

Signature of Author _____
Department of Chemistry
July 11, 1995

Certified by _____
Professor Robert G. Griffin
Thesis Supervisor

Accepted by _____
Professor Dietmar Seyferth
Chairman, Departmental Committee on Graduate Students

This Doctoral thesis has been examined by a Committee of the Department of Chemistry as follows:

Professor John S. Waugh _____
Chairman

Professor Robert G. Griffin _____
Thesis Supervisor

Professor Robert W. Field _____

Dipolar Recoupling and Decoupling in Solid State Nuclear Magnetic Resonance Spectroscopy

by
Andrew Ernest Bennett

Submitted to the Department of Chemistry
on July 11, 1995 in partial fulfillment of the
requirements for the Degree of Doctor of Philosophy

Abstract

In solid state nuclear magnetic resonance spectroscopy, the magic angle spinning technique is often used to remove anisotropic interactions and generate high resolution spectra. However, these interactions contain valuable information about molecular structure and dynamics. In particular, the dipole-dipole coupling strength between two spin-1/2 nuclei is a direct reflection of their interatomic distance.

Two ways of recoupling dipolar interactions into spinning experiments are explored here. In the first, longitudinal dipolar exchange experiments employing spin echoes are examined in homonuclear spin systems. The accurate measurement of internuclear distances is demonstrated for spin pairs. Two-dimensional exchange spectroscopy using π pulses is applied to the retinal conformations in dark-adapted bacteriorhodopsin and the relationship between the retinal chromophore and the neighboring aspartic acid residues. The distance of the retinal-14 position in light-adapted bacteriorhodopsin to the aspartic acid-212 sidechain is also established within less than 5.5 Å using spin diffusion experiments.

A second dipolar recoupling experiment involves the frequency-selective reintroduction of heteronuclear interactions among spin-1/2 nuclei. This approach is designed to examine weak dipolar interactions in a multiple spin environment, where it is desirable to isolate the influences of individual couplings.

Simulations including losses of spin coherence within an exponential model are introduced for both the homonuclear and heteronuclear techniques. A theoretical framework for understanding compensation for pulse imperfections in multiple pulse echo sequences is presented, and the effect of insufficient proton decoupling on dilute spins is also discussed.

Finally, a simple phase modulation scheme is introduced for heteronuclear spin decoupling in rotating solids, yielding improved linewidths over those obtained with continuous-wave decoupling under

typical conditions. The influence of magic angle spinning on continuous wave and composite pulse decoupling is also investigated.

Thesis Supervisor: Dr. Robert G. Griffin

Title: Professor of Chemistry and Director of the Francis Bitter National Magnet Laboratory

This thesis is dedicated to my wife,
Michelle Heller

Table of Contents

Acknowledgements

Above all, I would like to thank my wife, Michelle Heller, for all of her support and assistance during my graduate career. It is extraordinary how much she has done to help me with graduate school and to contribute to my happiness during some of the difficult challenges.

I am also very grateful for the support and advice which I have received from my research supervisor, Professor Bob Griffin. In his laboratory, I have had a wonderful opportunity to enter a new area of research and to participate in an exceptionally interesting and significant field of study.

Also, I have greatly benefited from my interactions with Professor Shimon Vega during my years at MIT, and I have learned much about many areas of NMR spectroscopy, as well as theoretical methods (especially Floquet Theory), from him.

Many current and former members of the Griffin group, as well as several staff members at the Francis Bitter National Magnet Laboratory, have been extremely helpful to me during my stay at MIT. Some of the group members whom I would especially like to thank are Janet Griffiths, Chad Rienstra, Michèle Auger, K. V. Lakshmi, Lino Becerra, Joanna Long, Doug Maus, Ken Fishbein, and Brendan Bellew.

Recently, I have particularly enjoyed working with Chad on the problem of decoupling in solids and Janet on the application of 2D dipolar correlation experiments to bacteriorhodopsin. Lakshmi and Michèle originally demonstrated many of the basic procedures in solid state NMR spectroscopy to me when I was a new member, and their assistance was very helpful to me and greatly appreciated. Ken Fishbein also provided me with much assistance and information along the way.

I have also greatly benefited from working on projects with many other current and former Griffin group members, as well as just socializing and talking about science or personal matters. The diversity of backgrounds and research interests within the group has made it possible for me to learn about a variety of topics in solid state NMR spectroscopy, as well as its applications to biophysical problems.

The assistance and support of Dr. David Ruben, Ajay Thakkar, Peter Allen, and Jim Wrenn with instrumentation and technical support are greatly appreciated. I have also learned a great deal about the technical aspects of NMR spectroscopy from them during the course of my research efforts.

The opportunity to study at MIT has been a tremendous one, and as one faculty member put it, it is "the most overstimulating environment" in which I have ever worked. That is to say, I have not only learned a lot about magnetic resonance and physical chemistry, but I have also been exposed to areas of science and engineering which I had never even heard of before attending MIT. For somebody who is interested in the scientific and technical realm, and who likes to be surrounded by talented and challenging people, I cannot imagine that there is a better place.

Finally, I would like to acknowledge the support of a predoctoral fellowship from the National Science Foundation. The research discussed in this thesis has also been supported by grants RR-00995, GM-23403, GM-36810, GM-23289, and GM-25505 from the National Institutes of Health.

List of Abbreviations

AHT	Average Hamiltonian Theory
CP	Cross Polarization
CPMAS	Cross Polarization Magic Angle Spinning
CS	Chemical Shift
CSA	Chemical Shift Anisotropy
CW	Continuous-Wave
DA	Dark-adapted
DD	Dipole-dipole
DIPSHIFT	Dipolar Chemical Shift Correlation Spectroscopy
FDR	Frequency-Selective Dipolar Recoupling
FID	Free Induction Decay
FTIR	Fourier Transform Infared Spectroscopy
FWHM	Full Width at Half Maximum
LA	Light-adapted
MAS	Magic Angle Spinning
MW	Maricq and Waugh
NMR	Nuclear Magnetic Resonance
1D	One-dimensional
PAS	Principal Axis System
ppm	parts per million
R2	Rotational Resonance
R3	Rotary Resonance Recoupling
REDOR	Rotational Echo Double Resonance
RF	Radio-Frequency
RFDR	Radio-Frequency Dipolar Recoupling
SEDOR	Spin Echo Double Resonance
SEDRA	Simple Excitation for the Dephasing of Rotational Echoes
SLF	Separated Local Field
2D	Two-dimensional
ZQ	Zero-Quantum

Introduction

The magnetic dipole-dipole coupling between two nuclear spins, which reflects their interatomic separation, can be measured using solid state nuclear magnetic resonance (NMR) techniques. In this thesis, two ways of reintroducing dipolar interactions into magic angle spinning (MAS) experiments on polycrystalline samples are explored. In the first study, longitudinal exchange experiments employing rotor-synchronized spin echo sequences are examined as a means of observing dipolar evolution in two spin and multiple spin systems. Average Hamiltonian Theory (AHT) within a double toggling frame approach is applied to the analysis of homonuclear dipolar recoupling with π pulse sequences. The two-dimensional version is demonstrated by experiments which reveal the retinal chromophore conformations in dark-adapted bacteriorhodopsin (bR) and provide qualitative confirmation of the relationships between the aspartic acid-212 and -85 residues and the chromophore. The proximity of the aspartic acid-212 residue (i. e. ≤ 5 Å) to the retinal-14 position in light-adapted bacteriorhodopsin is also confirmed with spin diffusion experiments and is in agreement with the Henderson model for the structure of bR.

It is also shown that the π pulse exchange approach is suitable for the measurement of internuclear distances up to at least 4.6 Å for ^{13}C-^{13}C spin pairs under favorable conditions. Analysis of the data is performed using a simulation algorithm which includes the combined influences of magic angle spinning and periodic radio-frequency (RF) pulse excitations, while an exponential model for the decay of all spin coherences is included in the spin dynamics simulations. The latter capability is necessary because of the signal losses arising from various incoherent effects, the most important of

which is the decay of spin coherences from insufficient proton decoupling power during the application of multiple pulse sequences to dilute spins.

The second dipolar recoupling experiment is a frequency-selective approach to restoring heteronuclear interactions among spin-1/2 nuclei. This technique is complementary to rotational echo double resonance (REDOR) experiments, where all heteronuclear interactions are recoupled into the MAS experiment simultaneously. The development of this sequence is motivated by the goal of examining weak dipolar interactions in a multiple spin environment, where it is desirable to isolate and measure individual couplings. Experimental demonstrations of the frequency-selective recoupling effect are presented in a four spin system, demonstrating the potential for selective measurements of heteronuclear dipole-dipole couplings in MAS experiments. A similar approach to selective dephasing in static polycrystalline solids is also demonstrated. In addition to the basic sequence consisting of two rotor cycles, an alternative approach which is tolerant to pulse imperfections is introduced for application to weak interactions. Lastly, the role of coherence decay during heteronuclear dephasing experiments is explored.

A third topic is the problem of pulse imperfections in multiple pulse experiments. Some controversy has surrounded the question of whether π pulse sequences based on *XY*-4 phase cycling are superior to expansions of MLEV-4, but no theoretical comparison has been made in the most general case where long windows are applied between the pulses. Here, a general method of analysis is presented for the single spin case, and it demonstrates that in most cases there is little difference in the degree of tolerance to pulse errors. Experimental data and a simple model of the interference between RF fields applied to ^{13}C and ^{1}H spins demonstrates that the signal losses

from insufficient proton decoupling during spin echo sequences are minimized with a mismatch ratio of approximately three between the RF fields, while at the same time the highest possible decoupling power level is applied. This condition underscores the importance of employing strong decoupling fields in double and triple resonance recoupling experiments, particular with the use of π pulses.

Finally, an improved method of proton decoupling is introduced for application to cross polarization magic angle spinning (CPMAS) experiments. Particularly in the regime of high and low spinning speeds, it is often observed that inefficient proton decoupling makes a significant contribution to the linewidths of protonated ^{13}C spins at typical proton RF fields of approximately 60-100 kHz. This line-broadening results mainly from resonance offset effects in the regime of large decoupling fields (i. e. greater than 40 kHz). In order to compensate for small shifts of the proton transmitter from resonance, while at the same time efficiently decoupling very strong heteronuclear interactions, a phase-switched variation of simple multiple-frequency decoupling is introduced and applied to several organic compounds in spinning experiments. In these examples, the method yields large improvements in the linewidths relative to continuous-wave (CW) decoupling, even in the presence of large homonuclear interactions among the protons. The experimental observations are explained qualitatively with the aid of an analytical approach based on a double-rotating frame transformation and through consideration of numerical simulations. In addition, some basic distinctions between the influence of proton-proton interactions on the performance of CW decoupling in static and spinning solids are explored in order to explain the observed dependence of the ^{13}C linewidths on resonance offsets. Finally, rotational interference effects in

composite pulse decoupling on spinning samples are considered via experimental and simulated lineshapes.

Chapter 1.

Introduction to Magic Angle Spinning NMR Spectroscopy

I. Line-Narrowing Techniques in Solid State NMR

The NMR spectrum of a solid material, as reconstructed from the free induction decay (FID) following a $\pi/2$ pulse or from the response to continuous-wave (CW) excitation [1], is generally broad and largely uninformative because of several influences. First, in the case of spin-1/2 nuclei, when the spins under observation are coupled to each other by strong homonuclear dipole-dipole (DD) interactions, a broad homogeneous lineshape results [2]. Second, in many cases, the spins experience strong heteronuclear couplings to a second nuclear species, which contribute additional line-broadening or splittings into the NMR spectrum. In the case of powdered solids, where all possible molecular orientations with respect to the magnetic field are represented in the sample, another contribution to the lineshape is the inhomogeneous broadening from anisotropic interactions. Examples of orientation-dependent spin interactions in high magnetic field are the chemical shift anisotropy (CSA) of each spin, the dipole-dipole coupling between pairs of spins, and in the more general case of nuclei possessing spin angular momentum greater than I=1/2, the quadrupolar interaction with the electric field gradient tensor at the nucleus [3].

The greatest challenge in solid state NMR spectroscopy has been the effort to reduce or eliminate some of these contributions to the NMR spectrum, so that an informative subset of the spin interactions, which contain useful information about molecular structure and dynamics, can be observed selectively. For example, in the case of ^{1}H spectroscopy, the linewidth arising from homonuclear interactions (typically $\geq$ 30 kHz) is generally much greater than the range of isotropic chemical shifts, and the first interaction therefore dominates the spectrum. In order to recover the

more valuable information contained in the chemical shifts and other weaker spin interactions, the magic angle spinning (MAS) technique was originally introduced in order to attenuate the influence of homonuclear interactions [4, 5]. By time-averaging the homonuclear couplings to zero over a period of rotation, the NMR spectrum is narrowed considerably, provided that the spinning speed is much more rapid than the spectral linewidth [6]. However, fast mechanical rotation at rates exceeding 15 kHz is quite difficult to achieve even today. An alternative approach involves the application of radio-frequency (RF) pulses. Periodic multiple pulse sequences such as WAHUHA were introduced by Waugh and co-workers for the purpose of eliminating the apparent influence of strong homonuclear couplings on the spin evolution at multiples of the period of excitation [7]. At the same time, however, the time-evolution of the magnetization under the Zeeman-like terms in the spin Hamiltonian is permitted to continue in these experiments, allowing for their selective observation.

Average Hamiltonian Theory (AHT) [3, 8] provides a theoretical basis for these multiple pulse line-narrowing experiments and, more generally, a flexible means of understanding the time evolution of spin systems under complicated periodic excitations. Specifically, the AHT approach provides a convenient framework for the design and analysis of pulse sequences which generate a desired "coherent averaging" effect of various spin interactions, which is complementary to the incoherent averaging of spin interactions by molecular motion. The only restrictions are that the time-dependence of the system must be periodic and that, in order to truncate the Magnus expansion after one or two orders, the Hamiltonian in the chosen interaction frame must be a small perturbation over the time-averaging cycle. The AHT approach is therefore useful for the analysis of spin systems experiencing

both RF excitations and sample spinning, as long as the combined time-dependence remains periodic. In fact, AHT plays a key role in understanding the performance of magic angle spinning in various spin systems [6, 9, 10] and is frequently useful in understanding dipolar evolution experiments in rotating samples with rotor-synchronized multiple pulse sequences [11].

In addition to homonuclear decoupling, another important role of RF fields in the line-narrowing and simplification of NMR spectra is the decoupling of one heteronuclear spin from another [12, 13]. The application of a large continuous-wave (CW) RF field to one spin eliminates the apparent coupling of that spin in the NMR spectrum of the other nucleus. Because of the great importance of this technique in both solid and solution state NMR spectroscopy, much effort has been applied to understanding spin decoupling and developing methods which compensate for imperfections in its performance. In most cases, the major practical difficulty is the deterioration of line-narrowing efficiency which results from shifts of the RF transmitter from resonance with the spin being decoupled. Many phase- and even frequency-switched modifications of CW decoupling have been introduced in order compensate for the resonance offset effect [14].

Another challenge of particular significance in solid state experiments is the poor sensitivity of nuclear magnetic resonance techniques. For many rare spins with low gyromagnetic ratios, T_1 relaxation is extremely slow in rigid solids (>> min in many cases). In most organic compounds, longitudinal relaxation is much faster within the proton reservior than among more dilute spins with lower gyromagnetic ratios, and in addition the ^1H system possesses relatively high spin polarization at equilibrium. Therefore, the technique of cross polarization (CP) [15], in which the magnetizations of the protons and the observed rare spins are equilibrated in the rotating frame, is

usually employed in observing dilute spins in organic solids. Under the influence of matching RF fields applied to both nuclear systems, each spin experiences the same effective Larmor frequency in the rotating frame, and the large barrier to polarization transfer which exists between heteronuclei in the laboratory frame is therefore eliminated, allowing polarization exchange to occur.

To summarize, in many compounds, the methods of homonuclear and heteronuclear decoupling, combined with the MAS technique, have made it possible to obtain spectra of resolved isotropic chemical shifts in the solid state [15-17]. Although MAS is not very efficient for the elimination of homonuclear couplings at practical spinning speeds, it has proved extremely valuable for the attenuation of the chemical shift anisotropy (CSA) in orientationally disordered systems, since spectral line-broadening from this interaction breaks up into sharp sidebands in the slow spinning regime [6, 9, 18]. For this reason, the combined use of proton decoupling, cross polarization, and MAS, which is now known as the CPMAS experiment [16], has become the standard method for observing the high resolution spectra of "dilute" spins, such as ^{13}C, ^{15}N, and ^{31}P, in polycrystalline samples. In addition, the use of two dimensional techniques is sometimes helpful in achieving even greater enhancements in spectral resolution [19].

II. Measurements of Dipole-Dipole Couplings

The measurement of homo- and heteronuclear dipolar couplings by nuclear magnetic resonance (NMR) techniques is an important tool for the determination of molecular structure in solids [11, 20]. In a static polycrystalline solid, the dipolar coupling between two magnetically dilute

spins results in the characteristic "Pake pattern" [21], first observed in the ^1H spectrum of gypsum, $CaSO_4 \cdot 2H_2O$, which arises from the interaction between the two protons in the water molecules of hydration. The splitting between the singularities provides a straightforward measurement of the dipolar coupling constant and therefore the internuclear distance between the two spins. Unfortunately, in the more general case, the structural information revealed by internuclear distances cannot be obtained directly from the static ^1H spectrum because of the multiplicity of couplings. In situations involving other nuclei, such ^{13}C, ^{15}N, and ^{31}P, large chemical shift anisotropies, as well as other line-broadening mechanisms, obscure the lineshape perturbations from the through-space dipolar couplings.

As a consequence of these problems, various methods have been developed that separate the dipolar couplings of interest from the other interactions in static samples, most notably the chemical shift terms present in the spin Hamiltonian. These techniques include separated local field (SLF) spectroscopy [22-25], spin echo double resonance (SEDOR) [26-31], nutation NMR [32], and the use of Carr Purcell echo sequences to measure homonuclear dipole-dipole couplings [33, 34]. The two-dimensional SLF experiment, performed on both single crystals [22] and powders [23], correlates the anisotropic chemical shift interactions of dilute spins with their dipolar couplings to neighboring abundant spins. In SEDOR, the intensity of a spin echo is attenuated by heteronuclear dipole-dipole couplings that are prevented from refocusing by the application of suitable π pulse sequences. By comparison with the amplitude of a complete spin echo, these couplings can be measured to determine internuclear distances. In rotating solids, a similar strategy is employed in rotational echo double resonance (REDOR) experiments [35, 36], where the formation of rotational echoes is hindered by

rotor-synchronized π pulse sequences. The remaining two experiments separate dipolar couplings from chemical shifts in static homonuclear spin systems. In nutation NMR, this separation is achieved by the application of continuous RF fields, which eliminate chemical shifts and heteronuclear interactions, but retain scaled homonuclear couplings. Carr Purcell echo sequences, on the other hand, retain the full strength of the homonuclear interaction in the limit of short π pulses.

These approaches are useful for the determination of molecular structure in static solids, including powders. However, in order to obtain high resolution NMR spectra of solids, the application of magic angle spinning is essential [4-6, 16, 17, 37]. MAS efficiently attenuates weak heteronuclear and homonuclear dipole-dipole couplings, as well as all chemical shift anisotropies, resulting in well-resolved spectra of the isotropic chemical shifts. In order to observe selected dipolar couplings in rotating solids, it is therefore necessary to reintroduce them into the experiment by some method that reverses their elimination by sample spinning. At the same time, as in the case of non-rotating solids, it is frequently desirable to separate recoupled interactions from other contributions to the spin Hamiltonian. Often, this criterion leads to the simultaneous elimination of chemical shifts from the experiment, in the sense of coherent averaging, through the use of spin echo sequences.

Several approaches have now been developed that achieve a suitable recoupling of the dipolar interaction for both heteronuclear and homonuclear spins in rotating solids. In the absence of RF pulses, the heteronuclear spin system is completely refocused after each rotor cycle and is therefore "inhomogeneous" in the sense introduced by Maricq and Waugh (MW) [6]. The fact that all terms in the heteronuclear MAS spin Hamiltonian commute

with one another at different times, a property that also holds under π pulse sequences, has led to several elegant spin echo techniques designed to measure internuclear distances [35, 38-41]. In contrast, under most circumstances, the flip-flop term of the homonuclear dipolar coupling results in the non-commutation of the spin Hamiltonian with itself at different times, rendering it an "homogeneous" interaction in the MW terminology. In the special case of a homonuclear spin pair, the chemical shift terms and the flip-flop part of the dipole-dipole interaction are non-commuting and lead to homogeneous behavior [6]. More generally, in the case of several spins, there are many dipolar couplings, and in most cases these interactions fail to commute because of the flip-flop terms. Accordingly, the rotational refocusing of observed signals is spoiled to varying degrees, and it is often necessary to spin much faster than the magnitude of the interactions in order to suppress them efficiently. In the case of homonuclear spins, the development of dipolar recoupling experiments requires consideration of the additional complexity introduced by the homogeneous nature of the spin Hamiltonian.

Recoupling methods that are applicable to homonuclear spin systems include experiments in which recoupling is driven solely by the mechanical rotation, as in longitudinal exchange at rotational resonance (R2) [42-45], and methods where multiple pulse sequences are applied in order to reintroduce the dipolar coupling. These approaches can be further divided into "direct" recoupling sequences [46-49], in which a pulse sequence similar to a solid echo [30] or magic echo [50] scheme is used to interfere with dipolar cancellation by MAS, and spin echo sequences employing π pulses [51-53], where the recoupling effect depends on the modulation of the dipolar coupling by chemical shift differences between the spins in the toggling frame.

Recoupling by rotational resonance also relies on the influence of the chemical shift difference. In a suitable interaction frame [54, 55], the destructive interference between MAS and the evolution of the dipolar flip-flop term between the spins leads to a non-vanishing dipole-dipole interaction.

In addition to REDOR experiments, other techniques which have been introduced for heteronuclear spins include rotary resonance recoupling (R3) [56-58] and dipolar chemical shift correlation spectroscopy (DIPSHIFT) [38, 40, 59]. In the first method, a single-phase RF field is applied to one of the two heteronuclear spin systems. With a sufficiently strong RF field, the irradiation causes decoupling [60, 61], but for weak fields recoupling occurs in MAS experiments when the amplitude of the RF field is matched to a multiple of the spinning speed, i. e. $\nu_{RF} = m\nu_R$. At rotary resonance, the RF field spoils the inhomogeneous character of the spin system, the property that its NMR spectrum is comprised of sharp sideband intensities [6], and powder patterns reflecting the interaction strength are regenerated [56]. This approach is significant for the case of weak coupling because the interaction is not reflected clearly in the sideband intensities when the spinning rate exceeds the heteronuclear coupling strength. In DIPSHIFT experiments, on the other hand, large heteronuclear interactions are examined, usually between protons and dilute spins. In these experiments, the first dimension of a two-dimensional (2D) experiment reveals the heteronuclear coupling via the removal of the proton decoupling field, which is instead replaced by a sequence which attenuates the homonuclear ^{1}H-^{1}H interactions [62-64]. In the absence of the homonuclear couplings, the NMR spectrum is again inhomogeneous, and the dipolar coupling strength between directly bonded

^{1}H nuclei and dilute spin-1/2 nuclei is observed in the large sideband intensities which remain in the slow spinning regime.

Figure (1-1) illustrates the powder lineshape, or "Pake pattern," which results from the heteronuclear coupling of an isolated spin pair. In the absence of large chemical shifts and couplings to more distant nuclei, the analogous homonuclear spectrum has an identical shape, except that it is broader by $\times 3/2$ because of the additional flip-flop term in the homonuclear dipole-dipole coupling. Under magic angle spinning, the heteronuclear lineshape breaks up into sharp sidebands. In the slow spinning speed regime, their envelope of intensities reflects the shape of the static spectrum. However, in the fast spinning limit, only the centerband remains. The direct measurement of weak dipole-dipole couplings (< 2 kHz) from the NMR spectrum therefore requires extremely slow spinning speeds which are often impractical, necessitating the use of recoupling pulse sequences. In addition, the spectra in Figure (1-1) are scaled to similar proportions for convenience, but the actual peak heights are greatly enhanced under MAS, most notably at higher spinning speeds, because the total integrated spectral intensity is conserved as the spinning frequency is increased.

Figure (1-1). Numerical Simulations of heteronuclear dipolar spectra associated with an isolated spin pair at 0 kHz, 2 kHz, and 10 kHz spinning frequencies, respectively, from top to bottom. The coupling constant is 23.3 kHz, corresponding to a typical ^{1}H-^{13}C separation of 1.09 Å. All chemical shift interactions are omitted for simplicity. The static spectrum exhibits the symmetric Pake pattern corresponding to an isotropic distribution of internuclear vector orientations in the magnetic field. Under MAS conditions, the pattern of sideband intensities reflects the static powder pattern at slow spinning speeds. At greater spinning speeds, however, the influence of the interaction is increasingly attenuated, and the centerband predominates.

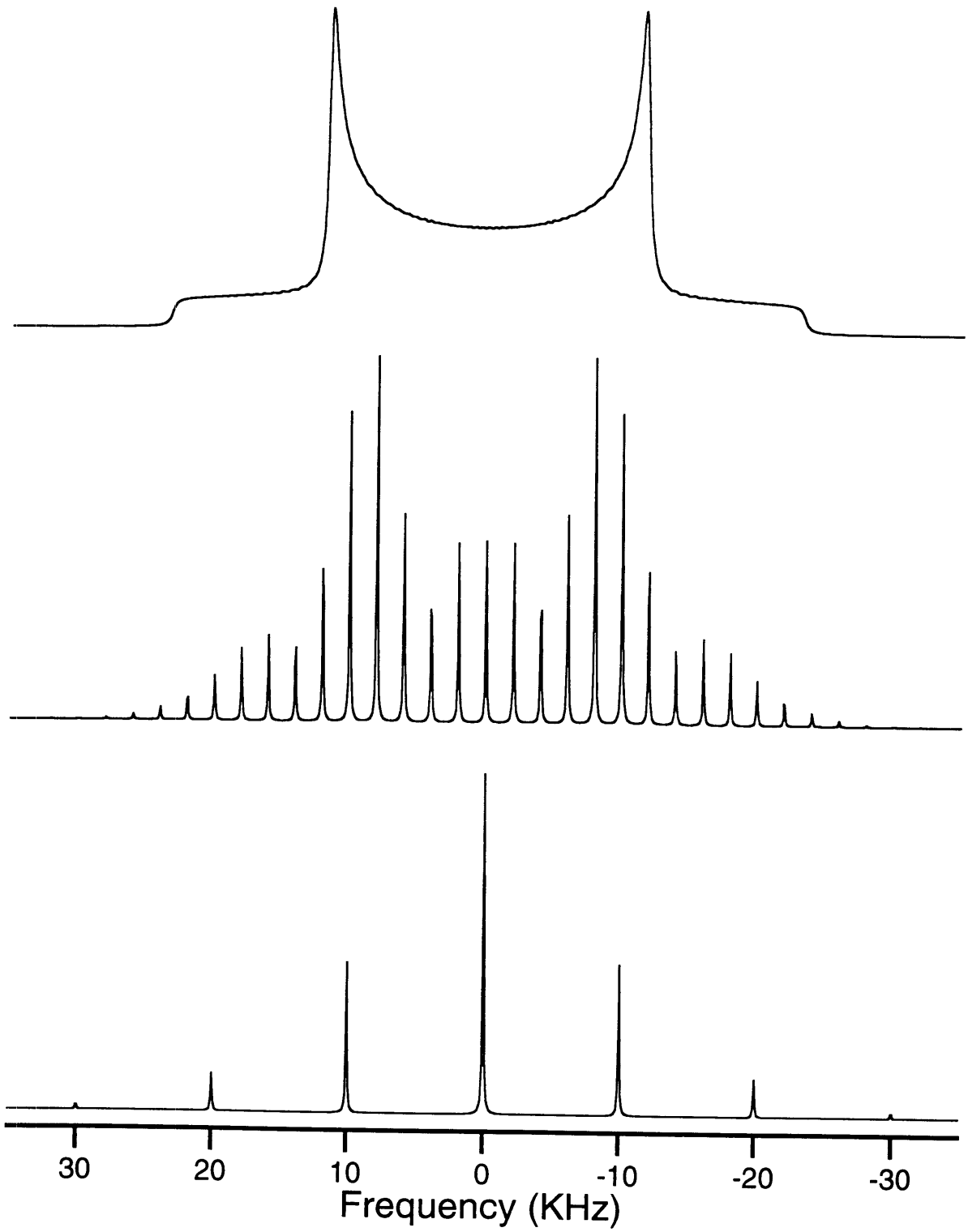
30
20
10
0
-10
-20
-30
Frequency (KHz)

III. Nuclear Spin Interactions

For a system of coupled homonuclear spins with angular momenta I=1/2, which is rotating with respect to the magnetic field, the relevant spin Hamiltonian can be divided as follows [3, 65]:

$$H(t) = H_D(t) + H_{CS}(t) + H_J + H_{RF}(t)\,, \tag{1-1}$$

where $H_D(t)$ represents the dipole-dipole couplings among the spins, $H_{CS}(t)$ the contribution from the chemical shift terms, H_J the indirect spin-spin interactions, or J-couplings, and $H_{RF}(t)$ the RF fields applied to the spin system. Under sample spinning, the geometric factors describing the anisotropic parts of the various spin interactions become time-dependent. Explicit expressions for the terms of the spin Hamiltonian are given by the following equations, which are applicable to a set of spins residing in a large static magnetic field, following the usual rotating frame transformation [30] with respect to all of the spins involved and the neglect of orthogonal time-dependent terms:

$$H_D(t) = \sum_{i<j} d_{ij}(t)\left[3I_{zi}I_{zj} - \vec{I}_i \cdot \vec{I}_j\right]; \tag{1-2a}$$

$$H_{CS}(t) = \sum_i \delta_i(t) I_{zi}\,; \tag{1-2b}$$

$$H_J = \sum_{i<j} J_{ij}\, \vec{I}_i \cdot \vec{I}_j\,; \tag{1-2c}$$

$$H_{RF}(t) = \sum_i \nu_{RF}(t)\left[\cos\chi(t)\, I_{xi} + \sin\chi(t)\, I_{yi}\right]. \tag{1-2d}$$

In the case of the J-coupling, the time-dependent anisotropic terms are assumed to be small and are therefore neglected. The part of the dipolar Hamiltonian in Eq. (1-2a) involving angular momentum operators is $\left[3I_{zi}I_{zj} - \vec{I}_i \cdot \vec{I}_j\right]$ for homonuclear spins, but for two sets of heteronuclear spins $\{i\}$ and $\{j\}$, the expression is further truncated to the form:

$$H_D(t) = \sum_{i<j} d_{ij}(t) \cdot 2I_{zi}I_{zj} \,, \tag{1-3}$$

because of the large difference between the Larmor frequencies of spins with different gyromagnetic ratios γ. The two cases are distinguished by the "flip-flop" operator $-\frac{1}{2}\left[I_{+i}I_{-j} + I_{-i}I_{+j}\right]$, which appears only in the homonuclear case. In this thesis, the expression $2I_{zi}S_{zj}$ is used to refer to the heteronuclear coupling between two nuclei i and j in order to differentiate it from the homonuclear Hamiltonian.

The dipolar coefficients $d_{ij}(t)$ are equal to the nuclear dipole-dipole interaction strength d_{ij} between the nuclei i and j, multiplied by a geometric factor. Planck's constant h is omitted from the definition of the spin Hamiltonian, and in terms of cycles per unit time, the dipolar coupling constant has the form:

$$d_{ij} = \frac{1}{2\pi}\left(\frac{\mu_0}{4\pi}\right)\left\{\frac{\gamma_i\gamma_j\hbar}{r_{ij}^3}\right\}, \tag{1-4}$$

where $\vec{r}_{ij}$ is the vector connecting the two interacting nuclei, and the factors γ_i and γ_j are the gyromagnetic ratios of the spins. The constant μ_0 is the permeability of free space. Knowledge of the coupling constant defined by Eq. (1-4) implies knowledge of the internuclear distance r_{ij}. In a sample rotating

with angular frequency ω_R, the time-dependence of the dipolar interaction coefficient can be expressed as follows [6, 10]:

$$d_{12}(t) = d_{12}\left\{G_0 + G_1\cos(\omega_R t + \phi_{ij}) + G_2\cos(2\omega_R t + 2\phi_{ij})\right\}, \tag{1-5}$$

where:

$$\begin{aligned} G_0 &= -\frac{\left(3\cos^2\theta_m - 1\right)}{2}\frac{\left(3\cos^2\theta_{ij} - 1\right)}{2}; \\ G_1 &= \frac{3}{4}\sin 2\theta_m \sin 2\theta_{ij}\ ; \\ G_2 &= -\frac{3}{4}\sin^2\theta_m \sin^2\theta_{ij}\ . \end{aligned} \tag{1-6}$$

The angle θ_m defines the relationship between the external magnetic field and the rotor axis, while $\left(\theta_{ij}, \phi_{ij}\right)$ are the polar angles of $\vec{r}_{ij}$ in a rotating reference frame defined by the rotor at time $t = 0$. Figure (1-2) provides an illustration of the relationships among the laboratory frame, the rotor frame, and the internuclear vector. At the magic angle, $\theta_m = \arccos\left(1/\sqrt{3}\right) \approx 54.7°$, the contribution G_0 vanishes, and the MAS dipolar Hamiltonian contains no terms which are time-independent. The two remaining components in Eq. (1-5) are oscillatory and average to zero over each rotor period. Often, it is also helpful to define the Fourier series of the geometric prefactor, which contains only ± 1 and ± 2 Fourier components under magic angle spinning:

$$d_{12}(t) = \sum_{n=-2, n\neq 0}^{+2} \hat{d}[n](\theta_{ij})\exp\left\{in(\omega_R t + \phi_{ij})\right\}, \tag{1-7}$$

where the Fourier coefficients $\hat{d}_{ij}[n](\theta_{ij})$ have the form:

$$\hat{d}_{ij}[\pm n](\theta_{ij}) = \frac{1}{2} d_{12} G_{|n|} \,. \tag{1-8}$$

In a similar way, the chemical shift (CS) coefficient $\delta_i(t)$ appearing in Eq. (1-2b) is a function of the three principal values $\left(\sigma_{11}^i, \sigma_{22}^i, \sigma_{33}^i\right)$ of the chemical shift tensor in the principal axis system (PAS) of spin i, including the shift in frequency from resonance. With the RF transmitter frequency defined at zero, the isotropic frequency offset, the chemical shift anisotropy (CSA) factor, and the asymmetry parameter are defined as follows:

$$\begin{aligned}
&\hat{\delta}_i[0] = \frac{\omega_0}{2\pi}\overline{\sigma}^i = \frac{\omega_0}{2\pi}\frac{1}{3}\left(\sigma_{11}^i + \sigma_{22}^i + \sigma_{33}^i\right); \\
&\delta_i^{CSA} = \frac{\omega_0}{2\pi}\left(\sigma_{33}^i - \overline{\sigma}^i\right); \\
&\eta_i = \frac{\left(\sigma_{22}^i - \sigma_{11}^i\right)}{\left(\sigma_{22}^i - \overline{\sigma}^i\right)};
\end{aligned} \tag{1-9}$$

with the convention $\left|\sigma_{33}^i - \overline{\sigma}^i\right| \geq \left|\sigma_{22}^i - \overline{\sigma}^i\right| \geq \left|\sigma_{11}^i - \overline{\sigma}^i\right|$, where $\overline{\sigma}^i$ is the isotropic chemical shift of spin i, which is generally expressed in parts per million (ppm). Here the Larmor frequency has the definition $\omega_0 = \gamma_i \mathrm{H}_0$ in units of radians per unit time, where H_0 is the static magnetic field strength. In close analogy to the dipolar amplitude, the CS coefficient in a spinning solid has the general form [6, 10]:

$$\delta_i(t) = \hat{\delta}_i[0] + \delta_i^{CSA}\left\{g_0 + g_1\cos\left(\omega_R t + \gamma_i + \psi_1\right) + g_2\cos\left(2\omega_R t + 2\gamma_i + \psi_2\right)\right\}, \tag{1-10}$$

where $(\alpha_i, \beta_i, \gamma_i)$ are the Euler angles of the CSA tensor of spin i in the reference frame defined by the rotor. The geometric factors are defined by the expressions:

$$g_0 = \frac{(3\cos^2\theta_m - 1)}{2}\left\{\frac{(3\cos^2\beta_i - 1)}{2} - \frac{\eta_i}{2}\sin^2\beta_i\cos 2\alpha_i\right\};$$

$$g_1 = -\frac{1}{2}\sin 2\theta_m \sin\beta_i\left\{(\eta_i\cos 2\alpha_i + 3)^2\cos^2\beta_i + \eta_i^2\sin^2 2\alpha_i\right\}^{1/2}; \qquad (1\text{-}11)$$

$$g_2 = \frac{1}{2}\sin^2\theta_m\left\{\left[\frac{3}{2}\sin^2\beta_i - \frac{\eta_i}{2}\cos 2\alpha_i(1+\cos^2\beta_i)\right]^2 + \eta_i^2\cos^2\beta_i\sin^2 2\alpha_i\right\}^{1/2};$$

and:

$$\psi_1 = \arctan\left\{\frac{\eta_i\sin 2\alpha_i}{(\eta_i\cos 2\alpha_i + 3)\cos\beta_i}\right\};$$

$$\psi_2 = \arctan\left\{\frac{-\eta_i\cos\beta_i\sin 2\alpha_i}{(3/2)\sin^2\beta_i - (\eta_i/2)\cos 2\alpha_i(1+\cos^2\beta_i)}\right\}. \qquad (1\text{-}12)$$

The time-independent contribution g_0 again vanishes at the magic angle. The Euler angle α_i appears only the phase angles ψ_1 and ψ_2. Under MAS, the Fourier expansion of the chemical shift coefficient is likewise expanded as follows:

$$\delta_i(t) = \sum_{n=-2}^{+2}\hat{\delta}_i[n](\alpha_i,\beta_i)\exp\{in(\omega_R t + \gamma_i)\}, \qquad (1\text{-}13)$$

with the definitions of the isotropic shift from resonance $\hat{\delta}_i[0]$ – which does not depend on the orientational Euler angles – and the relation:

$$\hat{\delta}_i[\pm n] = \frac{1}{2}\delta_i^{CSA} g_{|n|} \exp\left\{\pm in\psi_{|n|}\right\}. \tag{1-14}$$

In contrast to the dipolar coupling, all of whose components are oscillatory at the magic angle, the CS interaction tensor has, in general, a non-zero Fourier component at $n = 0$, namely, the shift from resonance, in addition to the elements $n = \pm 1, \pm 2$. From the perspective that the interactions are second-rank tensors acting on the spin operators, this distinction arises from the fact that the trace of the matrix which characterizes the dipolar coupling is zero, whereas the trace of the CS interaction is, in general, non-vanishing [3, 65].

With the neglect of the anisotropic part of the J-coupling Hamiltonian, its coefficients are independent of orientation, and H_J remains time-independent during MAS experiments. In addition, the J-coupling of Eq. (1-2c) is further truncated to the expression:

$$H_J = J_{ij} I_{zi} I_{zj}\ , \tag{1-15}$$

for heteronuclear spins, and also for homonuclear spins when the condition $\left|\delta_i(t) - \delta_j(t)\right| >> \left|J_{ij}\right|$ holds at all times. In most cases, the J-coupling is neglected in the analysis of the experiments discussed here because in solids it is dominated by the much larger dipole-dipole interaction, and it consequently plays a subordinate role in the nuclear spin dynamics.

The RF irradiation term $H_{RF}(t)$ of the Hamiltonian is in most cases a strong function of time. Together, the amplitude $\nu_{RF}(t)$ and the phase $\chi(t)$ in Eq. (1-2d) characterize an arbitrary RF excitation applied to the set of I spins after the rotating frame transformation. If there is a second set of spins

S possessing a different Larmor frequency, then a second RF field is also included within the framework of its own rotating frame transformation.

Figure (1-2). Relationship of the rotor principal axis system (PAS) to the laboratory reference frame. The axis of rotation Z_R is oriented at the magic angle θ_m with respect to the direction of the static magnetic field. The internuclear vector $\vec{r}_{ij}$ rotates about the longitudinal axis of the rotor, and its time average therefore lies along the magic angle where the dipolar coupling is zero. The X axes of the reference systems are parallel and point outward. While only two angles $\left(\theta_{ij}, \phi_{ij}\right)$ are needed to express the orientation between the rotor and dipolar principal axis systems, three Euler angles $\left(\alpha_i, \beta_i, \gamma_i\right)$ must be specified for the CSA interaction.

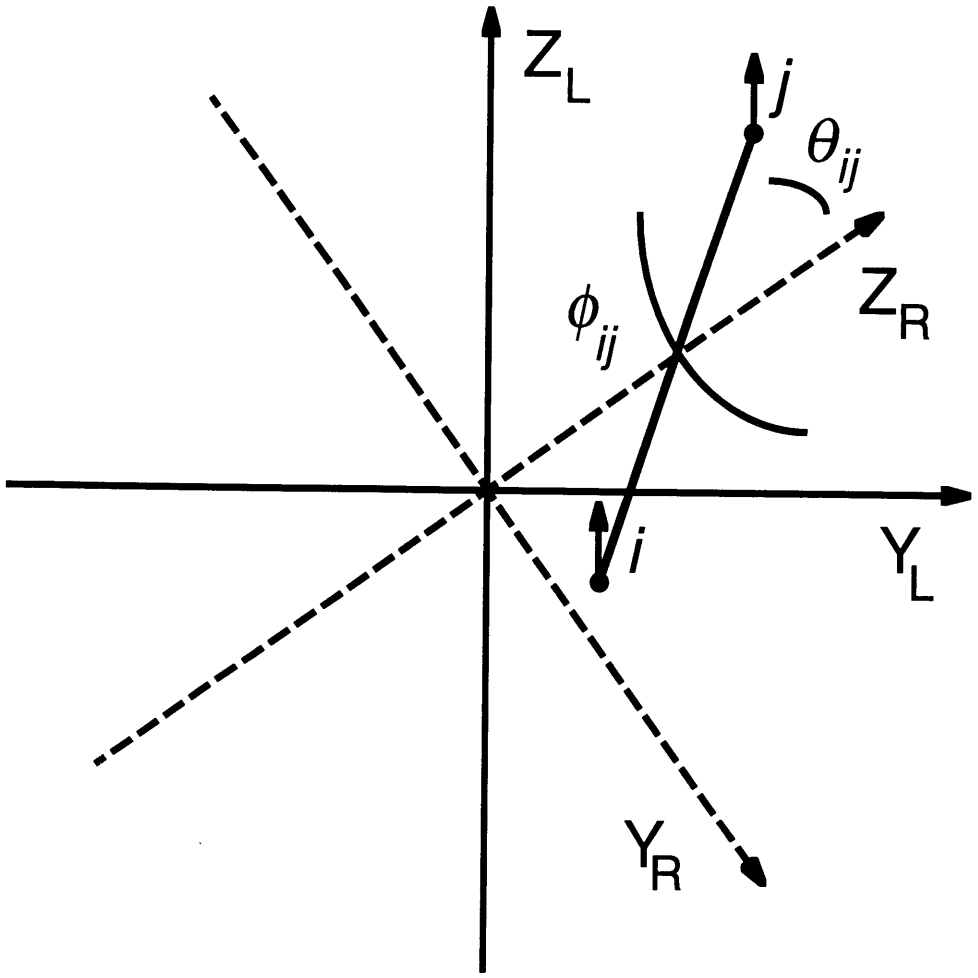
Z_L
j
θ_{ij}
Z_R
ϕ_{ij}
i
Y_L
Y_R

IV. Average Hamiltonian Theory

In many experiments combining MAS and RF excitations, the time-dependence of the RF field is periodic and synchronous with the rotation of the sample [10]. Two theoretical approaches which are applicable to a spin Hamiltonian whose overall time-dependence is periodic are Average Hamiltonian Theory and Floquet Theory [66-69]. Although Floquet Theory has recently become an effective tool for understanding MAS recoupling experiments [11], the AHT approach is adequate for describing most of the experiments presented in subsequent chapters, where weak interactions are subjected to periodic excitation and observation. An exception is the case of heteronuclear decoupling, where the pulse sequence is generally applied asynchronously with MAS, and the relevant dipole-dipole couplings are mostly large relative to the spinning frequency.

The spin density matrix $\rho(t)$ enables the description of nuclear spin evolution during NMR experiments. The operator representing the statistical state of the spin system satisfies the Liouville equation [70]:

$$\frac{d}{dt}\rho(t) = -i\left[H(t),\rho(t)\right], \tag{1-16}$$

which has the formal solution:

$$\rho(t) = U(t,0)\rho(0)U^{-1}(t,0), \tag{1-17}$$

where the time evolution operator is given by:

$$U(t,0) = T\exp\left\{-i\int_0^t dt'\,H(t')\right\}. \tag{1-18}$$

The Dyson time ordering operator T necessitates a stepwise propagation to evaluate the time evolution operator, which makes both approximate and numerical calculations difficult to perform.

For the case of synchronous sampling, an exact time-independent effective Hamiltonian can be defined which provides a complete description of the stroboscopic behavior of $\rho(t)$. With a periodic time-dependence modulo τ_C, the time evolution operator satisfies the condition:

$$\begin{aligned} U(n\tau_C,0) &= T\exp\left\{-i\int_0^{n\tau_C} dt\, H(t)\right\} \\ &= \left[T\exp\left\{-i\int_0^{\tau_C} dt\, H(t)\right\}\right]^n \\ &= \left[U(\tau_C,0)\right]^n . \end{aligned} \tag{1-19}$$

If the spin system is monitored only at times $t = n\tau_C$, then the evolution operator $U(\tau_C,0)$ suffices to determine the evolution of the density operator $\rho(t)$. The exact effective Hamiltonian $\overline{H}_{eff}$ can then be defined as the time-independent Hermitian operator satisfying the relationship [71-73]:

$$U(\tau_C,0) = \exp\left\{-i\overline{H}_{eff}\tau_C\right\}. \tag{1-20}$$

If the net evolution of $\overline{H}_{eff}$ over τ_C yields a small rotation angle in the multi-dimensional space of spin states, then it is valid to apply a perturbation approach in terms of powers of the Hamiltonian, and the effective Hamiltonian can be approximated via the Magnus expansion [8, 74-76]:

$$\overline{H}_{eff} = \overline{H}_{eff}^{(0)} + \overline{H}_{eff}^{(1)} + \overline{H}_{eff}^{(2)} + \ldots , \tag{1-21}$$

where:

$$\overline{H}_{eff}^{(0)} = \frac{1}{\tau_C}\int_0^{\tau_C} dt\, H(t);$$

$$\overline{H}_{eff}^{(1)} = \frac{-i}{2\tau_C}\int_0^{\tau_C} dt \int_0^t dt' \left[H(t), H(t')\right]; \tag{1-22}$$

$$\overline{H}_{eff}^{(2)} = \frac{1}{6\tau_C}\int_0^{\tau_C} dt \int_0^t dt' \int_0^{t'} dt'' \left[H(t''),\left[H(t'), H(t)\right]\right]$$

$$+\left[H(t),\left[H(t'), H(t'')\right]\right].$$

Because the effective Hamiltonian is Hermitian through any order, the corresponding time evolution operator is always unitary. Therefore, this approach is preferable to ordinary time-dependent perturation theory [70] in describing the evolution of the coherent spin system. The zeroth order term $\overline{H}_{eff}^{(0)}$ is simply the average over the time period τ_C, and it constitutes the basic AHT approximation. If the influence of the Hamiltonian is a small perturbation when integrated over the cycle time, then this average provides a reasonable estimate of the effective Hamiltonian. Furthermore, in the special case where the full Hamiltonian $H(t)$ commutes with itself at different times, the first term $\overline{H}_{eff}^{(0)}$ provides the exact result, since all terms of higher order involve commutators which vanish. Sometimes, symmetry considerations simplify the evaluation of higher order terms. For example, the odd order terms of the Magnus expansion vanish for Hamiltonians that are symmetry in time [3].

The analysis of spin dynamics by AHT leads to a better understanding of the time evolution of nuclear spins primarily by providing approximate effective Hamiltonians that are straightforward to calculate analytically.

When RF excitation is applied, the system is usually transformed into the "toggling frame," where the operators of the internal spin Hamiltonian experience time-dependent modulations under the influence of the RF fields [3]. The motion of angular momentum operators in this interaction frame closely resembles the action of RF fields on the spin operators in the density matrix itself, but should be carefully distinguished from the true physical motion of spin coherences. The transformation into the toggling frame is defined by the time evolution operator for the RF fields:

$$U_{RF}(t,0) = T\exp\left\{-i\int_0^t dt' H_{RF}(t')\right\}, \tag{1-23}$$

and the internal spin Hamiltonian, $H_{int}(t) = H(t) - H_{RF}(t)$, in the toggling frame is defined by the expression:

$$\tilde{H}_{int}(t) = U_{RF}^{-1}(t,0)H_{int}(t)U_{RF}(t,0)\,. \tag{1-24}$$

In terms of the toggling frame Hamiltonian, the overall time evolution operator can be expressed in the form [8, 61]:

$$U(t,0) = U_{RF}(t,0)\left[T\exp\left\{-i\int_0^t dt' \tilde{H}_{int}(t')\right\}\right]. \tag{1-25}$$

The toggling frame transformation is most useful when the sequence of RF excitations is cyclic as well as periodic over a period τ_C. When the cyclic condition $U_{RF}(\tau_C,0) = \pm 1$ is fulfilled, the evolution of the spins over the cycle is completely determined by the portion of the time evolution operator involving $\tilde{H}_{int}(t)$:

$$\exp\left\{-i\overline{H}_{eff}\tau_C\right\} = \exp\left\{-i\int_0^{\tau_C} dt\,\tilde{H}_{int}(t)\right\}. \qquad (1\text{-}26)$$

In MAS experiments, if the RF pulse sequence is synchronous with the time-dependence of the sample rotation, then $\tau_C = N\tau_R$ for some integer N, where τ_R is the rotor period, and the MAS Hamiltonian remains periodic after transformation into the toggling frame. Accordingly, the toggling frame Hamiltonian $\tilde{H}_{int}(t)$ summarizes the combined modulations of the sample rotation and RF pulses on the internal spin operators.

With the application of the AHT approximation to a spin system which is sampled stroboscopically, the complicated spin dynamics determined by $H(t)$ are simplified to understanding the behavior of the system under the influence of $\overline{H}_{eff}^{(0)}$. Since the spinning frequency and the waveform of the RF excitation are under experimental control, the form of $\overline{H}_{eff}^{(0)}$ can in many instances be tailored to a desired form.

V. Spin Dynamics Simulations

When applicable, the AHT approach provides a basic understanding of the outcome of applying a pulse sequence, but for more thorough investigations it is often valuable to perform exact calculations. In some cases, there is no portion of the Hamiltonian which satisfies the condition that it is a small perturbation over the relevant cycle time. In others, the time-dependence is not periodic. Furthermore, even when the AHT is essentially correct, a thorough understanding of more subtle features of the spin dynamics, such as the effects of finite pulses, benefits from performing numerical simulations.

The essential features of a spin dynamics calculation are the construction of the Hamiltonian, the exponentiation of the Hamiltonian to obtain the time evolution operator, and finally the propagation of the density matrix from a given initial condition $\rho(0)$ [55, 61]. Projections of the operator corresponding to the variable of interest onto the density matrix are then taken as a function of time to obtain the trajectory of the observable. Recently, several spin dynamics simulation programs based on this approach have become available, including packages for both IBM-compatible computers [77] and C++ programming environments [78]. However, all of the calculations presented here were carried out with programs written by the author and optimized for MAS applications using the general approach outlined below.

The time evolution operator is divided into short time steps $\Delta\tau$ during which it is a reasonable approximation to regard the Hamiltonian as time-independent:

$$\begin{aligned} U(\tau,0) &= T\exp\left\{-i\int_0^{\tau} dt\, H(t)\right\} \\ &= T\exp\left\{-i\int_{\tau_{n-1}}^{\tau_n} dt\, H(t)\right\}\times T\exp\left\{-i\int_{\tau_{n-2}}^{\tau_{n-1}} dt\, H(t)\right\}\times\ldots\times T\exp\left\{-i\int_{\tau_0}^{\tau_1} dt\, H(t)\right\} \quad (1\text{-}27) \\ &= \exp\{-iH(\tau_{n-1})\Delta\tau\}\times\exp\{-iH(\tau_{n-2})\Delta\tau\}\times\ldots\times\exp\{-iH(\tau_0)\Delta\tau\}\,. \end{aligned}$$

With the definitions $\tau_k = k\Delta\tau$ and $\tau_n = \tau$, the period $(0,\tau)$ is broken up into n intervals, where n is sufficiently large to obtain convergence of the results with respect to the time step $\Delta\tau$.

There are $2N$ quantum states in the Hamiltonian matrix of a system consisting of N spin-1/2 nuclei. During the short time intervals $\Delta\tau$, each time-independent $2N$ by $2N$ Hamiltonian matrix $\boldsymbol{H}$ must be exponentiated.

A straightforward and robust approach to the exponentiation of a matrix employs its eigenvalues and eigenvectors. For a Hermitian matrix $\boldsymbol{H}$, the eigenvalues λ_j are always real, and the matrix of eigenvectors $\boldsymbol{V}$ is unitary. With the definition $\{\boldsymbol{D}\}_{ij} = \delta_{ij}\lambda_j$ of the diagonal matrix of eigenvalues $\boldsymbol{D}$, the Hamiltonian can be expressed in the form $\boldsymbol{H} = \boldsymbol{V}\boldsymbol{D}\boldsymbol{V}^{-1}$, and the corresponding matrix form of the time evolution operator $\boldsymbol{U}$ is the following:

$$\begin{aligned}\boldsymbol{U} &= \exp\{-i\boldsymbol{H}\Delta\tau\} \\ &= \exp\{-i\boldsymbol{V}\boldsymbol{D}\boldsymbol{V}^{-1}\Delta\tau\} \\ &= \boldsymbol{V}\exp\{-i\boldsymbol{D}\Delta\tau\}\boldsymbol{V}^{-1}\,.\end{aligned} \tag{1-28}$$

Within the diagonal representation the matrix exponentiation is straightforward, since it requires only the exponentiation of each diagonal element. Using the unitarity of the eigenvector matrix, which implies that $V_{ij}^{-1} = V_{ji}^{*}$, the elements of $\boldsymbol{U}$ have the form:

$$\begin{aligned}\{\boldsymbol{U}\}_{ij} &= \left\{\exp\{-i\boldsymbol{H}\Delta\tau\}\right\}_{ij} \\ &= \sum_{k=1}^{2N} V_{ik}\exp\{-i\lambda_k\Delta\tau\}V_{kj}^{-1} \\ &= \sum_{k=1}^{2N} V_{ik}V_{jk}^{*}\exp\{-i\lambda_k\Delta\tau\}\,.\end{aligned} \tag{1-29}$$

After the time evolution operator has been determined numerically as a function of time, the calculation of the expectation value of an observable of interest, corresponding to a Hermitian spin operator A, involves taking its projection – defined in the sense of the trace [65] – onto the density matrix:

$$\langle A(t)\rangle = \mathrm{Tr}\{AU(t,0)\rho(0)U^{-1}(t,0)\}. \qquad (1\text{-}30)$$

In general, the density matrix of the nuclear spin system is taken to be in its high temperature limit at thermal equilibrium [79], and only the portion which contributes to observable signals is retained. Since relative changes in spin coherences are usually the quantities of the greatest interest, constant factors multiplying $\rho(0)$ are generally adjusted such that $\langle A(0)\rangle = 1$. For example, in the acquisition of the free induction decay, the evolution of the transverse magnetization, whose expectation value is proportional to $A = (I_x, I_y)$, is monitored with quadrature detection, and the density matrix of initially prepared magnetization is to taken to be $\rho(0) = 2I_x$, where I_x is the total x angular momentum of the spins under observation.

In practice, there are several means of saving computation time which are frequently applicable. First, when the Hamiltonian is periodic, the time evolution operator is required only over one period, and the corresponding evolution of the density matrix can be calculated by applying the same operator repeatedly. In subsequent chapters, this approach is useful in calculating the evolution of nuclear spins under rotor-synchronized recoupling sequences with stroboscopic sampling. However, in the case of decoupling sequences applied with MAS, where the combined time-dependence of the Hamiltonian is generally not periodic, the operator $U(t,0)$ must be calculated for the entire length of the FID.

A second opportunity to save computer time arises when the spin Hamiltonian is block-diagonal. In many experiments, periods of free evolution occur between the application of RF pulses. In these cases, the diagonalization of the Hamiltonian matrix is simplified during part of the spin trajectory. For the two spin system, the internal spin Hamiltonian

consists of a 4 by 4 matrix with at most a 2 by 2 block in the homonuclear case, where the flip-flop term appears off the diagonal in the Zeeman basis set [55]. In the heteronuclear case, the internal spin Hamiltonian is always self-commuting and completely diagonal. Since a 2 by 2 matrix can be diagonalized analytically using the Cayley-Klein parameters [70], numerical diagonalization is never required for evaluation of the free evolution of a two spin system. The use of ideal δ-function pulses, where the RF excitation is assumed to be infinitely brief and intense, is another simplifying factor in calculations. The evolution under these pulses can be treated as a sudden rotation during which the simultaneous time evolution under the internal spin Hamiltonian is negligible.

Sometimes, it is necessary to include the effects of coherence relaxation in numerical simulations. With an exponential model of the decay rates, these calculations necessitate the construction of a supermatrix acting on the set of spin coherences. This matrix, whose dimensionality spans the square of the number of coherences participating in the trajectory, includes the simultaneous evolution under both the spin Hamiltonian and the relaxation effects. The time-dependent density matrix can be expanded in a convenient orthonormal basis set as follows:

$$\rho(t) = \sum_m a_m(t) A^m \ . \tag{1-31}$$

where orthogonality is defined in the sense: $\mathrm{Tr}\{A^m A^n\} = \delta_{mn}$ [65]. The generalizated Liouville equation including exponential relaxation toward equilibrium has the form:

$$\frac{d}{dt}\rho(t) = -i[H(t),\rho(t)] - \Gamma\{\rho(t) - \rho_{eq}\}. \tag{1-32}$$

With suitable phase cycling, however, it is usually unnecessary to include ρ_{eq} in the analysis of recoupling experiments. Under these conditions, Eq. (1-32) can be written more conveniently in terms of the operator expansion:

$$\dot{a}_m(t) = \sum_n \{-i\,\mathrm{Tr}\{A^m[H(t),A^n]\} - \Gamma_{mn}\} a_n(t). \tag{1-33}$$

With the definition of the matrix elements $L_{mn}(t) = \mathrm{Tr}\{A^m[H(t),A^n]\}$, the Liouville equation can be formally integrated:

$$a_m(\tau) = \sum_n \left[T\exp\left\{\int_0^\tau dt(-i\,L(t) - \Gamma)\right\}\right]_{mn} a_n(0). \tag{1-34}$$

With a similar division of the interval $(0,\tau)$ into short times steps $\Delta\tau$, the integration of the Liouville operator requires the exponentiations of M by M matrices, where M is the number of coherences participating in the trajectory. For instance, in the most general case, a total of 15 coherences are necessary to span the density matrix for two spins.

However, the coherent part of the problem, namely, the exponentiation of the series of matrices $\{-iL(\tau_k)\Delta\tau\}$, requires only the construction of $U(\tau_k,\tau_{k-1})$, which is of much lower dimensionality, e. g. 4 by 4 complex for two spins. In addition, the relaxation process is time-independent and often diagonal in a particular basis set of spin coherences [30]. Consequently, in numerical evaluations, it is useful to divide the evolution operator into its coherent and incoherent components as follows:

$$T\exp\left\{\int_0^\tau dt(-iL(t)-\Gamma)\right\} = \exp\{-iL(\tau_{n-1})\Delta\tau\}\times\exp\{-\Gamma\Delta\tau\}\times$$
$$\exp\{-iL(\tau_{n-2})\Delta\tau\}\times\exp\{-\Gamma\Delta\tau\}\times\ldots\times\exp\{-iL(\tau_0)\Delta\tau\}\times\exp\{-\Gamma\Delta\tau\}, \quad (1\text{-}35)$$

which converges in the limit $\Delta\tau \to 0$. Because the Hamiltonian is time-dependent, it is already necessary to concatenate the operators obtained with short time steps $\Delta\tau$, and consequently no further computational sacrifice is introduced by applying this approach to relaxation. In fact, the time step required for convergence is generally unchanged with the addition of relaxation effects in practical MAS applications. On the other hand, if the internal Hamiltonian were time-independent as in solution experiments, it would be more computationally efficient to diagonalize the entire M by M matrix just once in order to describe the spin trajectory.

The choice of basis operators $\{A^m\}$ can be adjusted to obtain maximum computational efficiency for a given problem. It is generally most natural and convenient to calculate $\exp\{-iL(\tau_k)\Delta\tau\}$ and $\exp\{-\Gamma\Delta\tau\}$ in different basis sets: the former in the spin eigenstates of z angular momentum and the latter in terms of product operators [80]. Following the construction of the evolution operators for each time step, they must be transformed into the same basis set. For a time-independent relaxation operator, this operation can be performed once for the relaxation process.

To calculate the macroscopic signal from a polycrystalline solid, the spin trajectories of an isotropic ensemble of crystallite orientations must be calculated in order to compute the integral:

$$\langle\langle A(t)\rangle\rangle_{powder} = \frac{1}{8\pi^2}\int_0^{2\pi}\int_0^{\pi}\int_0^{2\pi} d\alpha\, d\beta \sin\beta\, d\gamma \langle A(t;\alpha,\beta,\gamma)\rangle, \quad (1\text{-}36)$$

where $\langle A(t;\alpha,\beta,\gamma)\rangle$ is the signal obtained from a crystallite with Euler angles (α,β,γ) relating the orientation of its molecular axis system to the rotor reference frame. The necessity of calculating the spin trajectory for a large number of crystallite orientations (≥ 1000 or much greater) is the greatest motivation for optimizing computational efficiency in MAS applications.

References for Chapter 1.

[1] R. R. Ernst, G. Bodenhausen, and A. Wokaun, *Principles of Nuclear Magnetic Resonance in One and Two Dimensions* (Clarendon Press, Oxford, 1987).

[2] A. Abragam, *The Principles of Nuclear Magnetism* (Oxford University Press, London, 1961).

[3] U. Haeberlen, *High Resolution NMR in Solids: Selective Averaging* (Academic Press, New York, 1976).

[4] E. R. Andrew, A. Bradbury, and R. G. Eades, Nature (London) **182**, 1659 (1958).

[5] I. J. Lowe, Phys. Rev. Lett. **2**, 285 (1959).

[6] M. Maricq and J. S. Waugh, J. Chem. Phys. **70**, 3300 (1979).

[7] J. S. Waugh, L. M. Huber, and U. Haeberlen, Phys. Rev. Lett. **20**, 180 (1968).

[8] U. Haeberlen and J. S. Waugh, Phys. Rev. **175**, 453 (1968).

[9] M. Maricq and J. S. Waugh, Chem. Phys. Lett. **47**, 327 (1977).

[10] E. T. Olejniczak, S. Vega, and R. G. Griffin, J. Chem. Phys. **81**, 4804 (1984).

[11] A. E. Bennett, R. G. Griffin, and S. Vega, NMR Basic Principles and Progress **33**, 1 (1994).

[12] V. Royden, Phys. Rev. **96**, 543 (1954).

[13] A. L. Bloom and J. N. Shoolery, Phys. Rev. **97**, 1261 (1955).

[14] A. J. Shaka and J. Keeler, Prog. in NMR Spectroscopy **19**, 47 (1987).

[15] A. Pines, M. G. Gibby, and J. S. Waugh, J. Chem. Phys. **59**, 569 (1973).

[16] J. Schaefer and E. O. Stejskal, J. Am. Chem. Soc. **98**, 1030 (1976).

[17] E. Lippmaa, M. Alla, and T. Tuherm, in *Proc. XIX Congress Ampère*,

H. Brunner, ed. (Group Ampère, Heidelberg, 1976).

[18] J. Herzfeld and A. E. Berger, J. Chem. Phys. **73**, 6021 (1980).

[19] P. Caravatti, L. Braunschweiler, and R. R. Ernst, Chem. Phys. Lett. **100**, 305 (1983).

[20] J. M. Griffiths and R. G. Griffin, Anal. Chim. Acta **283**, 1081 (1993).

[21] G. E. Pake, J. Chem. Phys. **16**, 327 (1948).

[22] R. K. Hester, J. L. Ackerman, B. L. Neff, and J. S. Waugh, Phys. Rev. Lett. **36**, 1081 (1976).

[23] M. E. Stoll, A. J. Vega, and R. W. Vaughan, J. Chem. Phys. **65**, 4093 (1976).

[24] M. Linder, A. Höhener, and R. R. Ernst, J. Chem. Phys. **73**, 4959 (1980).

[25] M. G. Munowitz, T. H. Huang, C. M. Dobson, and R. G. Griffin, J. Mag. Res. **57**, 56 (1984).

[26] B. Herzog and E. L. Hahn, Phys. Rev. **103**, 148 (1956).

[27] D. E. Kaplan and E. L. Hahn, Bull. Am. Phys. Soc. **2**, 384 (1957).

[28] D. E. Kaplan and E. L. Hahn, J. Phys. Radium **19**, 821 (1958).

[29] M. Emshwiller, E. L. Hahn, and D. E. Kaplan, Phys. Rev. **118**, 414 (1960).

[30] C. P. Slichter, *Principles of Magnetic Resonance* (Springer-Verlag, Berlin, 1990).

[31] S. E. Shore, J.-P. Amsermet, C. P. Slichter, and J. H. Sinfelt, Phys. Rev. Lett. **58**, 953 (1987).

[32] C. S. Yannoni and R. D. Kendrick, J. Chem. Phys. **74**, 747 (1981).

[33] M. Engelsberg and C. S. Yannoni, J. Mag. Res. **88**, 393 (1990).

[34] M. J. Lizak, T. Gullion, and M. S. Conradi, J. Mag. Res. **91**, 254 (1991).

[35] T. Gullion and J. Schaefer, J. Mag. Res. **81**, 196 (1989).

[36] T. Gullion and J. Schaefer, Adv. Mag. Res. **13**, 58 (1989).

[37] E. R. Andrew, W. S. Hinshaw, and R. S. Tiffen, J. Mag. Res. **15**, 191 (1974).

[38] M. G. Munowitz and R. G. Griffin, J. Chem. Phys. **76**, 2848 (1982).

[39] M. G. Munowitz and R. G. Griffin, J. Chem. Phys. **78**, 613 (1983).

[40] J. Schaefer, R. A. McKay, E. O. Stejskal, and W. T. Dixon, J. Mag. Res. **52**, 123 (1983).

[41] A. C. Kolbert, D. P. Raleigh, M. H. Levitt, and R. G. Griffin, J. Chem. Phys. **90**, 679 (1989).

[42] D. P. Raleigh, M. H. Levitt, and R. G. Griffin, Chem. Phys. Lett. **146**, 71 (1988).

[43] M. G. Columbo, B. H. Meier, and R. R. Ernst, Chem. Phys. Lett. **146**, 189 (1988).

[44] W. E. J. R. Maas and W. S. Veeman, Chem. Phys. Lett. **149**, 170 (1988).

[45] A. Kubo and C. A. McDowell, J. Chem. Soc. Faraday Trans. **84**, 3713 (1988).

[46] R. Tycko and G. Dabbagh, Chem. Phys. Lett. **173**, 461 (1990).

[47] R. Tycko and S. O. Smith, J. Chem. Phys. **98**, 932 (1992).

[48] T. Fujiwara, A. Ramamoorthy, K. Nagayama, K. Hoika, and T. Fujito, Chem. Phys. Lett. **212**, 81 (1993).

[49] A. Ramamoorthy, T. Fujiwara, and K. Nagayama, J. Mag. Res. A **104**, 366 (1993).

[50] W.-K. Rhim, A. Pines, and J. S. Waugh, Phys. Rev. B **3**, 684 (1971).

[51] A. E. Bennett, J. H. Ok, R. G. Griffin, and S. Vega, J. Chem. Phys. **96**, 8624 (1992).

[52] T. Gullion and S. Vega, Chem. Phys. Lett. **194**, 423 (1992).

[53] D. K. Sodickson, M. H. Levitt, S. Vega, and R. G. Griffin, J. Chem. Phys. **98**, 6742 (1993).

[54] Z. H. Gan and D. M. Grant, Mol. Phys. **67**, 1419 (1989).

[55] M. H. Levitt, D. P. Raleigh, F. Creuzet, and R. G. Griffin, J. Chem. Phys. **92**, 6347 (1990).

[56] T. G. Oas, R. G. Griffin, and M. H. Levitt, J. Chem. Phys. **89**, 692 (1988).

[57] M. H. Levitt, T. G. Oas, and R. G. Griffin, Isr. J. Chem. **28**, 271 (1988).

[58] A. Schmidt and S. Vega, Isr. J. Chem. **32**, 215 (1992).

[59] J. A. Diverdi and S. J. Opella, J. Am. Chem. Soc. **104**, 1761 (1982).

[60] P. W. Anderson and R. Freeman, J. Chem. Phys. **37**, 85 (1962).

[61] J. S. Waugh, J. Mag. Res. **50**, 30 (1982).

[62] W. K. Rhim, D. D. Elleman, and R. W. Vaughan, J. Chem. Phys. **59**, 3740 (1973).

[63] D. P. Burum and W.-K. Rhim, J. Chem. Phys. **71**, 944 (1979).

[64] D. P. Burum, M. Linder, and R. R. Ernst, J. Mag. Res. **44**, 173 (1981).

[65] M. Mehring, *Principles of High Resolution NMR in Solids* (Springer-Verlag, Berlin, 1983).

[66] J. M. Shirley, Phys. Rev. B **138**, 979 (1965).

[67] D. R. Dion and J. O. Hirschfelder, Adv. Chem. Phys. **35**, 265 (1976).

[68] Y. Zur, M. H. Levitt, and S. Vega, J. Chem. Phys. **78**, 5293 (1983).

[69] D. B. Zax, G. Goelman, D. Abramovich, and S. Vega, Adv. Mag. Res. **14**, 219 (1990).

[70] J. J. Sakurai and S. F. Tuan, *Modern Quantum Mechanics* (Benjamin/ Cummings Publishing, Menlo Park, 1985).

[71] M. M. Maricq, Adv. Mag. Res. **14**, 151 (1990).

[72] M. M. Maricq, Phys. Rev. B **25**, 6622 (1982).

[73] A. Llor, Chem. Phys. Lett. **199**, 383 (1992).

[74] W. Magnus, Comm. Pure Math. **7**, 649 (1954).

[75] P. Pechukas and J. C. Light, J. Chem. Phys. **44**, 3897 (1966).

[76] W. A. B. Evans, Ann. Phys. **48**, 72 (1968).

[77] F. S. de Bouregas and J. S. Waugh, J. Mag. Res. **96**, 280 (1992).

[78] S. A. Smith, T. O. Levante, B. H. Meier, and R. R. Ernst, J. Mag. Res. A **106**, 75 (1994).

[79] M. Goldman, *Quantum Description of High-Resolution NMR in Liquids* (Oxford University Press, Oxford, 1988).

[80] O. W. Sørensen, G. W. Eich, M. H. Levitt, G. Bodenhausen, and R. R. Ernst, Prog. NMR Spectroscopy **16**, 163 (1983).

Chapter 2.

Homonuclear Dipolar Recoupling with Spin Echo Sequences

I. Introduction

The homonuclear dipolar interaction provides a direct route to internuclear distances among spins in solids possessing the same gyromagnetic ratio γ. In rotating solids, weak dipole-dipole couplings are greatly attenuated, and so in order to recover valuable information about molecular structure from the dipolar interactions, several "recoupling" techniques have been developed in recent years to restore and measure the couplings selectively in various MAS experiments [1, 2]. In this section, the application of π pulse sequences to recoupling homonuclear interactions [3-5] is explored with an emphasis on longitudinal exchange experiments involving weak interactions.

Since the application of spin echo sequences leads to recoupling over a broad range of chemical shift parameters, in contrast to rotational resonance experiments, where exchange proceeds only at certain resonance conditions [6, 7], this approach is suitable for recoupling several spins simultaneously in two-dimensional (2D) exchange experiments. A suitable pulse sequence is shown in Figure (2-1). With 2D acquisition and longitudinal mixing [8], the polarization transfer is achieved by a train of rotor-synchronized π pulses [4, 9]. Figure (2-2) shows a two-dimensional spectrum of triply-^{13}C-labeled alanine obtained with this radio-frequency driven recoupling (RFDR) method [4], revealing correlations among all three spins in the two-dimensional plane after 8.6 ms. This approach has also been applied to the study of the 26 kD membrane protein bacteriorhodopsin [10]. In simple cases, such as a sample with a pair of ^{13}C-labeled nuclei, a one-dimensional approach to π pulse exchange [5], which is illustrated in Figure (2-3), is often more convenient in practice due to the shorter acquisition time.

Frequently, because of relaxation processes and signal losses from insufficient proton decoupling, decay parameters for the spin coherences must be included in the analysis of exchange with weak dipole-dipole couplings. Simulated trajectories based on a simple model for the observed signal losses are in good agreement with experimental results for homonuclear couplings as weak as 80 Hz, which corresponds to a 4.56 Å internuclear distance.

Figure (2-1). Two-dimensional RFDR pulse sequence. Frequency-labeling in the two dimensions is obtained during the time intervals t_1 and t_2. During the mixing period, the polarization is stored along the static magnetic field direction z, and exchange among resonances is obtained with the rotor-synchronized echo sequence of one π pulse per rotor period.

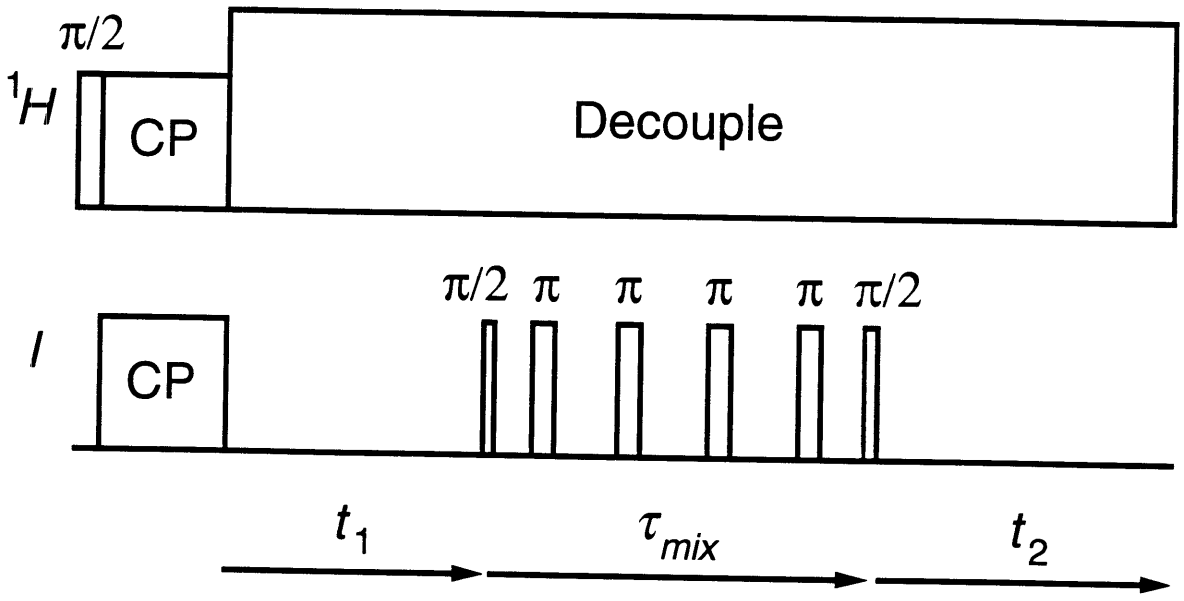
π/2
^1H
CP
Decouple
π/2 π π π π π/2
I
CP
t_1
τ_{mix}
t_2

Figure (2-2). Two-dimensional spectrum of triply-^{13}C-labeled D,L-alanine at 3.720 kHz with a mixing time of 8.6 ms. The polarization is exchanged rapidly among the three ^{13}C resonances in the molecule via the $\approx$ 2 kHz one-bond interactions. The magnitude spectrum is shown here. Since "anti-echo" phase cycling is employed, no sidebands involving non-exchanging resonances appear away from the diagonal.

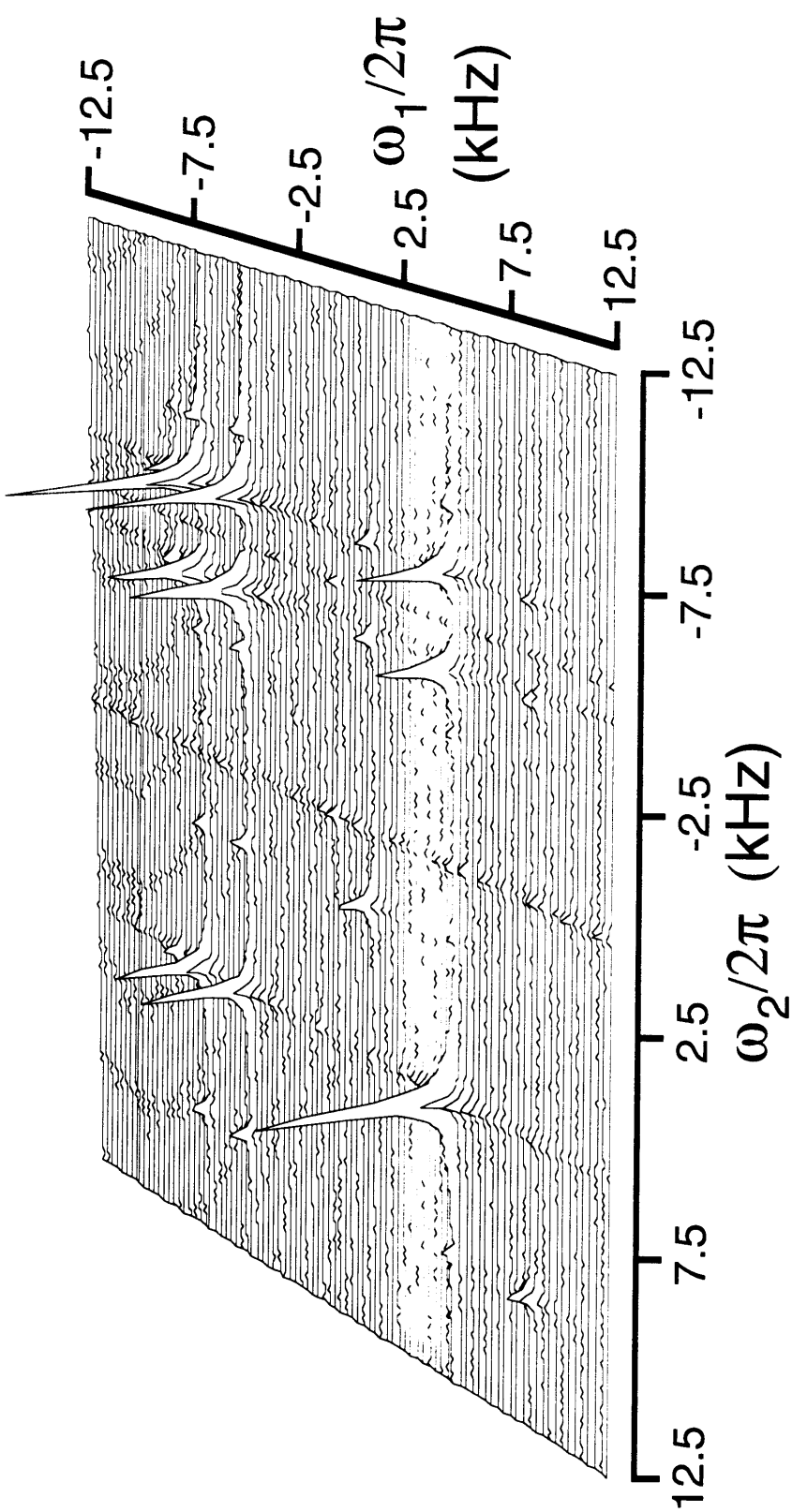
-12.5
-7.5
-2.5
2.5
7.5
12.5
$\omega_1/2\pi$ (kHz)
12.5
7.5
2.5
-2.5
-7.5
-12.5
$\omega_2/2\pi$ (kHz)

Figure (2-3). One-dimensional RFDR pulse sequence. Instead of frequency-labeling during t_1, a state of difference polarization is prepared with selective inversion of the one of the resonances of interest by either a weak pulse or a DANTE sequence. Rotor-synchronized π pulse mixing then promotes exchange among resonances experiencing a difference in polarization between them.

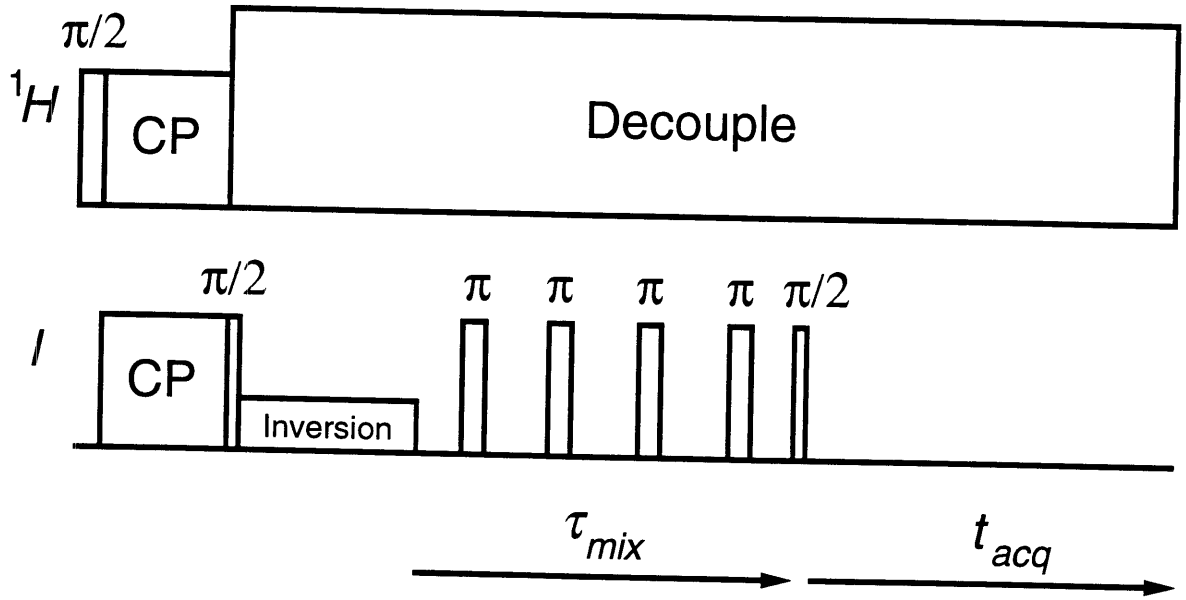
π/2
^1H
CP
Decouple
π/2
π
π
π
π
π/2
I
CP
Inversion
τ_{mix}
t_{acq}

II. Average Hamiltonian Analysis

In the limit of weak dipolar coupling, the effect of applying an arbitrary rotor-synchronized π pulse sequence to a system of coupled homonuclear spins can be treated analytically with either Average Hamiltonian Theory (AHT) [4] or Floquet Theory [3]. Since cyclic time-dependent Hamiltonian operators [11] can be defined for both the chemical shift terms and the RF pulses, the AHT approach provides a particularly transparent means of examining the recoupling dynamics. With the assumption of δ-function π pulses (i. e. instantaneous rotations), only three coherences are involved in longitudinal exchange experiments: the state of difference polarization $1/2\left[I_{z1} - I_{z2}\right]$ between the two spins and their in-phase $\left[I_{x1}I_{x2} + I_{y2}I_{y2}\right]$ and out-of-phase $\left[I_{y1}I_{x2} - I_{x2}I_{y2}\right]$ zero quantum coherences, so the qualitative physics can also by analyzed by inspection of numerical simulations where the spin evolution within the three state subspace is followed [5].

At high magnetic field (e. g. 50-100 MHz for ^{13}C), the chemical shift dispersion of ^{13}C resonances expressed in kHz is comparable to the range of practical spinning frequencies. Consequently, it is not always appropriate to expand the chemical shift contribution to the Hamiltonian in a perturbation series. However, the dipolar coupling between dilute spins is generally small compared to the spinning speed, and it is therefore reasonable to accept the lowest order of a series expansion in powers of the dipolar coupling constant. The difficulty posed by large chemical shift interactions can be solved by establishing an interaction frame defined by the chemical shift terms [7, 12]. Since it is also convenient to define an interaction frame to describe the action of the RF pulses, these transformations lead to a second toggling frame, in which the Magnus expansion can be carried out [11].

In considering the simple case of a spin pair experiencing δ-function π pulses and magic angle spinning, it is useful to divide the internal spin Hamiltonian into three terms which commute with one another at all times [13]:

$$H_{\text{int}}(t) = H_{0a}(t) + H_{0b}(t) + H_1(t)\,, \tag{2-1}$$

where:

$$H_{0a}(t) = \frac{1}{2}\{\delta_1(t) + \delta_2(t)\}[I_{z1} + I_{z2}]\,, \tag{2-2}$$

$$H_{0b}(t) = d_{12}(t) \cdot 2I_{z1}I_{z2}\,, \tag{2-3}$$

$$\begin{aligned} H_1(t) &= H_{CS,1}(t) + H_{D,1}(t) \\ &= \frac{1}{2}\{\delta_1(t) - \delta_2(t)\}[I_{z1} - I_{z2}] - d_{12}(t)[I_{x1}I_{x2} + I_{y1}I_{y2}]\,. \end{aligned} \tag{2-4}$$

As Levitt *et. al.* have pointed out [13], the terms $H_{0a}(t)$ and $H_{0b}(t)$, but not $H_1(t)$, commute with themselves at different times and are therefore "inhomogeneous" in the sense that their influence cancels exactly after multiples of the rotor period [14]. Under MAS, the chemical shift interaction of each spin j has a time-independent isotropic contribution, as well as oscillating terms due to its anisotropy, which depends on the Euler angles $(\alpha_j, \beta_j, \gamma_j)$ of the individual crystallites with respect to the rotor frame:

$$\delta_j(t) = \hat{\delta}_j[m=0] + \sum_{m=-2, m\neq 0}^{m=+2} \hat{\delta}_j[m](\alpha_j, \beta_j)\exp\{im(\omega_R t + \gamma_j)\}\,; \tag{2-5}$$

on the other hand, the dipole-dipole interaction $d_{12}(t)$, whose orientation in the rotor frame is defined by the polar angles (θ,ϕ) of the internuclear vector, is fully amplitude-modulated and, taken alone, averages to zero over one rotor cycle:

$$d_{12}(t) = \sum_{m=-2,m\neq 0}^{m=+2} \hat{d}_{12}[m](\theta)\exp\{im(\omega_R t+\phi)\}. \tag{2-6}$$

In a toggling frame defined by the external RF field, all of the above commutation relations are unchanged under an arbitrary sequence of δ-function π pulses. Therefore, the time evolution operator for the two spin system undergoing rotor-synchronized pulse excitation can be written as follows:

$$\begin{aligned} U(\tau,0) = U_{RF}(\tau,0)\exp\left\{-i\int_0^\tau dt\ \tilde{H}_{0a}(t)\right\} \\ \times\exp\left\{-i\int_0^\tau dt\ \tilde{H}_{0b}(t)\right\} T\exp\left\{-i\int_0^\tau dt\ \tilde{H}_1(t)\right\}, \end{aligned} \tag{2-7}$$

where the toggling frame is defined by the time evolution operator for the RF field alone, $U_{RF}(t,0)$:

$$\tilde{H}_1(t) = U_{RF}^{-1}(t,0)H_1(t)U_{RF}(t,0). \tag{2-8}$$

As in the theory of rotational resonance [12, 13], the important dynamics involve the "homogeneous" term $\tilde{H}_1(t)$, which does not commute with itself at different times. In the particular case where a rotor-synchronized π pulse sequence satisfies the constraint that it leads to the formation of a spin echo

[9, 15], all of the chemical shift terms average to zero over some cycle time τ_C, which is a multiple of the rotor period, i. e. $\tau_C = n\tau_R$, and the chemical shift difference term $\tilde{H}_{CS,1}(t)$ is therefore cyclic in the sense required for the application of AHT [11]. Under these conditions, it is useful to define a second toggling frame via the action of the RF-modulated chemical shift difference term on the dipolar flip-flop Hamiltonian $\tilde{H}_{D,1}(t)$, resulting in the following partition:

$$T\exp\left\{-i\int_0^{\tau_C} dt\ \tilde{H}_1(t)\right\} = \tilde{U}_{CS,1}(\tau,0)\,T\exp\left\{-i\int_0^{\tau_C} dt\ \tilde{\tilde{H}}_{D,1}(t)\right\}, \tag{2-9}$$

where:

$$\tilde{\tilde{H}}_{D,1}(t) = \tilde{U}_{CS,1}^{-1}(t)\tilde{H}_{D,1}(t)\tilde{U}_{CS,1}(t), \tag{2-10}$$

$$\tilde{U}_{CS,1}(\tau,0) = \exp\left\{-i\int_0^{\tau} dt\ \tilde{H}_{CS,1}(t)\right\}. \tag{2-11}$$

The Dyson time-ordering operator T is unnecessary in the definition of $\tilde{U}_{CS,1}(\tau,0)$ because $\tilde{H}_{CS,1}(t)$ is always self-commuting.

The time evolution operator involving $\tilde{H}_{0b}(t)$ has no effect on the density matrix after an integer number of rotor periods. On the other hand, a secular dipolar interaction emerges from $\tilde{\tilde{H}}_{D,1}(t)$ when the RF-modulated chemical shift difference term partly cancels out the coherent averaging effect of MAS. This interaction can be adequately approximated using AHT when the condition $|d_{12}(t)| < \nu_R$ is satisfied, which is generally the case since $|d_{12}(t)|$ is always ≤ 2.5 kHz for ^{13}C-^{13}C couplings.

For example, the application of one π pulse per rotor period refocuses all chemical shift terms following two rotor cycles [15] and also yields an

effective dipolar flip-flop term [3, 4, 16]. The AHT result for the latter, neglecting the chemical shift anisotropy, is the following:

$$\tilde{\bar{H}}_{D,1}^{(0)} = -\bar{d}_{12}\left[I_{x1}I_{x2} + I_{y1}I_{y2}\right] = -\frac{1}{2}\bar{d}_{12}\left[I_{+1}I_{-2} + I_{-1}I_{+2}\right], \tag{2-12}$$

where, with the definitions of the spinning frequency ν_R and the isotropic chemical shift difference $\Delta\delta = \hat{\delta}_1[0] - \hat{\delta}_2[0]$, the effective coupling constant has the form:

$$\bar{d}_{12} = \frac{2}{\pi}\sum_{m=1,2}\hat{d}_{12}[m](\theta)\cos(m\phi)\left\{\frac{\Delta\delta/\nu_R}{m^2-(\Delta\delta/\nu_R)^2}\right\}(-1)^{m-1}\sin\left\{\pi\frac{\Delta\delta}{\nu_R}\right\}. \tag{2-13}$$

More generally, the double toggling frame approach reveals two conditions for recoupling by rotor-synchronized sequences consisting only of π pulses: (1) the coherent averaging of all chemical shift interactions and (2) the recovery of a non-zero dipolar coupling from destructive interference between MAS and the motion of the flip-flop operator in the second toggling frame under the RF-modulated chemical shifts. In order to fulfill the second condition, the latter time-dependence must exhibit some non-zero Fourier component at either ν_R or $2\nu_R$.

In Figure (2-4), the effective coupling for two model crystallite orientations, corresponding physically to the $m = 1$ and $m = 2$ Fourier components of the dipolar interaction, illustrates the recoupling efficiency of the basic echo sequence of one π pulse per rotor period as a function of $(\nu_R/\Delta\delta)$. Though a broad function of the spinning frequency, the effective coupling peaks near the rotational resonance conditions $\Delta\delta = m\nu_R$ in these artificial crystallites. In general, real crystallites involve a linear

combination of these terms, and overall recoupling in a powder sample is most efficient in the region of the primary rotational resonance conditions $m = 1,2$ [13].

At exact rotational resonance $\Delta\delta = M\nu_R$, the effective Hamiltonian reduces to the form:

$$\tilde{\tilde{H}}_{\text{int}}^{(0)} = -\frac{1}{2}\hat{d}_{12}[M](\theta)\cos(M\phi)\left[I_{+1}I_{-2} + I_{-1}I_{+2}\right], \tag{2-14}$$

while the analogous Hamiltonian in the absence of π pulses does not depend on the azimuthal angle ϕ:

$$\tilde{\tilde{H}}_{\text{int}}^{(0)} = -\frac{1}{2}\hat{d}_{12}[M](\theta)\left[I_{+1}I_{-2} + I_{-1}I_{+2}\right]. \tag{2-15}$$

From a physical viewpoint, the angle ϕ is expected to appear in the result, since there is a well-defined phase difference between the pulse sequence and the rotationally induced oscillation of the spin interactions. Indeed, the azimuthal angle appears in the effective coupling recovered by any multiple pulse recoupling sequence where a phase can be defined [1]. A consequence of the phase dependence is that π pulse recoupling is somewhat less efficient than rotational resonance over a powder distribution of crystallites [1, 3, 5].

The effect of any rotor-synchronized π pulse sequence can be analyzed within this framework. For example, the application of one π pulse per N rotor periods also leads to joint rotational and Hahn echoes, and also generates a non-vanishing homonuclear coupling with an increasingly narrow bandwidth in the vicinity of the rotational resonance conditions for increasing N. Likewise, although eight π pulses per rotor period promotes the formation

of an echo every rotor period, it does not recouple interactions in the limit of δ-function π pulses [9]. In the regime where the spinning speed dominates the CSA, it is reasonable to neglect it in the derivation. In the slow spinning regime, the coupling constant $\bar{d}_{12}$ becomes a function of the RF-modulated CSA term, and its influence can be included within the same framework as the isotropic chemical shifts. In practice, however, it is most convenient to explore the influence of the CSA tensors using simulations.

In the case of total correlation spectroscopy (TOCSY) [17], a method broadly employed in solution NMR spectroscopy, a sequence of π pulses eliminates chemical shifts, but leaves the complete homonuclear J coupling $J\vec{I}_1\cdot\vec{I}_2$ intact in the limit of rapid pulsing compared to the chemical shift difference frequencies. In solution experiments, the homonuclear J coupling is sufficient to promote either the transverse or longitudinal exchange of spin polarization, i. e. the mixing is isotropic. In rotating solids, however, the mixing sequence recouples only the flip-flop part of the interaction, while the rest of the dipolar coupling, $d_{12}(t)\cdot 2I_{z1}I_{z2}$, vanishes exactly over each rotor cycle. Under these conditions, transverse magnetization undergoes dephasing, but not exchange [4]:

$$\rho(\tau) = I_{x1}\cos\left\{2\pi\cdot\bar{d}_{12}\tau/2\right\} + 2I_{z1}I_{y2}\sin\left\{2\pi\cdot\bar{d}_{12}\tau/2\right\}. \qquad (2\text{-}16)$$

Under δ-function π pulses, or in the absence of RF pulses, exchange of the transverse magnetizations is forbidden over multiples of the rotor period, since only the flip-flop portion of the spin-spin interaction is recovered. Therefore, in order to use π pulse recoupling in two-dimensional spectroscopy with transverse mixing, π/2 pulses must be applied for coherence transfer

[18]. On the other hand, the flip-flop coupling directly couples longitudinal polarizations:

$$\rho(\tau) = I_{z1}\cos^2\left\{2\pi\cdot\bar{d}_{12}\tau/2\right\} + I_{z2}\sin^2\left\{2\pi\cdot\bar{d}_{12}\tau/2\right\} + \left[I_{y1}I_{x2} - I_{x1}I_{y2}\right]\sin\left\{2\pi\cdot\bar{d}_{12}\tau\right\}. \tag{2-17}$$

so longitudinal exchange is the most convenient and straightforward means of acquiring two-dimensional spectra. In addition, the spin trajectory develops twice as rapidly in longitudinal experiments, which are therefore advantageous for the examination of weak interactions. In one-dimensional RFDR experiments, the corresponding trajectory begins with a state of inverted relative polarization:

$$\rho(\tau) = \frac{1}{2}\left[I_{z1} - I_{z2}\right]\cos\left\{2\pi\cdot\bar{d}_{12}\tau\right\} + \left[I_{y1}I_{x2} - I_{x1}I_{y2}\right]\sin\left\{2\pi\cdot\bar{d}_{12}\tau\right\}. \tag{2-18}$$

In all of these trajectories, differential effective rates of decay among the various coherences perturb the trajectories, particularly when the decay rates are comparable to the dipolar coupling [13]. A simple empirical approach for selecting decay rates in spin echo experiments is described in the fourth chapter. Kubo and McDowell have discussed the approximation of the decay rates of homonuclear two spin coherences as the sum of the relevant single spin rates [19], which is valid in limit where the fluctuating fields causing the disappearance of the signals are independent at each spin. For example, if the spin coherence I_{z1} is taken to disappear exponentially with decay constant Γ_{z1}, and the decay constant of I_{x2} is Γ_{x2}, then the corresponding decay parameter for the two spin coherence $I_{z1}I_{x2}$ is the sum $\{\Gamma_{z1}+\Gamma_{x2}\}$. In

the numerical simulations of longitudinal exchange discussed here, this approximation is applied to all of the spin coherences. For a two spin system, a total of fifteen coherences are necessary to span the density matrix in finite pulse simulations of longitudinal exchange.

Figure (2-4). Effective dipolar coupling constant as a function of the dimensionless parameter $\nu_R/\Delta\delta$ for two artificial single crystallite orientations, where ν_R is the spinning frequency and $\Delta\delta$ is the difference between the isotropic chemical shift frequencies of the two spins. The smooth curves provide the results predicted by the AHT treatment; the additional points correspond to the interaction derived from the exact time evolution operator. For $m = 1$, $d_{12,|1|}(\theta) = 1$ kHz and $d_{12,|2|}(\theta) = 0$ kHz; for $m = 2$, $d_{12,|1|}(\theta) = 0$ kHz and $d_{12,|2|}(\beta) = 1$ kHz. In all cases $\phi = 0$. The greatest extent of dipolar recoupling is achieved in the neighborhood of the rotational resonance conditions. Real crystallites within an isotropic powder distribution involve various linear combinations of these basic contributions.

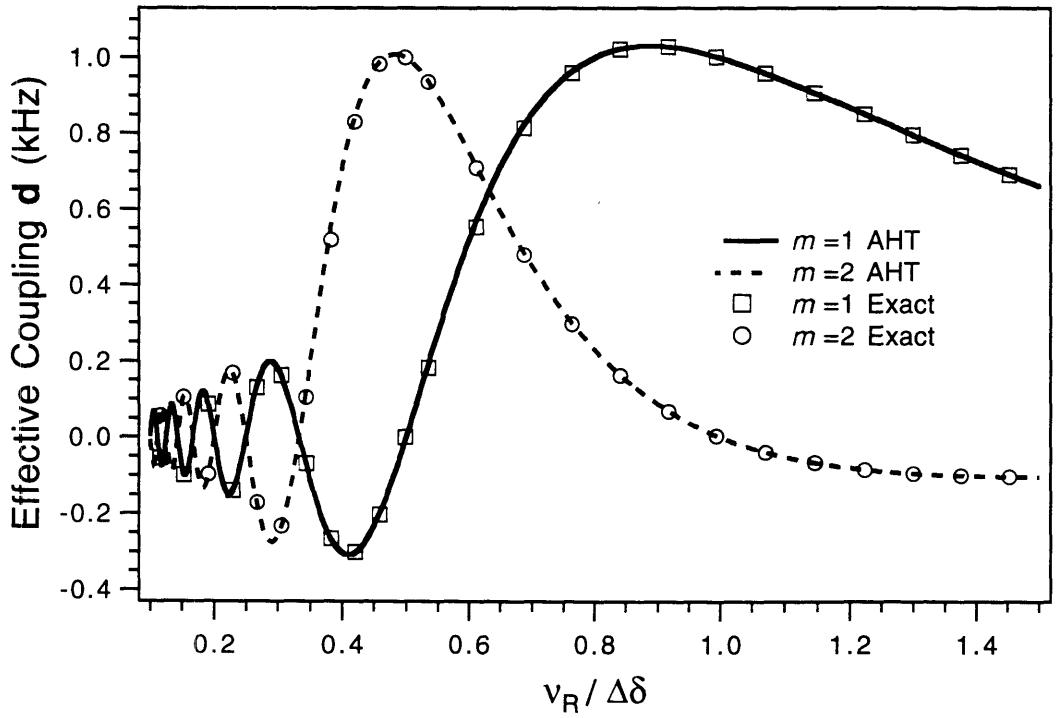
Effective Coupling d (kHz)
1.0
0.8
0.6
0.4
0.2
0.0
-0.2
-0.4
0.2
0.4
0.6
0.8
1.0
1.2
1.4
$\nu_R / \Delta\delta$
m =1 AHT
m =2 AHT
m =1 Exact
m =2 Exact

III. Longitudinal Exchange Experiments

Figure (2-5) demonstrates the longitudinal exchange trajectory of 1,3-^{13}C-^{15}N-D,L-alanine at 4.8 kHz spinning speed [10]. In the numerical simulations, the anomalously short T_1 of the methyl carbon (i. e. 65 ms in these experiments) must be included in the analysis [20]. Likewise, although the ^{13}C-^{1}H coupling is relatively small for both resonances, additional signal decay is observed under the π pulse sequence. In Figure (2-5a), the decay of the z polarizations is observed. With the dipolar coupling (475 Hz) included, parameters are chosen for the losses of the single spin coherences during the pulse train in order to match the experimental rates of longitudinal decay. An additional effective T_2 parameter is also introduced in order to describe the somewhat more rapid transverse dephasing of the single spin coherences during periods of free evolution in the pulse cycle (not shown). Since the dipolar interaction also contributes to the decay trajectories, it is necessary to include an initial estimate of its magnitude in the simulations. Figure (2-5b) illustrates the good agreement which is obtained between the observed trajectory with the inversion of the CO_2H group and the simulated spin evolution, demonstrating that relatively large dipole-dipole couplings can be measured in the presence of differential signal losses and a rapid T_1 process.

For multiple spin applications, the dynamics of all spins which are strongly coupled and their dipole-dipole interactions must be considered simultaneously. Under most circumstances, the exchange trajectories are dominated by the largest interactions. Figure (2-6) illustrates experimental trajectories obtained with triply-^{13}C-labeled alanine and two alternative simulation approaches. With the perturbation of the $^{13}CO_2H$ polarization in Figure (2-6b), it exchanges rapidly with the neighboring α-^{13}CH site that is

coupled to it via the one-bond interaction of 2.2 kHz and then with the methyl carbon. The direct interaction between the $^{13}CO_2H$ and $^{13}CH_3$ groups of 475 Hz has a small influence on the transfer of polarization among the spins. For computational convenience, the finite pulse simulation does not include signal losses, while the δ-function pulse calculation does include them. At short times, the finite pulse widths have a significant effect in this spin system, but at longer times, the δ-function pulse simulation is in better agreement because it includes the influence of the empirically observed rates of signal decay which are important at long times.

In the case of a spin pair, it is often most valuable to measure relatively weak couplings in order to gain the most important information concerning molecular conformations [21, 22]. Doubly-^{13}C-labeled 1,4-^{13}C-$^{15}NH_3$-glycylglycine hydrochloride monohydrate provides a suitable test case. Its crystal structure is known from neutron and X-ray diffraction [23, 24], and the labeled homonuclear spin pair has an internuclear separation of 4.56 Å, which corresponds to a dipole-dipole coupling constant of 80.0 Hz.

With the initial choice of 80 Hz as the coupling constant, the decay parameters for the longitudinal and transverse spin coherences under the echo sequence are selected to match the simulations with the observed trajectories shown in Figure (2-7). In the sample under study, which is 10% diluted in natural abundance material, intermolecular couplings are also expected to play a role in the experimental exchange trajectories because there are three intermolecular distances ≤ 5 Å in addition to the intramolecular coupling, i. e. with separations 4.26 Å, 4.22 Å, and 4.71 Å, all corresponding to dipolar coupling constants of similar magnitude.

The use of a second moment expansion is helpful in deriving an empirical correction for the intermolecular effects [25, 26]. At short times,

the longitudinal exchange trajectory of spin 1, for example, proceeds as follows:

$$\left\langle\left\langle I_{z1}(\tau)\right\rangle\right\rangle \approx 1-\frac{1}{4}(2\pi)^2\left\{\left\langle\overline{d}_{12}^2\right\rangle+\sum_{j\neq 1,2}\left\langle\overline{d}_{1j}^2\right\rangle p_j\right\}\tau^2 , \tag{2-19}$$

where the outer brackets $\langle\cdots\rangle$ indicate averaging over the powder distribution. The parameters p_j are the populations of the intermolecular ^{13}C spins. Here the parameters are $p_j = 0.1$ with the ten-fold dilution of the sample. The averaged moments $\left\langle\overline{d}_{ij}^2\right\rangle$ involve the chemical shift parameters according to Eq. (2-13) and are directly proportional to d_{ij}, the dipolar coupling constant. This expansion suggests the following empirical correction for the intermolecular effects in the observed exchange trajectories:

$$x_{12}^{observed}(\tau) = x_{12}^{actual}(\tau)+\sum_{j\neq 1,2} x_{1j}^{actual}(\tau)p_j , \tag{2-20}$$

where $\left\langle\left\langle I_{z1}(\tau)\right\rangle\right\rangle = 1-x_{12}(\tau)$. This approach is valid for times which are relatively short compared to the inverse of the largest dipolar coupling constant involved. In the case of the glycylglycine sample, Eq. (2-20) implies that the true exchange process $x_{12}^{actual}(\tau)$ is overestimated by 39% at each point. The exchange data shown in Figure (2-8) are corrected accordingly, leading to good agreement with the simulated finite pulse trajectory employing a coupling constant of 85 Hz, which implies an underestimate of 0.1 Å in the internuclear distance. Without the correction, the experimental results imply a coupling constant of ≈ 95 Hz, which underestimates the interatomic separation in the molecule by 0.3 Å, a significant error. More generally, when the crystal structure is unknown, experiments can be

performed as a function of dilution in order to vary the constants p_j. Otherwise, in relative small molecules, it is difficult to distinguish between weak intra- and inter-molecular interactions.

Figure (2-8b) shows the somewhat modified exchange trajectory which is obtained when the system is perturbed at 10.67 ms by the elimination of the zero-quantum (ZQ) coherences, which is achieved by briefly removing the proton decoupling field to destroy all spin coherences of transverse character. This experiment has two purposes. First, it provides evidence that the decay parameters for the spin coherences are being selected realistically, since these parameters, together with the dipolar coupling constant, determines how much zero-quantum coherence is present during the trajectory. Although the ZQ coherences are not directly observable, the effect of eliminating them in the middle of the exchange trajectory has a direct impact on the subsequent dynamics. In limit of very rapid zero-quantum relaxation, little ZQ coherence is present at all times, and accordingly attenuating it has little effect. On the other hand, if its decay rate is negligible, then the trajectory of Eq. (2-18) is modified as follows:

$$\begin{aligned}\Delta\rho(\tau_1+\tau_2) &= \frac{1}{2}\left[I_{z1}-I_{z2}\right]\sin\left\{\bar{d}_{12}\tau_1\right\}\sin\left\{\bar{d}_{12}\tau_2\right\} \\ &+\left[I_{y1}I_{x2}-I_{x1}I_{y2}\right]\sin\left\{\bar{d}_{12}\tau_1\right\}\cos\left\{\bar{d}_{12}\tau_2\right\},\end{aligned} \tag{2-21}$$

where $\Delta\rho(\tau_1+\tau_2)$ signifies the difference between the density matrix obtained with and without the removal the two spin coherences at time τ_1. The simultaneous agreement of the simulations with the experimental points in both the cases $\tau_1 = 0$ ms and $\tau_1 = 10.67$ ms provides additional confirmation that the spin dynamics are being described correctly. A second

application of this approach is the filtering of signals via the ZQ coherences. Clearly, no signal is obtained from the difference trajectory $\Delta\rho(\tau_1 + \tau_2)$ when the coupling constant d_{12} vanishes, so $\Delta\rho(\tau_1 + \tau_2)$ provides a filtered signal which is maximized when $\tau_1 \approx 1/d_{12}$ and $\tau_1 = \tau_2$.

Sample Preparation. The triply-labeled 1,2,3-^{13}C-D,L-alanine sample in Figure (2-2) was purchased from MSD Isotopes and used without further purification. The 1,3-^{13}C-^{15}N-D,L-alanine sample (MSD Isotopes Inc.) was recrystallized from water by slow evaporation with ten-fold dilution in natural abundance material, and likewise for the 1,2,3-^{13}C-L-alanine sample (Cambridge Isotopes Inc., Cambridge, MA) used for the experiment shown in Figure (2-6). The sample for the long distance was polycrystalline 1,4-^{13}C-$^{15}NH_3$-glycylglycine hydrochloride monohydrate, which was also ten-fold diluted.

NMR Experiments. All experiments discussed here were carried out at 79.9 MHz for ^{13}C using a home-built NMR spectrometer and double resonance probes for magic angle spinning employing commercial spinning assemblies (Doty Scientific, Columbia, SC). Mixing was performed in all cases with the rotor-synchronized spin echo sequence of one π pulse per rotor period. It is necessary to make corrections for the imperfect creation of an inverted state of relative polarization (usually $\leq 5-10\%$ error) in processing one-dimensional data, and in addition the contribution from uncoupled spins must be subtracted from the experimental data.

The 2D spectrum shown in Figure (2-2) was acquired with a 7mm rotor spinning at 3.720 kHz with a total mixing time of 8.6 ms. The spectrum was acquired with "anti-echo" phase cycling [27], which eliminates sidebands from non-exchanging peaks away from the diagonal when the mixing period is

rotor-synchronized. The magnitude spectrum is shown. The *XY*-8 phase alternation scheme for the compensation of pulse errors was also applied [28].

All of the one-dimensional experiments on alanine were carried out at 4.800 kHz spinning speed with a 7 mm Doty stator using one π pulse per rotor period with *XY*-16 phase cycling and selective inversion of the CO_2H resonance via the DANTE pulse sequence [29]. The π pulses employed in mixing were 20.0 μs, and the ^1H $\pi/2$ pulse 3.1 μs, yielding the large Hartmann-Hahn mismatch ratio of 3.2.

The glycylglycine experiments were performed at 9.000 kHz spinning frequency using a 5 mm high-speed stator from Doty with π pulse lengths of 15.6 μs for ^{13}C and 5.6 μs for ^1H, yielding a mismatch ratio of 2.8. These trajectories were also acquired with *XY*-16 cycling and one π pulse per rotor period. The spinning speed of 9 kHz was selected in order to reduced the influence of the CSA tensors on the results and place the system between the $m = 1$ and $m = 2$ rotational resonance conditions. The chemical shift difference between the 1-$^{13}CO_2$ and the 4-$^{13}CH_2$ nuclei is 10.28 kHz in these experiments.

Numerical Simulations. In the case of doubly-labeled alanine, a decay parameter is chosen to account for the loss of the methyl group polarization during the π pulses, and an effective zero-quantum relaxation rate of 32 msec is extracted from the transverse echo trajectory. The δ-function pulse calculations for the three spin alanine case include the longitudinal losses within a similar framework and omit the additional transverse decay rates. Because the spinning rate of 4.800 kHz is relatively slow compared to the CSA tensor parameters, these are included in the numerical simulations. For L-alanine, the orientations of the CSA tensors in the crystal reference frame [30] are known from single crystal NMR studies [31] and explicitly included

in the three spin calculations, while the CSA orientations for D,L-alanine are estimated from those of the L-alanine case. The two spin alanine trajectories fit a dipolar coupling constant of 480 Hz (2.51 Å), which is slightly shorter than the value of 475 Hz (2.52 Å) given by the X-ray crystal structure [32].

For glycylglycine, only the anisotropic chemical shifts of the CO_2H resonance (principal values of -150.9, -36.1, and +6.6 ppm) are included in the calculations, since the α-^{13}C CSA is quite small relative to the 9 kHz spinning speed. The isotropic shift the α-^{13}C line is 68.6 ppm. Although the trajectories are virtually insensitive to the orientation of the CSA in the molecular reference frame, again because of fast MAS, it is estimated from the known molecular orientations of carboxyl CSA tensors derived from single crystal studies [33]. During the pulses, the decay parameters $\Gamma_{CO2H} = 0.024$ kHz and $\Gamma_{CH2} = 0.357$ kHz are chosen based on the data in Figure (2-7), while the single spin effective transverse decay rates are $\Gamma_{CO2H} = 0.024$ kHz and $\Gamma_{CH2} = 0.008$ kHz during periods of free evolution between the RF pulses. With the correction of the experimental points for the overestimate of exchange from intermolecular couplings (as discussed above), the results fit a coupling constant of 85 Hz quite well, which underestimates the internuclear distance of 4.56 Å obtained from single crystal diffraction studies [23, 24] by only 0.1 Å.

Figure (2-5). One-dimensional inversion exchange data for 1,3-^{13}C-^{15}N-D,L-alanine at 4.800 kHz spinning speed with one π pulse per rotor period: (a) decay of sum polarization, (b) decay of difference polarization, revealing the magnitude of the dipolar interaction. In (b) the CO_2 resonance is inverted via the DANTE technique. The observation of the sum polarization state, i. e. the initial condition with no spin inversion, is useful for ascertaining the behavior of the resonances under the pulse sequences, since the dipolar flip-flop interaction affects only differences in spin polarizations. The simulated results include finite pulse effects.

(a)

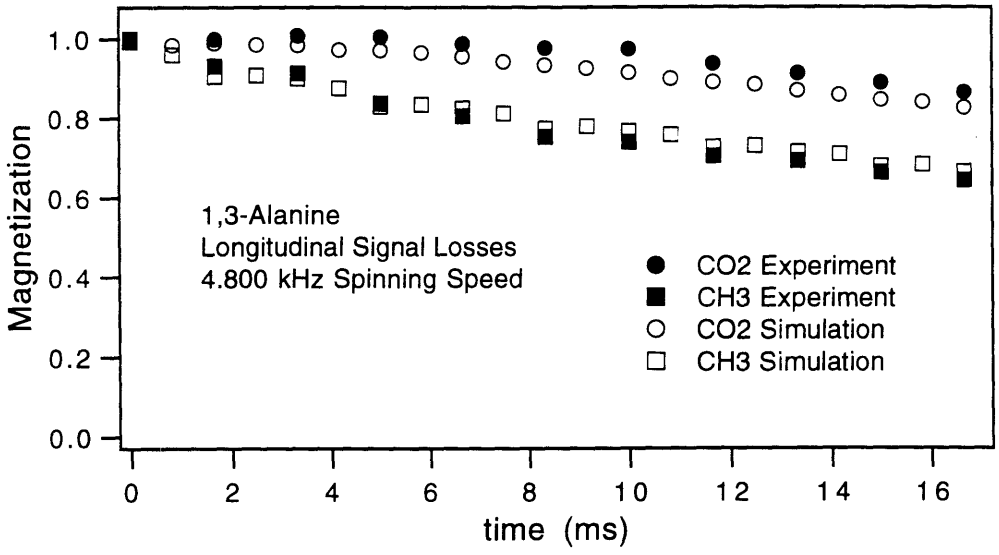
1.0
0.8
0.6
0.4
0.2
0.0
Magnetization
1,3-Alanine
Longitudinal Signal Losses
4.800 kHz Spinning Speed
CO2 Experiment
CH3 Experiment
CO2 Simulation
CH3 Simulation
0
2
4
6
8
10
12
14
16
time (ms)

(b)

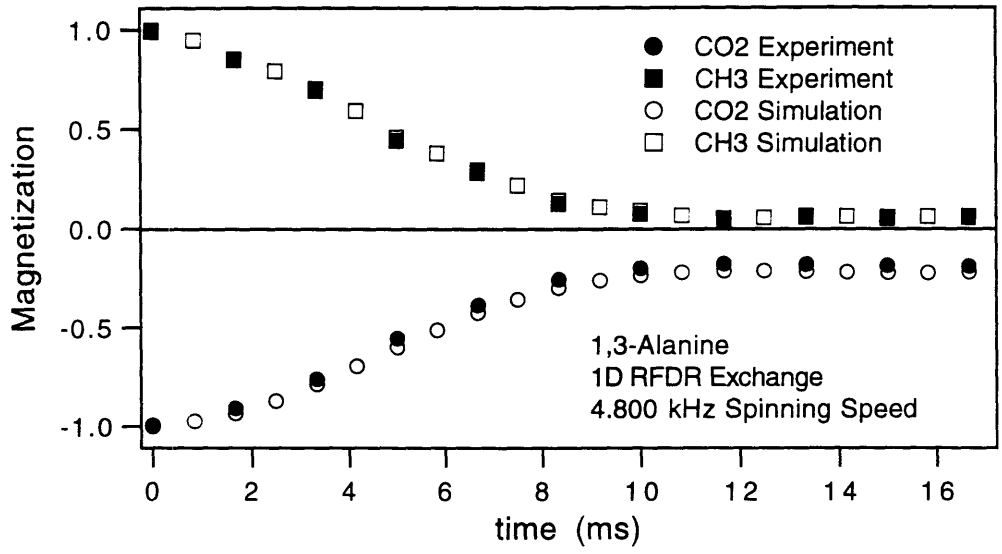
1.0
0.5
0.0
-0.5
-1.0
Magnetization
CO2 Experiment
CH3 Experiment
CO2 Simulation
CH3 Simulation
1,3-Alanine
1D RFDR Exchange
4.800 kHz Spinning Speed
0
2
4
6
8
10
12
14
16
time (ms)

Figure (2-6). One-dimensional inversion exchange data for 1,2,3-^{13}C-L-alanine at 4.800 kHz spinning speed with one π pulse per rotor period and inversion of the CO_2 resonance. The creation of the inverted state is imperfect, and the experimental data and simulations are scaled to the observed values of their relative initial magnitudes: (a) decay of sum polarization, (b) decay of the spin polarizations with inversion of the CO_2 resonance.

(a)

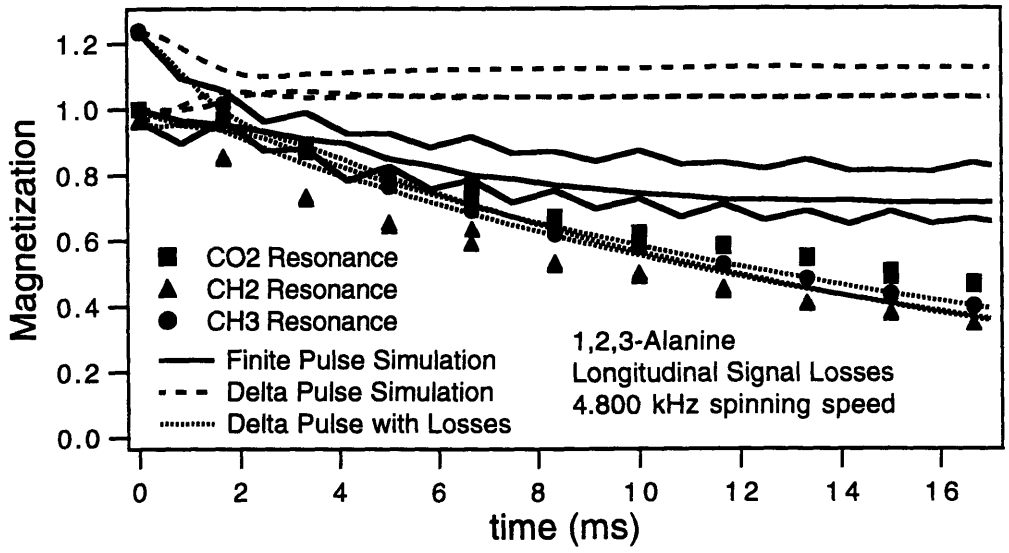
Magnetization
1.2
1.0
0.8
0.6
0.4
0.2
0.0
CO2 Resonance
CH2 Resonance
CH3 Resonance
Finite Pulse Simulation
Delta Pulse Simulation
Delta Pulse with Losses
1,2,3-Alanine
Longitudinal Signal Losses
4.800 kHz spinning speed
0
2
4
6
8
10
12
14
16
time (ms)

(b)

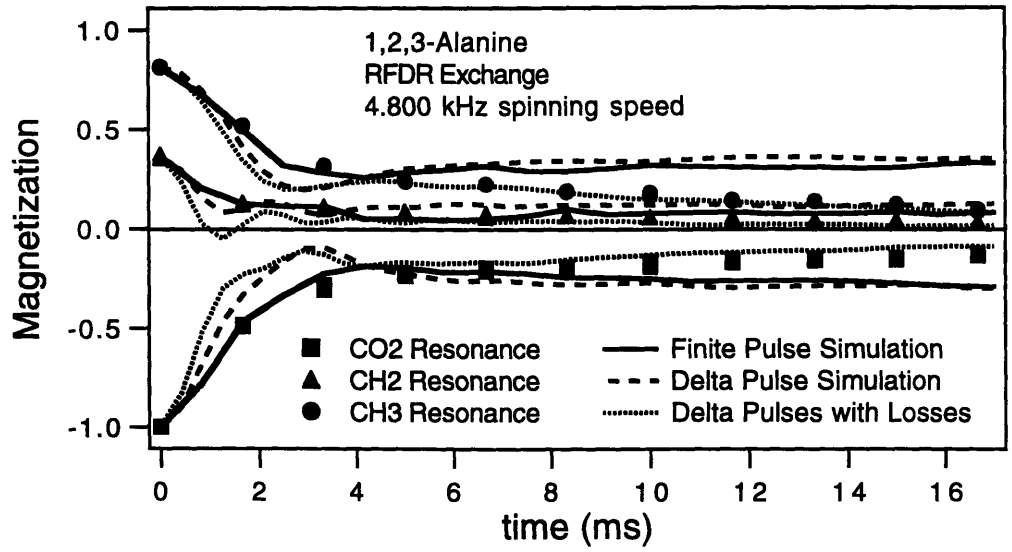
Magnetization
1.0
0.5
0.0
-0.5
-1.0
1,2,3-Alanine
RFDR Exchange
4.800 kHz spinning speed
CO2 Resonance
CH2 Resonance
CH3 Resonance
Finite Pulse Simulation
Delta Pulse Simulation
Delta Pulses with Losses
0
2
4
6
8
10
12
14
16
time (ms)

Figure (2-7). One-dimensional results for the decay of spin coherences in the 1,4-^{13}C-glycylglycine sample at 9.000 kHz: (a) losses of the spin polarizations beginning with the sum polarization state, and (b) decay of the state of initially prepared transverse spin magnetizations.

(a)

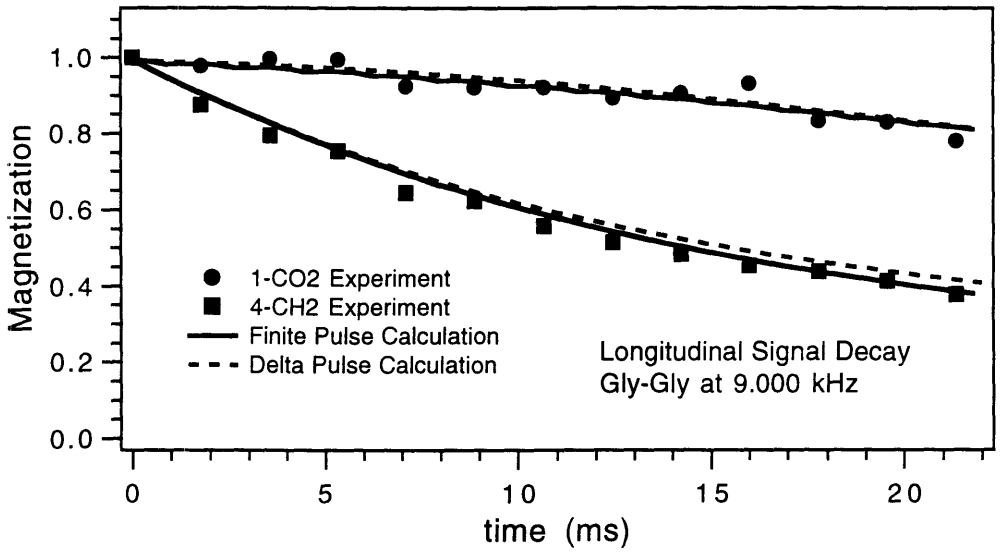
Magnetization
1.0
0.8
0.6
0.4
0.2
0.0
0
5
10
15
20
time (ms)
1-CO2 Experiment
4-CH2 Experiment
Finite Pulse Calculation
Delta Pulse Calculation
Longitudinal Signal Decay
Gly-Gly at 9.000 kHz

(b)

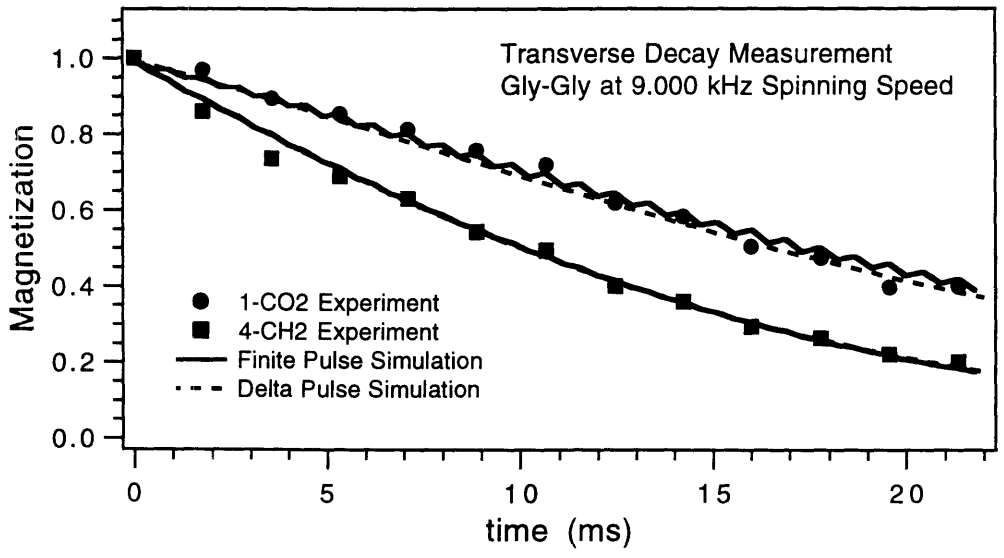
Magnetization
1.0
0.8
0.6
0.4
0.2
0.0
0
5
10
15
20
time (ms)
Transverse Decay Measurement
Gly-Gly at 9.000 kHz Spinning Speed
1-CO2 Experiment
4-CH2 Experiment
Finite Pulse Simulation
Delta Pulse Simulation

Figure (2-8). One-dimensional results for inversion exchange in the glycylglycine sample, where the CO_2H line is inverted via the DANTE sequence: (a) longitudinal exchange trajectory (experimental results and both δ-function and finite pulse calculations), and (b) the same trajectory obtained with the elimination of the ZQ coherences at 10.67 ms via the brief removal of the decoupling field (for two rotor periods).

(a)

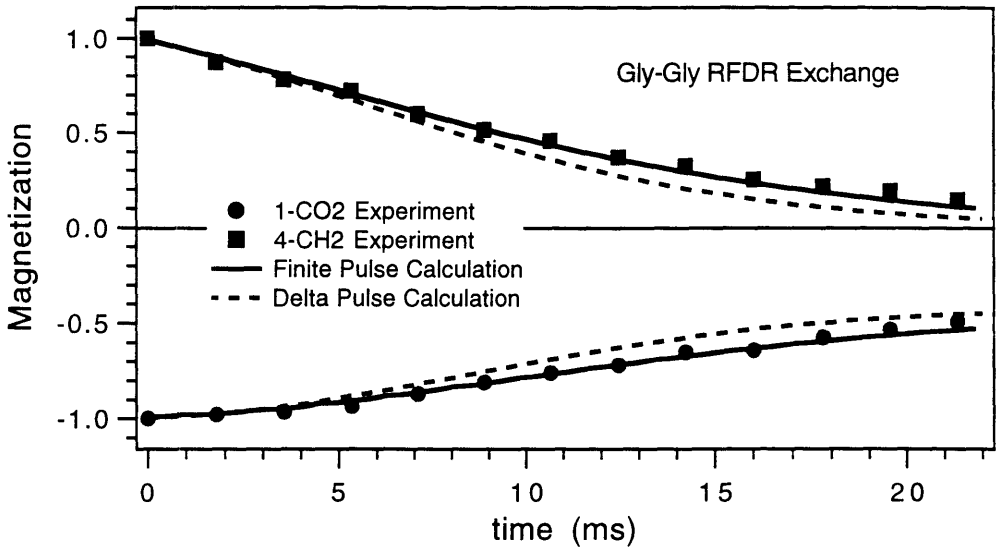
Gly-Gly RFDR Exchange
1-CO2 Experiment
4-CH2 Experiment
Finite Pulse Calculation
Delta Pulse Calculation
Magnetization
1.0
0.5
0.0
-0.5
-1.0
0
5
10
15
20
time (ms)

(b)

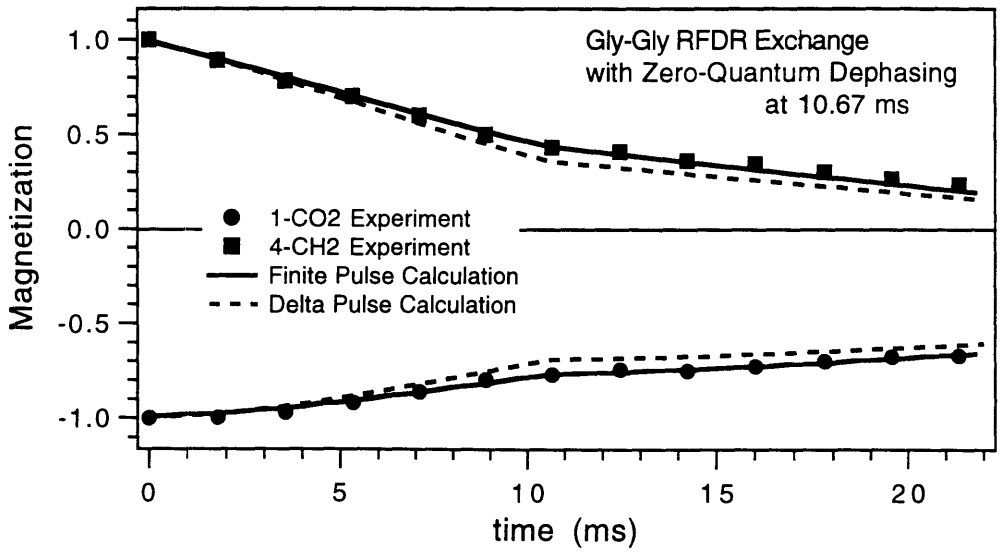
Gly-Gly RFDR Exchange
with Zero-Quantum Dephasing
at 10.67 ms
1-CO2 Experiment
4-CH2 Experiment
Finite Pulse Calculation
Delta Pulse Calculation
Magnetization
1.0
0.5
0.0
-0.5
-1.0
0
5
10
15
20
time (ms)

IV. Conclusion

The recoupling of homonuclear interactions via spin echo sequences and the observation of 1D and 2D longitudinal exchange trajectories among ^{13}C-labeled spins is a simple and accurate means of determining internuclear distances in favorable cases. Its advantages include tolerance of the results to RF pulse errors, such as the RF inhomogeneity (up to at least $\leq 5\%$) and phase transients, as well as the simplicity of implementation and analysis. For weak couplings, the δ-function pulse calculations yield reasonable agreement with the experimental data and are relatively easy to perform using the established method for selecting decay parameters.

The advantages of the longitudinal exchange approach include the rapid evolution of the spin polarizations (twice as fast as in transverse experiments) and their relatively slow decay during the pulse sequence. The major disadvantages of the π pulse approach as a non-selective recoupling method are the losses of spin magnetizations experienced with an insufficiently strong proton decoupling field and the dependence of the effective coupling of the chemical shift parameters. In practice, this approach is most suitable for large differences in isotropic chemical shifts. In these cases, the use of fast spinning eliminates the dependence of the trajectories on the chemical shift anisotropy. Particularly with improved probe technology, the accurate measurement of distances greater than 5 Å using this method appears feasible.

References for Chapter 2.

[1] A. E. Bennett, R. G. Griffin, and S. Vega, NMR Basic Principles and Progress **33**, 1 (1994).

[2] J. M. Griffiths and R. G. Griffin, Anal. Chim. Acta. **283**, 1081 (1993).

[3] T. Gullion and S. Vega, Chem. Phys. Lett. **194**, 423 (1992).

[4] A. E. Bennett, J. H. Ok, R. G. Griffin, and S. Vega, J. Chem. Phys. **96**, 8624 (1992).

[5] D. K. Sodickson, M. H. Levitt, S. Vega, and R. G. Griffin, J. Chem. Phys. **98**, 6742 (1993).

[6] D. P. Raleigh, M. H. Levitt, and R. G. Griffin, Chem. Phys. Lett. **146**, 71 (1988).

[7] M. G. Columbo, B. H. Meier, and R. R. Ernst, Chem. Phys. Lett. **146**, 189 (1988).

[8] J. Jeener, B. H. Meier, P. Bachmann, and R. R. Ernst, J. Chem. Phys. **71**, 4546 (1979).

[9] J. H. Ok, R. G. S. Spencer, A. E. Bennett, and R. G. Griffin, Chem. Phys. Lett. **197**, 389 (1992).

[10] J. M. Griffiths, K. V. Lakshmi, A. E. Bennett, J. Raap, C. M. van der Wielen, J. Lugtenburg, J. Herzfeld, and R. G. Griffin, J. Am. Chem. Soc. **116**, 10178 (1994).

[11] U. Haeberlen, *High Resolution NMR in Solids: Selective Averaging* (Academic Press, New York, 1976).

[12] Z. H. Gan and D. M. Grant, Mol. Phys. **67**, 1419 (1989).

[13] M. H. Levitt, D. P. Raleigh, F. Creuzet, and R. G. Griffin, J. Chem. Phys. **92**, 6347 (1990).

[14] M. Maricq and J. S. Waugh, J. Chem. Phys. **70**, 3300 (1979).

[15] E. T. Olejniczak, S. Vega, and R. G. Griffin, J. Chem. Phys. **81**, 4804 (1984).

[16] O. Weintraub, S. Vega, C. Hoelger, and H. H. Limbach, J. Mag. Res. A **109**, 14 (1994).

[17] L. Braunschweiler and R. R. Ernst, J. Mag. Res. **53**, 512 (1983).

[18] O. Weintraub, S. Vega, C. Hoelger, and H. H. Limbach, J. Mag. Res. **110**, 12 (1994).

[19] A. Kubo and C. A. McDowell, J. Chem. Soc. Faraday Trans. **84**, 3713 (1988).

[20] K. Akasaka, S. Ganapathy, C. A. McDowell, and A. Naito, J. Chem. Phys. **78**, 3567 (1983).

[21] D. P. Raleigh, F. Creuzet, S. K. Das Gupta, M. H. Levitt, and R. G. Griffin, J. Am. Chem. Soc. **111**, 4502 (1989).

[22] R. G. S. Spencer, K. J. Halverson, M. Auger, A. E. McDermott, R. G. Griffin, and P. T. Lansbury, Biochem. **30**, 10382 (1991).

[23] R. Parthasarathy, Acta. Cryst. B **25**, 509 (1969).

[24] T. F. Koetzle, W. C. Hamilton, and R. Parthasarathy, Acta. Cryst. B **28**, 2083 (1972).

[25] Y. Pan, T. Gullion, and J. Schaefer, J. Mag. Res. **90**, 330 (1990).

[26] M. Mehring, *Principles of High Resolution NMR in Solids* (Springer-Verlag, Berlin, 1983).

[27] A. P. M. Kentgens, E. deBoer, and W. S. Veeman, J. Chem. Phys. **87**, 6859 (1987).

[28] T. Gullion, D. B. Baker, and M. S. Conradi, J. Mag. Res. **89**, 479 (1990).

[29] P. Caravatti, G. Bodenhausen, and R. R. Ernst, J. Mag. Res. **55**, 88 (1983).

[30] M. S. Lehmann, T. F. Koetzle, and W. C. Hamilton, J. Am. Chem. Soc. **94**, 2657 (1972).

[31] A. Naito, S. Ganapathy, K. Akasaka, and C. A. McDowell, J. Chem. Phys. **74**, 3190 (1981).

[32] J. Donohue, J. Am. Chem. Soc. **72**, 949 (1950).

[33] W. S. Veeman, Prog. NMR Spectroscopy **16**, 193 (1984).

Chapter 3.

Two-Dimensional Dipolar Correlation Spectroscopy of Bacteriorhodopsin

I. Introduction

Bacteriorhodopsin (bR) is a 26 kD integral membrane protein found in the bacterium *Halobacterium salinarium*, and it serves as a light-driven proton pump [1-4]. Five of its seven transmembrane alpha helices enclose a channel for ion transport across the cell membrane. Approximately in the middle of the channel, a retinal chromophore is bound to the end of the sidechain of lys-216 through a Schiff base linkage. Following the absorption of light, the retinal undergoes conformational changes which are coupled to the expulsion of protons from the cytoplasm to the exterior of the cell [5, 6].

In the plane of the lipid bilayer, the purple membrane fraction of the *Halobacterium*, which contains bacteriorhodopsin in large concentration, has the unusual property that it forms two-dimensional crystals consisting only of ordered arrays of bR molecules appearing in clusters of three surrounded by lipids. Henderson *et. al*. have provided a detailed structural model of the ground state of bR based on electron microscopy and other available information [2]. Still, there is significant uncertainty in the resolution normal to the bilayer (≈ 3.5 Å in lateral resolution, but only ≈ 10 Å in the normal direction) because the purple membrane is not ordered in this direction. Therefore, it remains important to examine key structural aspects of the retinal binding pocket using alternative methods which contribute information at the atomic level. Furthermore, there is far greater uncertainty about the structural changes that occur during the bR photocycle among the various amino acid sidechains present in the retinal binding pocket. These structural changes are intimately related to the mechanism of proton transport [6].

Solid state NMR spectroscopy has been used extensively in the study of bacteriorhodopsin [7] and, in particular, for investigations of the structure of the retinal chromophore and the Schiff base linkage in the bR ground states (i. e. bR_{555} and bR_{568} – where the subscript indicates the absorption maximum in nm) [8-11] and the deprotonated M intermediate of the bR photocycle [12, 13]. Other methods which have found utility in examining the photointermediates include Fourier transform infared (FTIR) [14, 15] and resonance Raman spectroscopy [16, 17]. These approaches, however, do not provide chemical information about individual atoms, and indeed the results are subject to misleading interpretations. For example, FTIR results have implied that the sidechain carboxyl group of the asp-212 residue probably becomes protonated in the M state [14], but ^{13}C chemical shifts [18] point convincingly to a deprotonated state. This conclusion is also supported by mutagenesis studies, as discussed by Henderson [2]. In combination with all of these spectroscopic techniques, site-directed mutagenesis has played a major role in elucidating the mechanistic features of proton pumping [4, 18].

Although ^{13}C and ^{15}N chemical shifts have been useful in elucidating protonation states and conformational information [8, 10], rotational resonance experiments have also been applied to samples labeled with ^{13}C spin pairs [9, 11]. These experiments provide direct measurements of homonuclear internuclear distances in favorable cases [19, 20]. Unfortunately, in many cases, it is difficult to match the rotational resonance condition or to create an inverted state of relative polarization in the spin pair of interest. Samples with several ^{13}C-labeled nuclei provide a further impetus for the development of other approaches. For these cases it is important develop more general dipolar recoupling techniques.

The technique of longitudinal exchange with spin echo recoupling, in particular, provides a means of observing dipolar correlation away from the rotational resonance conditions [21, 22]. In two-dimensional (2D) applications, cross peaks can be observed among coupled spins without undesirable overlap with spinning sideband intensities, while in rotational resonance experiments the spinning sidebands are by definition placed at potential cross peak positions in the 2D plane. In simple cases, the accurate measurement of internuclear distances is also possible. However, the application of two-dimensional MAS experiments to bacteriorhodopsin is quite challenging, particularly when rotor-synchronized multiple pulse mixing is applied, principally because of the poor signal to noise ratio encountered with a sample of high molecular weight. Other experimental difficulties include the need to control and maintain the spinning speed with great precision (i. e. within 5 Hz or less) for long periods of time at low temperature (e. g. –85° C).

II. Retinal-Schiff Base Conformations

In order to demonstrate the feasibility of performing dipolar correlation spectroscopy on proteins in the solid state, two-dimensional RFDR experiments [21] have been performed on ^{13}C-enriched samples of bR [23, 24]. In the first example, relative distances between the retinal-14 position and the ε-^{13}C position of the lys-216 are measured approximately with a single two-dimensional spectrum of dark-adapted (DA) bacteriorhodopsin, which consists of a mixture of the two species bR_{555} and bR_{568} in an approximately 60:40 ratio. The latter is the all-trans retinal species of bR which predominates after irradiation with white light, and it is this light-

adapted (LA) state which undergoes the photocycle. The retinal configurations in these states are shown in Figure (3-1), and a widely accepted basic scheme for the photocycle is illustrated in Figure (3-2) [6], although many of the details are controversial [3-6]. As discussed in Refs. [5] and [6], it appears that there may also be further intermediates, including two M states, and even alternative photocycles. It is generally believed that all of the photointermediates adopt the 13-cis, 15-anti configuration near the Schiff base linkage, while the bR_{568} and bR_{555} states reside in the 13-trans, 15-anti and 13-cis, 15-syn conformations, respectively [3, 13]. The distances in the dark-adapted species, which have already been measured using rotational resonance techniques [11], serve to constrain the retinal conformation at the Schiff base linkage.

In the 2D RFDR spectrum of [14-^{13}C]retinal, [e-^{13}C,^{15}N]lys-bR shown in Figure (3-3) [23], the dipolar cross peaks in the two states are observed simultaneously in a single experiment recorded with a mixing time of 15 ms. The corresponding 1D CPMAS spectrum, also shown in the figure, indicates the positions of the spectral lines corresponding to the labeled spins in [ε-^{13}C]lys-216 at 48 and 53 ppm and in [14-^{13}C]retinal at 110 ppm and 122 ppm in bR_{555} and bR_{568}, respectively [10]. The large resonance at 40 ppm arises from the other six lysine residues, which are also ^{13}C-enriched. The remaining spectral intensity is attributable to the 1.1% natural abundance of ^{13}C nuclei in the protein, retinal, and surrounding lipid. The diagonal in the 2D spectrum (with its rotational sidebands spaced by multiples of the 3.2 kHz rotor frequency), as well as the two pairs of cross peaks corresponding to the selectively enriched sites, are the major features in the two-dimensional spectrum. Cross peaks from dipolar exchange between centerbands and sidebands are also evident owing to the slow spinning rate and the large

shielding anisotropy of the [14-^{13}C]retinal spectral lines. A 2D spectrum of the same sample was also recorded in the absence of mixing pulses, i. e. $\tau_m = 0$ ms, and it differs from the spectrum of Figure (3-3) only in that the cross peaks are absent, aside from signal losses, providing confirmation that the origin of the cross correlation peaks is dipolar exchange.

The intensities of the cross peaks reflect the extent of polarization exchange. The cross peaks associated with bR_{555} have greater intensities than the cross peaks associated with bR_{568}, indicating a stronger dipolar coupling (and therefore a shorter distance) in bR_{555}. Separate numerical calculations are performed for each spin pair in the sample. Dipolar exchange between the two pairs of peaks is not correlated because the conformers are essentially separate dilute spin systems. The simulation results, shown in Figure (3-4), correspond to distances of 3.1 Å (255 Hz) and 3.9 Å (128 Hz) for bR_{555} and bR_{568}, respectively, which are obtained from energy minimization calculations for the syn and anti conformations [11]. The results are scaled to a ratio of 60:40 in order to coincide with the relative equilibrium populations of the two conformers.

For simplicity, δ-function pulses are assumed in the numerical simulations. Following the 15 ms mixing time, the signal losses of the retinal-14 and ε-lysine peaks are approximately 35% in this experiment. As shown in Figure (3-4) for the case of the cross peak above the diagonal, the predicted off-diagonal intensities are 0.17 in bR_{555} and 0.09 in bR_{568} at $\tau_m = 15$ ms, yielding a ratio of 1.9 for the relative intensities. Similar calculations predict almost the same ratio for the opposite side of the 2D spectrum, where polarizations begin at the retinal-14 position. Upon integration of the experimental cross peak areas, a ratio of 1.9 (bR_{555}/bR_{568}) is obtained for magnetizations stemming from the ε-lysine resonances and 1.6

for magnetizations proceeding from the retinal-14 lines. The average experimental ratio of 1.75 is therefore in reasonable agreement with the simulated value of 1.90, in spite of the poor spectral sensitivity.

The absolute measurement of internuclear distances from 2D spectra requires knowledge of the relative changes in both the diagonal and cross peak intensities which occur during mixing. In a system of large molecular weight, only a crude estimate can be made of these intensities because of the ^{13}C background signals which congest the diagonal bands, unless an analogous reference spectrum of an unlabeled sample is also acquired for subtraction under identical conditions. In the experiment discussed here, however, the results reflect the relative internuclear distances surprisingly well, implying that quantitative measurements are possible using two-dimensional MAS experiments on macromolecules.

Sample Preparation. [ε-^{13}C, ^{15}N]Lysine was synthesized according to the procedure of Raap *et. al.* [25] by Prof. J. Lugtenburg and co-workers in Leiden and was incorporated into bacteriorhodopsin of the JW-3 strain of *Halobacterium salinarium* as described previously [26] in the laboratory of Prof. J. Herzfeld. The ^{15}N label was introduced primarily in order to reduce the line-broadening of the ε-lysine resonance line arising from its dipolar coupling to the quadrupolar ^{14}N nucleus [27]. Retinal labeled at the 14 position was also provided by J. Lugtenburg and co-workers. Replacement of the naturally occuring retinal with the labeled species was carried out as outlined in Ref. [23]. A similar procedure was also employed in regenerating the aspartic acid samples discussed below with labeled retinal. After repeated washing with deionized water, the purple membrane sample was centrifuged for 60 min at 30,000 g, and the pellet was packed into a 7 mm sapphire rotor for magic angle spinning.

NMR Experimental Procedure. The NMR spectra were recorded at 79.9 MHz for ^{13}C using the 2D RFDR pulse sequence. The ^{1}H $\pi/2$ pulse length was 4.4 μs, the ^{13}C $\pi/2$ flip up and flip back pulses 5.0 μs, and the π pulses used for mixing were 22 μs in length. The long pulses were used in order to avoid signal losses from interference of the ^{13}C RF pulses with the proton decoupling field, which is relatively weak (only 57 kHz) in this experiment. All samples were spun in an home-built variable-temperature double resonance probe equipped with a 7 mm double bearing MAS assembly (Doty Scientific, Inc., Columbia, SC). The sample temperature was maintained at $-60°$ during the 2D acquisition.

In the acquisition of the 2D spectrum, eighteen t_1 increments were used in the first dimension (F1) with a total spectral window of ± 4.8 kHz, while 1024 time points were recorded during acquisition of the FID in the second dimension (F2) with a spectral window of ± 25.0 kHz. Some aliasing of the carbonyl region and its sidebands occurs in F1 as a consequence of the narrow spectral limits, but these peaks appear in regions where they do not interfere with the resolution of the cross peaks of interest. The construction of the 2D spectrum involves the addition of many 2D spectra acquired with a minimum phase cycling scheme, which consists of a total of 128 scans with permutation of the ^{13}C cross polarization pulse, the flip up and flip back pulses, and phase inversion of the initial ^{1}H pulse combined with receiver alternation [28]. A total of 3840 transients were recorded for each t_1 increment with a 3 sec recycle delay.

In-phase (real) and out-of-phase (imaginary) spectra in the F1 domain were separately recorded according to the "pure phase" method States *et. al.* [29], and subsequently recombined to obtain absorption mode lineshapes across all directions in the 2D plane. Although the absorption mode spectral

lines are narrower than lineshapes with mixed absorption and dispersion mode characters, the absorption mode spectra involve a combination of the "echo" and "anti-echo" components of the 2D spectrum [30]. Unfortunately, even with a rotor-synchronized mixing period, sidebands appear away from the diagonal in the "echo" part of the 2D spectrum [28] even though they cancel in the corresponding "anti-echo" portion of the phase cycle. Since the large off-diagonal sideband manifolds do not arise from dipolar exchange, they are a nuisance which contributes to spectral congestion. At the same time, dipolar exchange between any two members of the sideband manifolds of different spins is never forbidden.

The accumulated FID was treated with a double Fourier transformation which yields a single 2D absorption mode spectrum. The 2D data sets were processed by applying an exponential line-broadening function of 50 Hz prior to the first Fourier tranformation, which was carried out with respect to the t_2 variable. A standard linear prediction algorithm was employed to extrapolate from 18 to 36 points in the t_1 domain, and the slices from the half transform were zero-filled to 1024 points prior to the second Fourier transformation (applied to the t_1 variable). A sample rotation rate of 3.200 kHz, which lies between the $m = 1$ and $m = 2$ rotational resonance conditions for the coupled resonances, was employed in order to maximize the efficiency of polarization transfer [21, 22, 31]. The spinning speed was kept stable within ± 20 Hz in order to enforce the condition of rotor-synchronization to the greatest extent possible.

Simulation Parameters. Because the spinning rate does not greatly exceed the magnitude of the retinal-14 CSA tensor [32], it is included explicitly in the δ-function pulse calculations of dipolar exchange in the two species with estimates of the relative orientations, which are based on known

relationships between the CSA tensors and the molecular reference frames in model compounds [33, 34]. The zero-quantum relaxation process during the periods of free evolution between the pulses is neglected for the resonances in the binding pocket of bR where the ^{13}C spins exist in a rigid environment [35]. In addition, effective transverse relaxation is extremely slow in the polycrystalline model compounds alanine and glycylglycine (as discussed in Chapter 2), implying that it can be neglected for approximate applications with couplings $\geq$ 100 Hz. The loss of longitudinal spin polarizations, however, is incorporated into the calculations, as well as the assumption of similar losses in the zero-quantum coherence between the spins during the pulses.

Figure (3-1). Conformations of the linkage between the Schiff base and the retinal chromophore in the two species of the dark-adapted ground state of bacteriorhodopsin and several photointermediates. In the M state, the Schiff base becomes deprotonated. The atoms which are ^{13}C-labeled are indicated, i. e. the retinal-14 and the ε-lysine sites. In the ground states of bR (bR_{568} and bR_{555}), the Schiff base has a bound proton which is oriented toward to the extracellular side of the channel for proton transport.

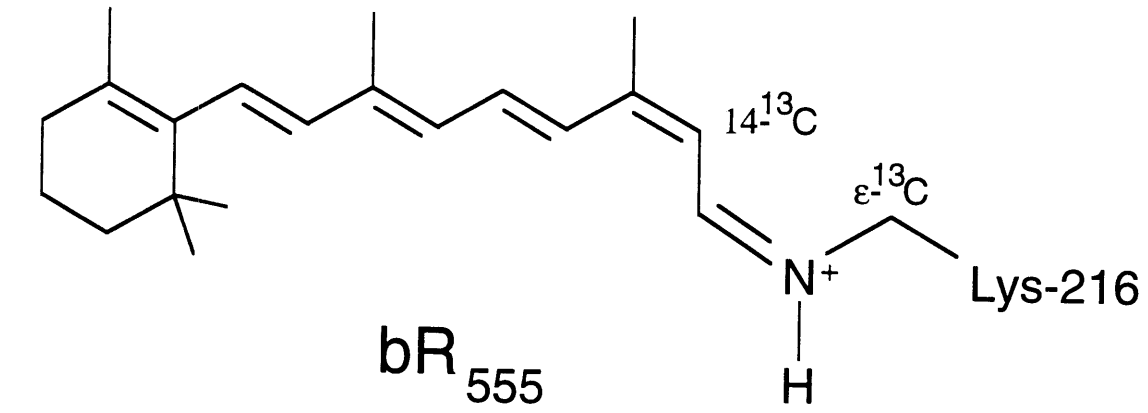

bR_{555}

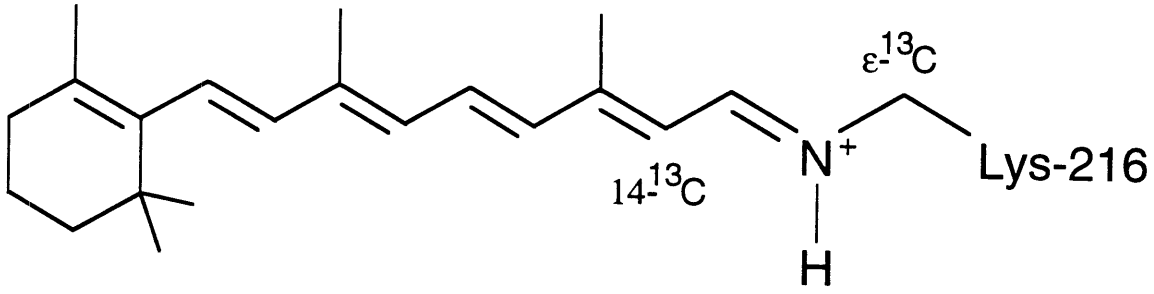

bR_{568}

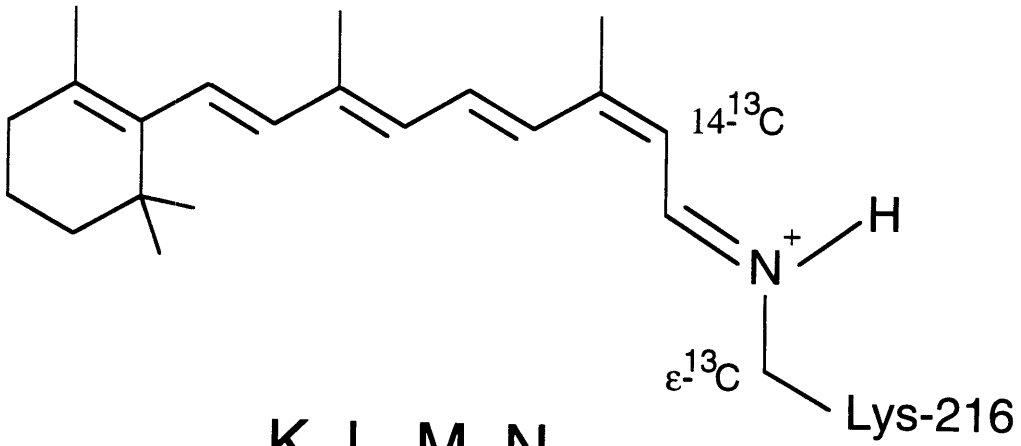

K, L, M, N

Figure (3-2). Simplified version of the bacteriorhodopsin photocycle. The absorption maxima of the various intermediate states of the photocycle are indicated in the prefixes in units of nm. The all-trans state bR_{568} initiates the photocycle upon absorption of a photon, which leads to the K intermediate.

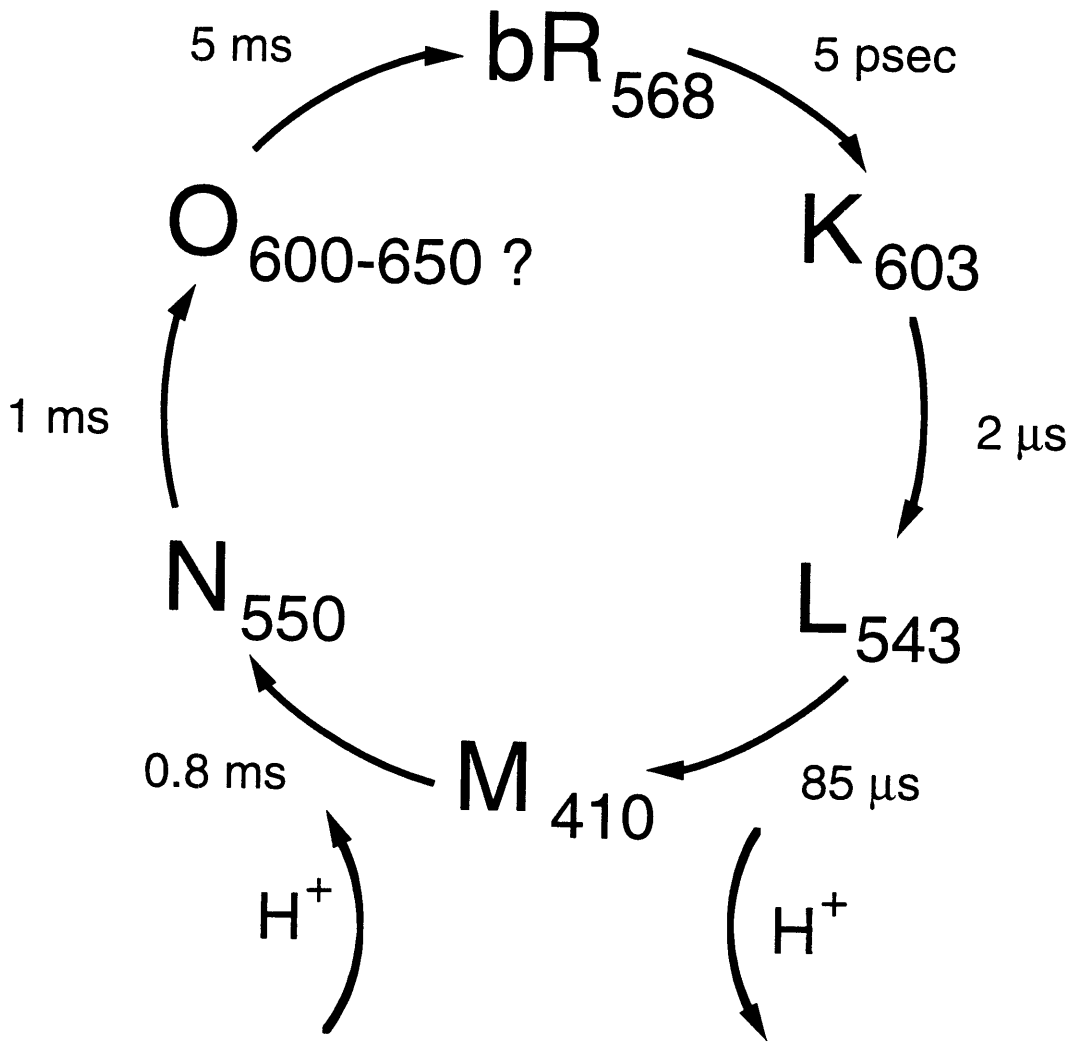
bR568
5 psec
K603
2 µs
L543
85 µs
M410
H+
0.8 ms
N550
1 ms
O600-650 ?
5 ms
H+

Figure (3-3). Two-dimensional RFDR spectrum of dark-adapted [14-^{13}C]retinal, [ε-^{13}C,^{15}N]lys-bacteriorhodopsin with a mixing time of 15 ms. The pairs of dipolar cross peaks are positioned between the sideband manifolds which appear at multiples of the spinning frequency from the diagonal. The spectral intensity along the diagonal includes the signals from the natural abundance ^{13}C nuclei in the sample. Above the spectrum, the corresponding one-dimensional spectrum is shown with the ^{13}C-labeled peaks indicated.

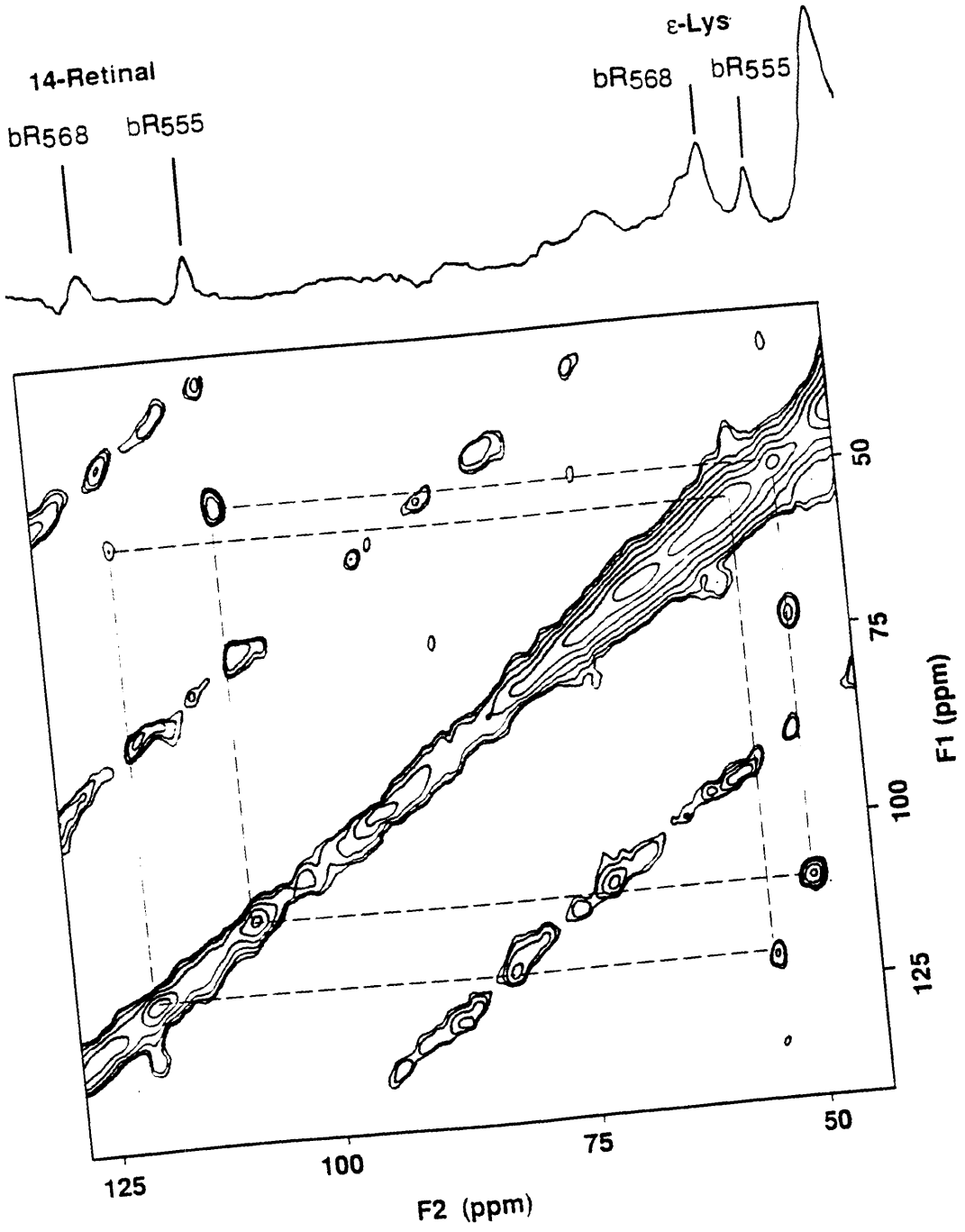
ε-Lys
14-Retinal
bR568
bR555
bR568
bR555
125
100
75
50
F2 (ppm)
50
75
100
125
F1 (ppm)

Figure (3-4). Numerical calculations of dipolar exchange in the two components of dark-adapted bR with δ-function pulses including the influence of the observed 35% loss of the magnetizations. The experimental cross peak ratios compare favorably to the simulation results at 15 ms.

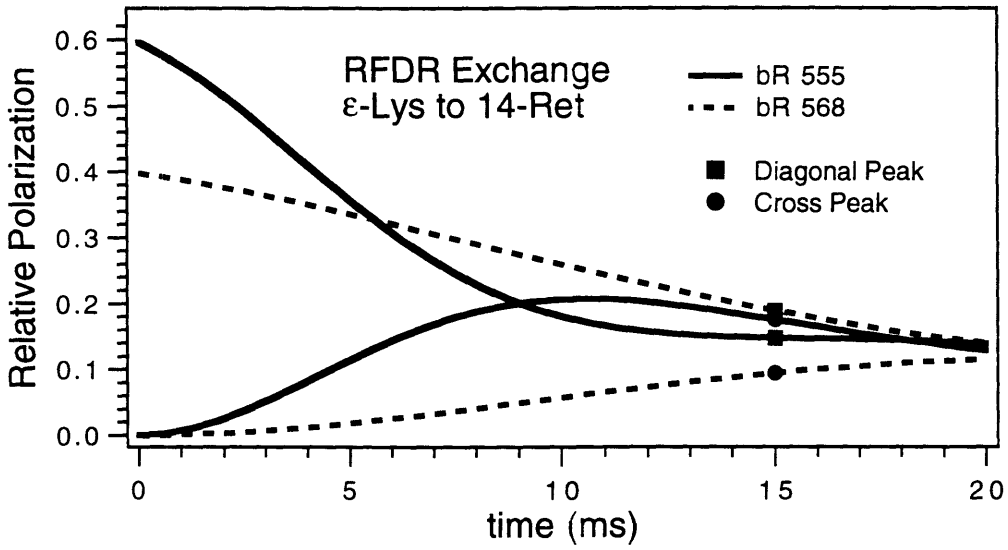
RFDR Exchange
ε-Lys to 14-Ret
bR 555
bR 568
Diagonal Peak
Cross Peak
Relative Polarization
0.0
0.1
0.2
0.3
0.4
0.5
0.6
0
5
10
15
20
time (ms)

III. Aspartic Acid-Retinal Structure

The second bR sample examined here contains a ^{13}C label at the retinal-14 position [10] and enrichment of the [4-^{13}C] positions of the aspartic acid and the [11-^{13}C] positions of the tryptophan residues [18, 35]. The individual [4-^{13}C]aspartic acid resonances which play a role in the binding pocket have been assigned [18, 35]. The asp-96, -85, and -212 residues are directly involved in proton transport [4, 6], and in the bR ground states, the Schiff base proton appears to be solvated by a "complex counterion" consisting of the arg-82, asp-85, and asp-212 residues [36], before its transfer to asp-85 upon Schiff base deprotonation to form the M state [2, 18]. At the same time, however, the asp-212 plays an important role in stabilizing the structure of the retinal binding pocket in bR_{568} [37, 38], and mutants lacking either the aspartic acid-85 or -212 are greatly inhibited in their proton pumping efficiency [4]. In the second half of the photocycle, the Schiff base recovers its proton from the asp-96 sidechain, possibly via water molecules of hydration in the channel [6]. Figure (3-5), adapted from Refs. [2] and [4], illustrates the most important residues in the ion channel and their general relationships within the binding pocket .

In the Henderson model, the separations between the retinal-14 carbon and the [4-C] positions of the asp-212 and asp-85 residues are 4.1 Å and 5.6 Å, respectively [2]. These dipolar couplings are weak (110 Hz and 20 Hz coupling constants), and the second is expected to be too small to observe in practice. However, visible cross peaks are anticipated for correlation to the asp-212. Figure (3-6) shows a CPMAS difference spectrum of the sample enriched in the amino acids prior to the labeling of the retinal peak. In the sample with the ^{13}C-label inserted at the retinal-14 position, a cross peak is

observed in the upper left portion of the 2D RFDR spectrum shown in Figure (3-7), corresponding to the transfer of polarization from the retinal-14 position to the asp-212 site in the light-adapted state of bR. However, in the lower right half, no cross peak is seen above the noise level. Conversion of the whole sample into bR_{568} is carried out prior to acquiring the spectrum in order to increase the intensity of its retinal peak. This all-trans species is in any case the relevant one because it initiates the photocycle. However, in comparable dark-adapted spectra, the same cross peak has been observed in bR_{568} while no correlations have been observed in bR_{555}.

Asymmetries in the cross peak amplitudes in the 2D MAS dipolar exchange spectra are observed frequently, especially in the case of weak homonuclear coupling. In the case of RFDR spectra, one source of genuine asymmetry in the intensities arises from the differences in losses of polarization between the resonances. These losses arise from insufficient proton decoupling during the spin echo sequence. In general, weak dipolar exchange from a resonance whose polarization is decaying rapidly to another spin whose coherences are more long-lived in the multiple pulse sequence leads to larger cross peaks than the reverse process. In the case of doubly-^{13}C-labeled 1,4-^{13}C-$^{15}NH_3$-glycylglycine hydrochloride monohydrate (10% diluted in natural abundance material), similar cross peak asymmetries are observed in 2D RFDR spectra, where the methylene resonance decays much more rapidly under the π pulse sequence than the carbonyl signal. Another possible reason for asymmetric peaks involves discrepancies in the efficiency of cross polarization among different resonances in the bR spectrum. A further source of apparent asymmetry in 2D contour plots are differences between the linewidths of the peaks. Since the resolution in these experiments is reduced in the first time domain by the acquisition of a small

number of time points, and is therefore limited by the acquisition parameters, peaks which are narrower in the second time domain appear taller in the final 2D spectrum.

Because only one of the cross peaks is visible in the 2D RFDR spectrum, a second set of experiments employing dipolar "spin diffusion" induced by heteronuclear couplings to the protons was also performed [39, 40]. These experiments can also be carried out in two-dimensional fashion using a mixing time where the decoupling field applied to eliminate the heteronuclear interactions is removed. The reintroduction of the ^{13}C-^{1}H interactions resolves the frequency mismatch between the ^{13}C resonances, allowing slow magnetization exchange to proceed according to an exponential law in the limit where the ^{13}C-^{1}H and ^{1}H-^{1}H couplings greatly exceed the spinning rate [41]. A basic 2D version of this approach is illustrated in Figure (3-8).

Because the protons participate directly in the exchange process, the rates are difficult to assess quantitatively from first principles. In addition to the extremely slow observed rates of dipolar exchange, this complication in interpreting the results is a disadvantage of the spin diffusion approach compared to RFDR and other multiple pulse methods [42]. However, in the 10% diluted 1,4-^{13}C-$^{15}NH_3$-glycylglycine sample, where the ^{13}C T_1 values are > 10 sec, exchange is 80% complete after 2000 ms mixing with the weak dipole-dipole coupling of 80 Hz (corresponding to a 4.56 Å distance) at 4.800 kHz spinning speed. In spite of the inhomogeneous distribution of crystallites in the powder sample, the glycylglycine spin diffusion trajectory from one dimensional data fits a single exponential decay rate of $\Gamma = 0.78 \pm 0.05$ Hz quite well. According to the theory of Kubo *et. al.* [41], the rates involving protonated carbon resonances are not very sensitive to the spinning speed, and are proportional to the inverse sixth power of the

internuclear distance. Consequently, the glycylglycine result implies that internuclear distances under 5 Å should be readily observable in the bR sample, where the retinal-14 is monoprotonated.

Fortunately, the T_1 values of the [4-^{13}C] resonances of the aspartic acid sidechains in the binding pocket of bR are quite long, i. e. $\geq$ 10 sec [35], so it is feasible to collect spectra with mixing periods of at least $\leq$ 2000 ms and probably much longer. In fact, the sample discussed here exhibits no decay after 2000 ms either in the retinal-14 or in the aspartic sidechain [4-^{13}C] resonances of the binding pocket at low temperature within experimental error. The 2D spin diffusion spectrum shown in Figure (3-9) demonstrates the expected dipolar correlation on both sides of the diagonal in the light-adapted bR sample, confirming the proximity of the asp-212 to the retinal-14 position in bR_{568}.

The asymmetry in cross peak intensities is again observed in this spectrum and in similar ones which have been acquired. Possibly, the peak in the lower right half of the 2D plane is apparently smaller because of line-broadening in the retinal-14 relative to the unprotonated aspartic acid peaks, but this explanation is most likely inadequate. The cross peak intensities under observation are quite small, and they must be extracted from much larger background signals in the 2D Fourier transformation. In addition, the signal to noise ratio is quite low in all of the 2D bR spectra because of limits on how long the MAS experiment can be stably maintained. There is no *a priori* reason to expect the spin diffusion rates to be greater in one direction than in the opposite polarization transfer process. Interestingly, some unexplained asymmetry is also seen in 2D spin diffusion spectra of the doubly-labeled glycylglycine sample, where the signal to noise ratio is much greater.

The two cross peaks exhibit experimental integrated intensities of 0.30 and 0.12 relative to unity for the diagonal retinal intensity, which resides in a region of little spectral overlap with the other resonances. With an estimate of 36% for the population of ^{13}C-labeling in the aspartic acid residues, the maximum relative cross peak intensity is 0.22, so exchange appears to be virtually complete in ≤ 2000 ms. The smaller cross peak implies a spin diffusion rate of $\Gamma = 0.46$ Hz. With the crude assumption that the constants of proportionality are the same for the glycylglycine and the bR samples, this rate implies a distance of 5.0 Å, applying the fact that the spin diffusion rate is proportional to the inverse sixth power of the interatomic separation between the dilute spins. A conservative distance constraint of ≤ 5.5 Å emerges from these results, but it is most likely much shorter, since the larger cross peak implies complete exchange on this time scale. Certainly, these results are consistent with the distance of 4.1 Å given by the Henderson model. In addition, the aspartic acid-85 distance, and likewise those of the other asp residues, to the retinal-14 are ≥ 5.5 Å based on the absence of any observable cross peaks in these experiments and similar ones.

Sample Preparation. The aspartic acid/tryptophan-labeled bR samples were kindly provided by Prof. M. Engelhardt and co-workers, and have been characterized in the literature [43]. The incorporation of the ^{13}C-label into the aspartic acid residues of bR is only about 36% in these samples. The labeled retinal, ^{13}C-enriched to 99% at the 14 position, was provided by Prof. J. Lugtenburg and co-workers. The labeled retinal was again introduced into the protein according to the regeneration procedure outlined in Ref. [23] for the sample used in the RFDR experiment by Drs. J. M. Griffiths and K. V. Lakshmi. Since the bleaching step (i. e. the removal of the natural abundance chromophore from the sample) is not complete, the ^{13}C-labeling is

approximately 90% for the retinal in the regeneration reactions. A second sample was regenerated with the enriched retinal for the spin diffusion experiments by Dr. Griffiths and the author [44], using a protocol similar to one developed by J. Hu [45]. Again the retinal is approximately 90% labeled because of incomplete bleaching, based on UV/visible absorption spectroscopy.

NMR Experiments. The 2D RFDR spectrum in Figure (3-7) was recorded at 6200 ± 10 Hz spinning speed with a mixing period of 31.0 ms, using the rotor-synchronized sequence of one π pulse per rotor period [46] with the compensated *XY*-16 echo sequence [47]. The spectrum was acquired with an home-built high speed MAS probe using a 5 mm sapphire rotor from Doty Scientific. The translucent rotor was irradiated for 1 hour at $0 \pm 5°$C with a 500 W projector lamp and quickly transfered to the cooled probe in order to convert the whole bR sample into its light-adapted state (bR_{568}). The pulse lengths were 2.6 μs for the ^{1}H $\pi/2$ pulse (and the corresponding decoupling field of 96 kHz), 6.0 μs for the ^{13}C $\pi/2$ cross polarization and flip pulses, and 14.2 μs for the π pulses during mixing. A total of 512 scans were collected for both the real and imaginary parts at each t_1 point, and the temperature was held constant at $-38°$C during acquisition.

The spin diffusion spectrum was acquired at 4900 ± 30 Hz with a 2000 ms mixing period where decoupling was not applied. Precise control of the spinning frequency is not essential to obtain dipolar exchange using this approach. Here, a 7 mm sapphire rotor and stator assembly from Doty was employed, and as in the RFDR experiment, the sample was light-adapted prior to acquisition. The number of scans was 384 scans per t_1 point. The temperature was maintained at $-90 \pm 5°$C during acquisition. Here the ^{1}H $\pi/2$ pulse was only 3.8 μs, and accordingly the decoupling field was 73.5 kHz.

In both the RFDR and spin diffusion spectra, 24 t_1 points were acquired with a dwell time of 125 μs. A 2 sec recycle delay was employed in these experiments between consecutive scans. The phase cycling and data acquisition parameters were otherwise similar to the ε-lys experiment discussed earlier. The spin diffusion spectrum was processed by extending the FID in the first time domain to 64 points with a standard linear prediction routine incorporated into the RNMR program of Dr. D. Ruben after adding 40 Hz of exponential line-broadening. The same 40 Hz was also applied in the second time domain, where 1024 points was acquired with a 20 μs dwell time. The first dimension were then zero-filled to 1024 points prior to the second Fourier transformation.

The 1D CPMAS spectrum of the aspartic acid labeled material in Figure (3-6), provided by Drs. Janet Griffiths and K. V. Lakshmi, is a difference spectrum between the [4-^{13}C]aspartic acid enriched material and an otherwise similarly prepared sample (also provided by Prof. Engelhard and co-workers). This spectrum was acquired at 100 MHz for ^{13}C, providing somewhat better resolution than is usually obtained at 79.9 MHz, where the 2D experiments were performed.

Figure (3-5). Schematic diagram of the proton transport channel in bacteriorhodopsin, illustrating the retinal, the key aspartic acid residues, and the arginine-82. Asp-96 is thought to be the proton donor to the Schiff base in the second half of the photocycle, while asp-85 is the proton acceptor upon Schiff deprotonation to form M in the first portion.

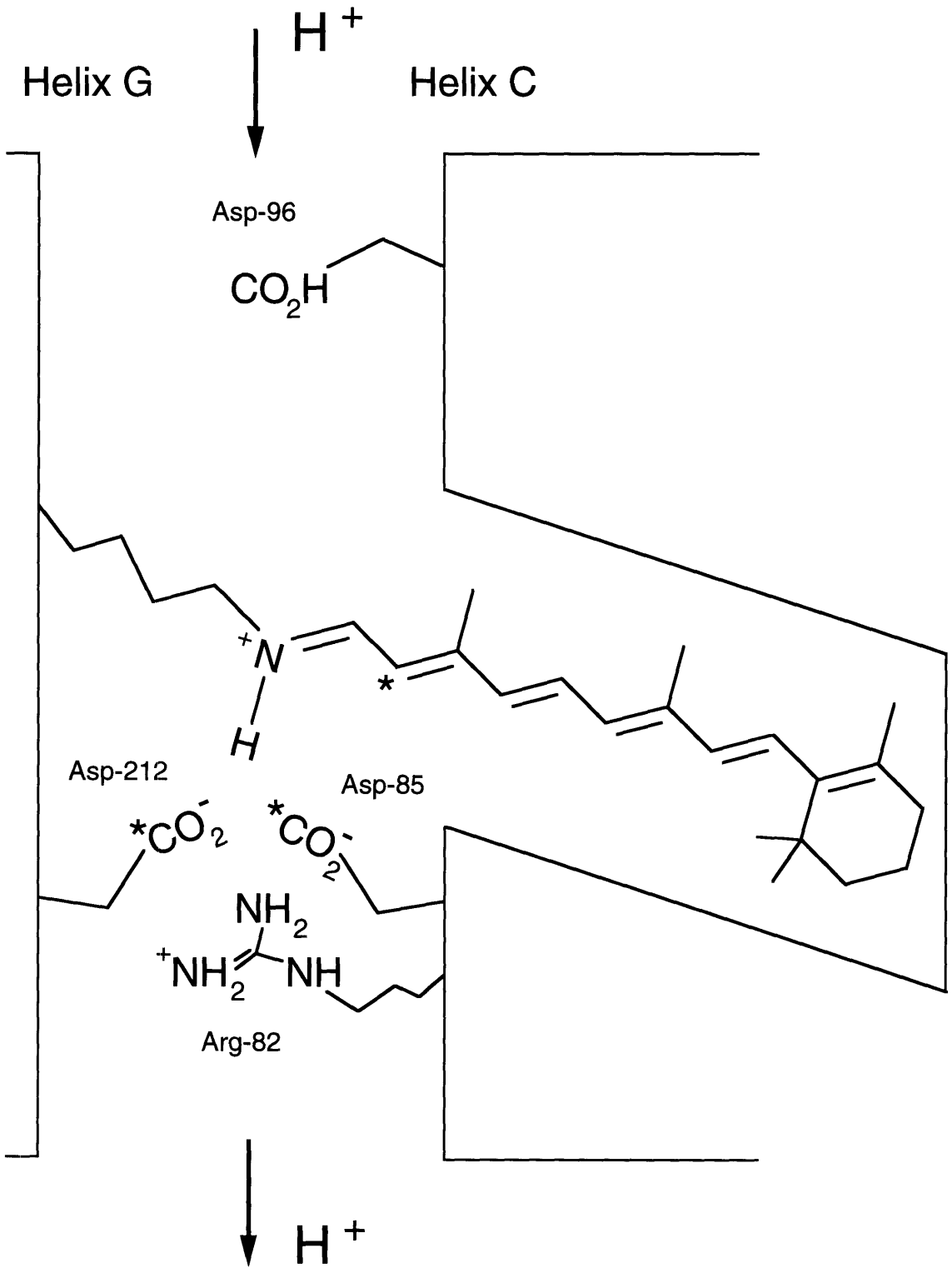
H +
Helix G
Helix C
Asp-96
CO2H
+N
H
*
Asp-212
Asp-85
*CO2-
*CO2-
NH2
+NH2
NH
Arg-82
H +

Figure (3-6). One-dimensional CPMAS difference spectrum of the aspartic acid/tryptophan ^{13}C-enriched sample of dark-adapted bacteriorhodopsin at 100 MHz for ^{13}C.

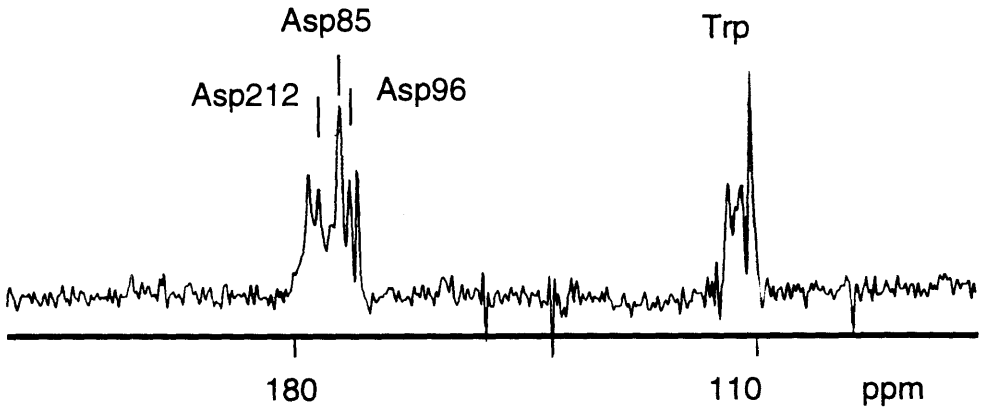
Asp85
Trp
Asp212
Asp96
180
110
ppm

Figure (3-7). Two-dimensional RFDR spectrum of light-adapted [4-^{13}C]asp, [14-^{13}C]retinal-bacteriorhodopsin at 6.200 kHz with a 31 ms mixing period. A dipolar cross peak corresponding to exchange from the retinal-14 to the asp-212 residue is observed in the spectrum. The reverse process is not visible in the opposite side of the 2D plane because of the low signal to noise ratio and the frequently observed asymmetries in the cross peak intensities, which have been seen in other similar 2D experiments.

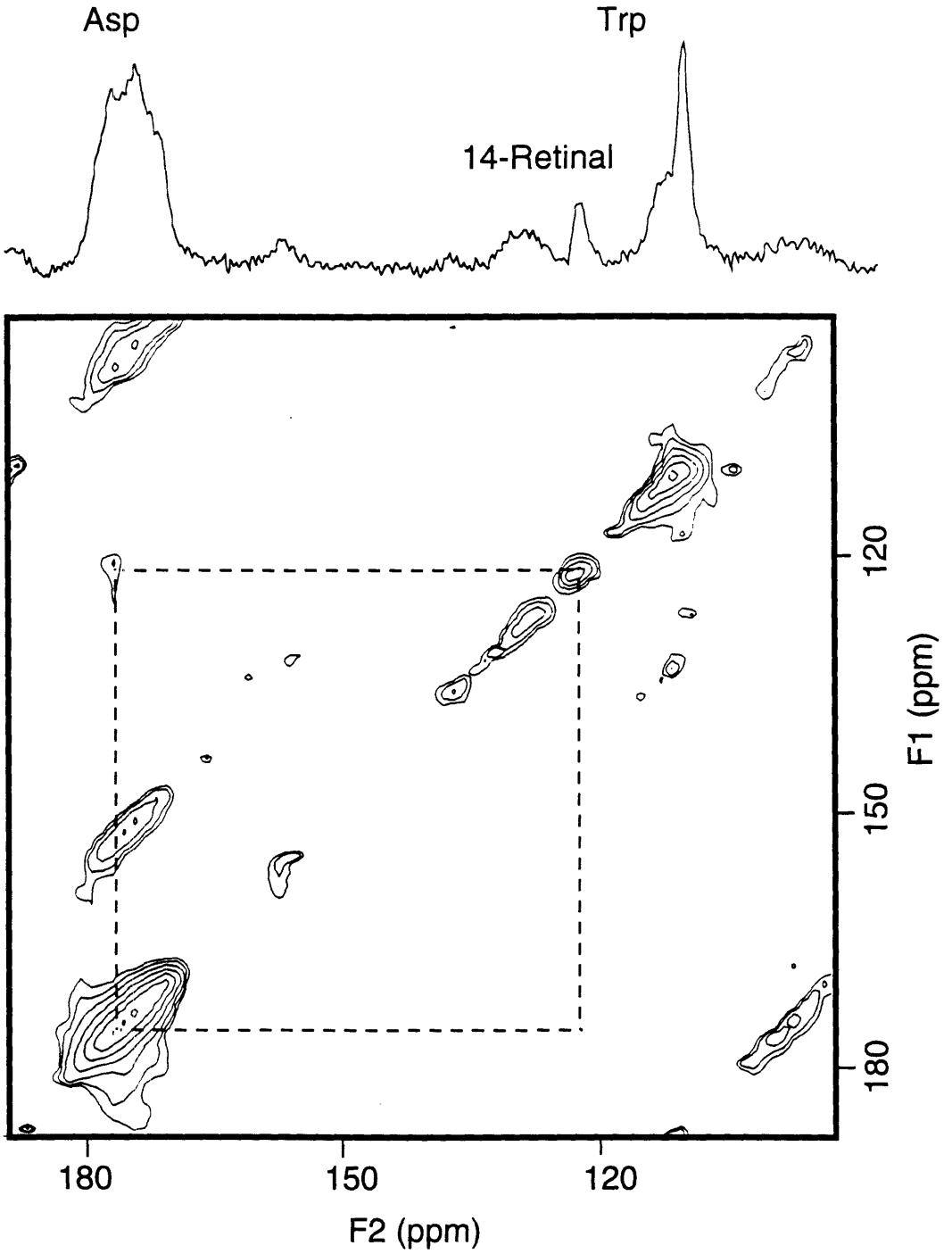
Asp
Trp
14-Retinal
120
150
180
F1 (ppm)
180
150
120
F2 (ppm)

Figure (3-8). Pulse sequence for 2D dipolar exchange with spin diffusion generated by coupling to protons. Slow exchange is stimulated over a broad range of chemical shift differences between the spins by removal of the proton decoupling field during the mixing time in the 2D longitudinal exchange experiment.

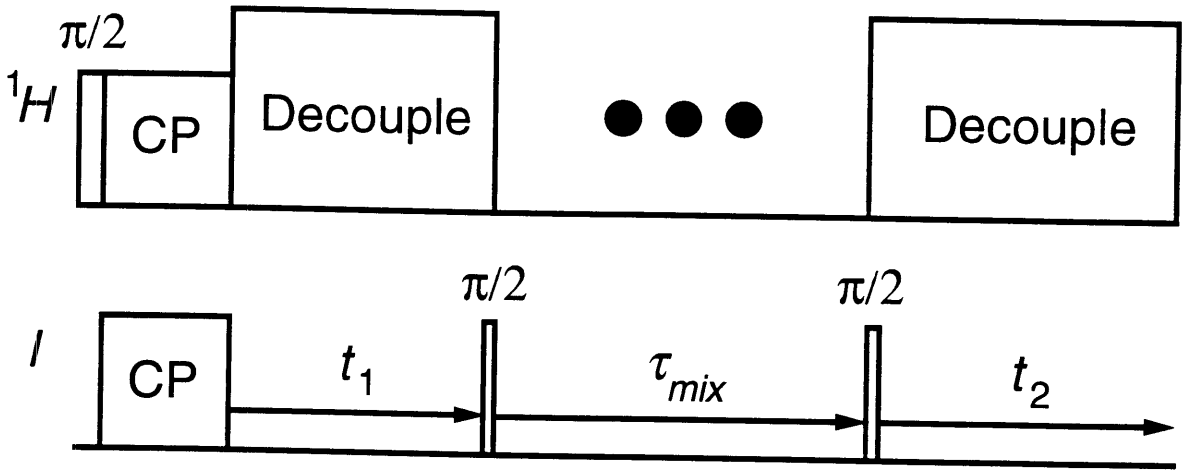
π/2
^1H
CP
Decouple
Decouple
π/2
π/2
I
CP
t_1
τ_{mix}
t_2

Figure (3-9). Two-dimensional spin diffusion spectrum of light-adapted [4-^{13}C]asp, [14-^{13}C]retinal-bacteriorhodopsin at 4.900 kHz with a 2000 ms mixing period. Dipolar cross peaks are observed between the asp-212 and the retinal-14 position, which are both ^{13}C-enriched. However, although the dipolar exchange process is symmetric in principle, the cross peak above the diagonal is much larger in the processed 2D spectrum. Similar RFDR and spin diffusion spectra of the doubly-labeled glycylglycine sample also exhibit some cross peak asymmetry.

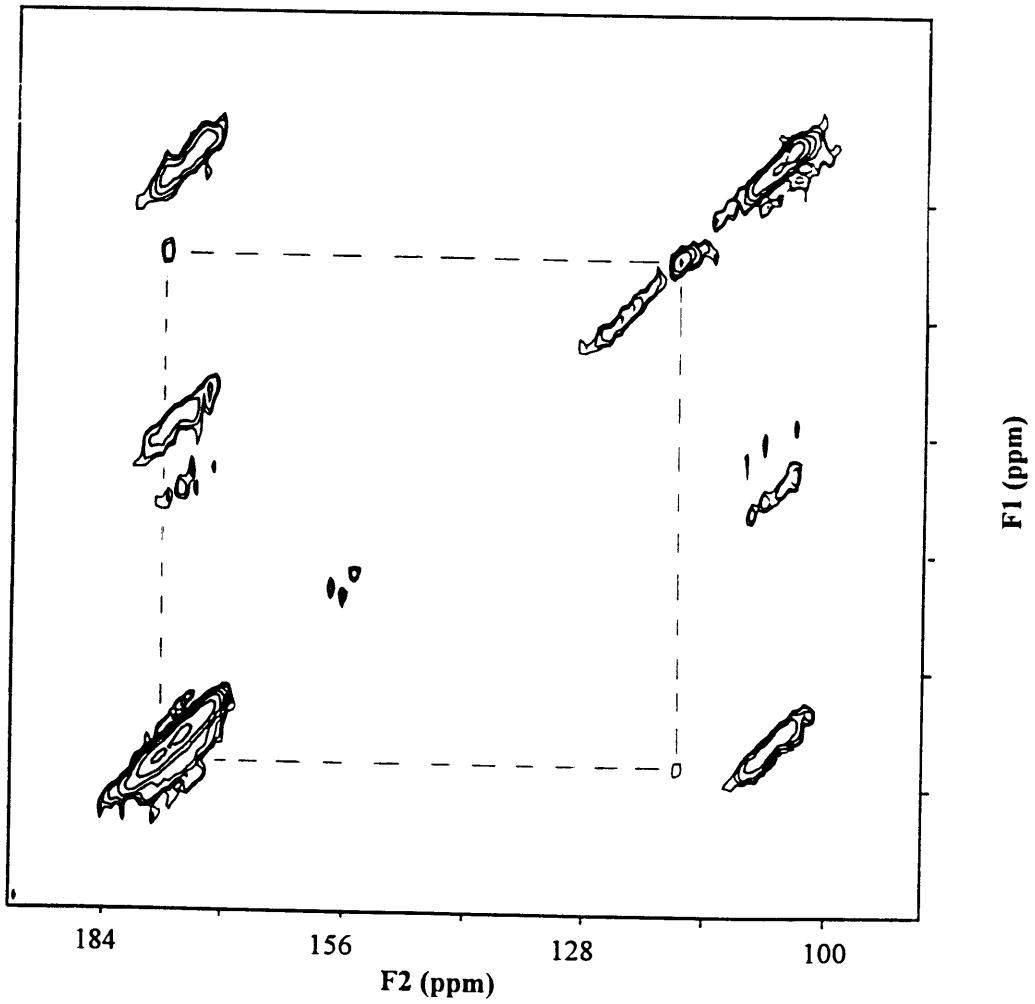
184
156
128
100
F2 (ppm)
F1 (ppm)

IV. Conclusion

With current technical constraints, it is challenging to acquire two-dimensional spectra of samples with large molecular weights, since these exhibit a low signal to noise ratio and extensive spectral overlap in solid state NMR experiments. However, the results shown here for a 26 kD sample demonstrate the promise of these methods for approximate distance measurements in large proteins in the solid state. Because solid state NMR methods do not require crystalline samples or soluble molecules possessing a short correlation time for tumbling in solution [48, 49], they are complimentary to the methods of solution NMR and X-ray crystallography. Improvements in the spectral sensitivity and the stability of MAS equipment at low temperatures will enhance the prospects for studying large isotopically enriched proteins which exhibit some chemical shift resolution among the resonances of interest.

Based on the spin diffusion experiment, where the sensitivity is sufficiently high to estimate cross peak intensities in the aspartic acid sample, a constraint of ≤ 5.5 Å has been established for the retinal-14 to aspartic acid-212 distance. None of the other aspartic acid or tryptophan residues exhibits observable cross peaks in either the RFDR or spin diffusion spectra, in agreement with the Henderson model [2], for which all of the corresponding distances are greater than 5.5 Å. Likewise, the same asp-212 correlation is not observed in bR_{555}, indicating that the corresponding distance is greater than 5.5 Å.

Similar efforts to characterize these structural constraints in the M intermediate of the bR photocycle have also been in progress. In these experiments, the deprotonated Schiff base state is trapped in guanidine

hydrochloride under basic conditions by irradiation with yellow light at low temperature [10]. These experiments have the potential to contribute important information about how the retinal binding pocket changes upon formation of the trapped M intermediate, which plays a critical role in the bR photocycle [3, 5, 6].

References for Chapter 3.

[1] D. Osterhelt and W. Stoeckenius, Proc. Nat. Acad. Sci. U. S. A. **70**, 2853 (1973).

[2] R. Henderson, J. M. Baldwin, T. A. Ceska, F. Zemlin, E. Beckmann, and K. H. Downing, J. Mol. Bio. **213**, 899 (1990).

[3] R. A. Mathies, S. W. Lin, J. B. Ames, and W. T. Pollard, Annu. Rev. Biophys. Biophys. Chem. **20**, 491 (1991).

[4] H. G. Khorana, Proc. Natl. Acad. Sci. USA **90**, 1166 (1993).

[5] J. K. Lanyi, J. Bioenerg. Biomem. **24**, 169 (1992).

[6] T. Ebrey, in *Light Energy Transduction in Bacteriorhodopsin*, M. B. Jackson, ed. (CRC Press, Boca Raton, 1993).

[7] L. Zheng and J. Herzfeld, J. Bioenerg. Biomem. **24**, 139 (1992).

[8] G. S. Harbison, S. O. Smith, J. A. Pardoen, P. P. J. Mulder, J. Lugtenburg, J. Herzfeld, R. A. Mathies, and R. G. Griffin, Proc. Natl. Acad. Sci. U. S. A. **81**, 1706 (1984).

[9] F. Creuzet, A. McDermott, R. Gebhard, K. van der Hoef, M. B. Spijker-Assink, J. Herzfeld, J. Lugtenburg, M. H. Levitt, and R. G. Griffin, Science **251**, 783 (1991).

[10] M. R. Farrar, K. V. Lakshmi, S. O. Smith, R. S. Brown, J. Raap, J. Lugtenburg, R. G. Griffin, and J. Herzfeld, Biophys. J. **65**, 310 (1993).

[11] L. K. Thompson, A. E. McDermott, J. Raap, C. M. van der Wielen, J. Lugtenburg, J. Herzfeld, and R. G. Griffin, Biochem. **31**, 7931 (1992).

[12] S. O. Smith, J. Courtin, E. van den Berg, C. Winkel, J. Lugtenburg, J. Herzfeld, and R. G. Griffin, Biochem. **28**, 237 (1989).

[13] K. V. Lakshmi, M. Auger, J. Raap, J. Lugtenburg, R. G. Griffin, and J. Herzfeld, J. Am. Chem. Soc. **115**, 8515 (1993).

[14] M. S. Braiman, T. Mogi, T. Marti, L. J. Stern, H. G. Khorana, and K. J. Rothschild, Biochem. **27**, 8516 (1988).

[15] M. S. Braiman, O. Bousche, and K. J. Rothschild, Proc. Nat. Acad. Sci. U. S. A. **88**, 2388 (1991).

[16] S. O. Smith, J. Lugtenburg, and R. A. Mathies, J. Membr. Bio. **85**, 95 (1985).

[17] J. B. Ames, S. R. Bolten, M. M. Netto, and R. A. Mathies, J. Am. Chem. Soc. **112**, 9007 (1990).

[18] G. Metz, F. Siebert, and M. Engelhard, FEBS Lett. **303**, 237 (1992).

[19] D. P. Raleigh, M. H. Levitt, and R. G. Griffin, Chem. Phys. Lett. **146**, 71 (1988).

[20] M. H. Levitt, D. P. Raleigh, F. Creuzet, and R. G. Griffin, J. Chem. Phys. **92**, 6347 (1990).

[21] A. E. Bennett, J. H. Ok, R. G. Griffin, and S. Vega, J. Chem. Phys. **96**, 8624 (1992).

[22] D. K. Sodickson, M. H. Levitt, S. Vega, and R. G. Griffin, J. Chem. Phys. **98**, 6742 (1993).

[23] J. M. Griffiths, K. V. Lakshmi, A. E. Bennett, J. Raap, C. M. van der Wielen, J. Lugtenburg, J. Herzfeld, and R. G. Griffin, J. Am. Chem. Soc. **116**, 10178 (1994).

[24] J. M. Griffiths, A. E. Bennett, K. V. Lakshmi, J. Raap, J. Lugtenburg, M. Engelhard, J. Herzfeld, and R. G. Griffin, poster presentation at the 36th Experimental NMR Conference, March 1995, Boston, MA.

[25] J. Raap, C. M. van der Wielen, and J. Lugtenburg, Recl. Trav. Chim. Pays-Bas **109**, 277 (1990).

[26] P. V. Argade, K. J. Rothschild, A. H. Kawamoto, J. Herzfeld, and W. C. Herlihy, Proc. Natl. Acad. Sci. USA **78**, 1643 (1981).

[27] R. K. Harris and A. C. Olivieri, Prog. NMR Spectroscopy **24**, 435 (1992).

[28] A. P. M. Kentgens, E. deBoer, and W. S. Veeman, J. Chem. Phys. **87**, 6859 (1987).

[29] D. J. States, R. A. Haberkorn, and D. J. Ruben, J. Mag. Res. **48**, 286 (1982).

[30] R. R. Ernst, G. Bodenhausen and A. Wokaun, *Principles of Nuclear Magnetic Resonance in One and Two Dimensions* (Clarendon Press, Oxford, 1987).

[31] T. Gullion and S. Vega, Chem. Phys. Lett. **194**, 423 (1992).

[32] S. O. Smith, H. J. M. de Groot, R. Gebhard, J. M. L. Courtin, J. Lugtenburg, J. Herzfeld, and R. G. Griffin, Biochem. **28**, 8897 (1989).

[33] W. S. Veeman, Prog. NMR Spectroscopy **16**, 193 (1984).

[34] E. K. Wolff, R. G. Griffin, and J. S. Waugh, J. Chem. Phys. **67**, 2387 (1977).

[35] G. Metz, F. Siebert, and M. Engelhard, Biochem. **31**, 455 (1992).

[36] H. J. M. deGroot, G. S. Harbison, J. Herzfeld, and R. G. Griffin, Biochem. **28**, 3346 (1989).

[37] T. Mogi, L. J. Stern, T. Marti, B. H. Chao, and H. G. Khorana, Proc. Natl. Acad. Sci. USA **85**, 4148 (1988).

[38] H. Otto, T. Marti, M. Holz, T. Mogi, L. J. Stern, F. Engel, H. G. Khorana, and M. P. Heyn, Proc. Natl. Acad. Sci. USA **87**, 1018 (1990).

[39] D. Suter and R. R. Ernst, Phys. Rev. B **32**, 5608 (1985).

[40] D. L. Vanderhart, J. Mag. Res. **72**, 13 (1987).

[41] A. Kubo and C. A. McDowell, J. Chem. Soc. Faraday Trans. **84**, 3713 (1988).

[42] A. E. Bennett, R. G. Griffin, and S. Vega, NMR Basic Principles and Progress **33**, 1 (1995).

[43] M. Engelhard, B. Hess, D. Emeis, G. Metz, W. Kreutz, and F. Siebert, Biochem. **28**, 3967 (1989).

[44] J. M. Griffiths and A. E. Bennett, unpublished work (1995).

[45] J. Hu, unpublished work (1994).

[46] E. T. Olejniczak, S. Vega, and R. G. Griffin, J. Chem. Phys. **81**, 4804 (1984).

[47] T. Gullion, D. B. Baker, and M. S. Conradi, J. Magn. Res. **89**, 479 (1990).

[48] K. Wüthrich, *NMR of Proteins and Nucleic Acids* (John Wiley and Sons, New York, 1986).

[49] G. M. Clore and A. M. Gronenborn, Annu. Rev. Biophys. Chem. **21**, 29 (1991).

Chapter 4.

Performance of Spin Echo Sequences in Double Resonance Experiments

I. Introduction

The refocusing of spin evolution under the Zeeman-like terms in the spin Hamiltonian, such as the chemical shifts, is a common technique in NMR spectroscopy [1]. The formation of a Hahn echo is achieved through the application of π pulses which reverse the sense of rotation under inhomogeneous interactions. Rotor-synchronized π pulse sequences can be applied to achieve joint spin and rotational echoes [2, 3] in spinning samples, generalizing the Hahn echo to MAS experiments. For example, the simple sequence of one π pulse per rotor period leads to complete refocusing of the signal following every two rotor cycles [2]. Trains of π pulses are also applied frequently in solution experiments, such as measurements of diffusion constants [1], and in MAS recoupling experiments [4]. When the signal is observed after many pulses (i. e. ≥ 100), the degradation, or spurious rotation of the signal in the transverse plane, becomes a serious problem. Accordingly, several methods have been introduced to compensate for rotation errors in the π pulses. An early approach, the Carr Purcell Meiboom Gill echo train [1], consists of a train of X pulses applied to initially prepared Y magnetization. This scheme is particularly useful for reducing the problem of RF inhomogeneity.

For more general applications, the XY-4 scheme was introduced to compensate simultaneously for pulse imperfections in the refocusing of all components of the spin magnetization [5]. Expansions of the basic cycle [6] have been applied to solution experiments [7] and several MAS applications [8-11]. Another four pulse cycle for compensating pulse errors is the "MLEV-4" cycle [12], which is based on the general scheme $XX\overline{X}\overline{X}$ for a supercycle consisting of net π pulse rotations [13]. The relative performance of the two

expansion schemes of simple π pulses has been compared in solution experiments [6] and with Floquet Theory for MAS applications [14]. Here, a general approach to the analysis of compensated π pulse sequences is applied to the comparison of these three basic approaches. The net rotation error obtained with *XYXY* and $XX\overline{XX}$ is strikingly similar in the most general case, although in the windowless limit the latter is more favorable for large resonance offsets and RF inhomogeneity.

In addition to compensation for pulse errors experienced by a single isolated spin, a major difficulty encountered in solid state double resonance experiments is the interference between the proton decoupling field and pulse sequences which are applied to dilute spins under observation [15]. In general, rapid signal losses are observed unless the RF fields are greatly mismatched in amplitude. Here, the problem of insufficient proton decoupling is discussed within the framework of a simple model, and it is shown that a mismatch in the RF field strengths by a factor of approximately three is necessary for the case of π pulses. Because the depolarization effect tends to increase with the length of the pulse, composite pulse rotations [16, 17] are generally undesirable in double resonance MAS applications, where sample spinning and ^{1}H-^{1}H couplings contribute additional complications. Consequently, a more favorable solution is to apply phase alternation schemes like the ones analyzed here.

II. Theory of Compensated Pulse Sequences

Figure (4-1) illustrates three schemes of phase alternation which are used in multiple pulse spin echo experiments [6]. The Carr Purcell Meiboom Gill sequence is often employed in the formation of spin echoes of the

transverse magnetization, and it provides a means of measuring the homogeneous portion of magnetization decay [1]. The others are approaches which are more generally tolerant to a variety of pulse errors, including resonance offsets, RF inhomogeneity, and phase transients. The principal difficulty in analyzing these sequences is that the cycle time τ_C is often long relative to the inverse of the spin interactions, and as a consequence, it is inappropriate to apply the AHT approximation directly to the case of long windows between the pulses.

The case of long windows, however, is the most relevant one for rotor-synchronized MAS experiments on dilute spins. In the limit of short windows, the performance of these sequences has been investigated with Floquet Theory [14]. An approximate theory which is more generally applicable is introduced here in order to evaluate the performance of the compensated echo sequences. In MAS recoupling experiments, the largest errors in applying multiple pulse sequences arise from the resonance offsets and the RF inhomogeneity. Neither can be eliminated in most cases. With several spins at different frequencies, it is impossible to place the RF field at exact resonance with all of them simultaneously. Moreover, the resonance offset is oscillating through a range of values in MAS experiments. The RF field amplitude in the sample coil is typically within its nominal strength by $\pm 5\%$, or $\pm 10\%$ at most, in typical CPMAS applications. The treatment presented here applies to the case of sample spinning under two conditions: the first is that $\tau_R >> \tau_p$, so that the resonance offset $\delta(t)$ is essentially time-independent during the brief pulse interval τ_p, and the second is that the pulses are applied only at points in time where the offset recurs repeatedly to the same value. The class of echo sequences where the π pulses are applied every N rotor periods possesses this property. The sequences analyzed here

cannot compensate for pulse errors which change from the application of one pulse to the next.

Including these effects, the Hamiltonian for a single spin has the form:

$$\begin{aligned} H &= H_0 + H_1 \\ &= \nu_{RF} S_x + \{\delta S_z + \Delta\nu_{RF} S_x\}, \end{aligned} \tag{4-1}$$

during the application of an X pulse, but just $H = \delta S_z$ during free evolution between the pulses, where δ represents the deviation of the spin frequency from resonance with the RF transmitter and ν_{RF} is the RF field strength. The $\Delta\nu_{RF}$ term represents the deviation in the RF field from its nominal value. Although AHT cannot be applied for the entire cycle time τ_C, it is valid for small pulse errors during the pulse time τ_p when $\nu_{RF} >> \delta,\ \Delta\nu_{RF}$. Through orders $\tilde{H}_D^{(0)}$ and $\tilde{H}_D^{(1)}$, the time evolution operator for the X pulse can be conveniently approximated to $O(\text{error}^2)$:

$$\begin{aligned} U_X(\tau_p,0) &\approx \exp\{-i2\pi\,\nu_{RF}\tau_p S_x\}\exp\left\{-i\left(\tilde{H}_1^{(0)} + \tilde{H}_1^{(1)}\right)\tau_p\right\} \\ &= \exp\{-i\pi S_x\}\exp\left\{-i\left[\left(2\pi\Delta\nu_{RF} - \pi\frac{\delta^2}{\nu_{RF}}\right)\tau_p S_x - 4\delta\left(1+\frac{\Delta\nu_{RF}}{\nu_{RF}}\right)\tau_p S_y\right]\right\}. \end{aligned} \tag{4-2}$$

With the definition of a time evolution operator for the phase accumulated during half of the window period:

$$U_\delta\left(\tfrac{1}{2}(\tau_w - \tau_p), 0\right) = \exp\left\{-i2\pi\delta\tfrac{1}{2}(\tau_w - \tau_p)S_z\right\}, \tag{4-3}$$

the evolution operator for the entire *XYXY* sequence can be written, omitting most of the time arguments for convenience, as follows:

$$U(\tau_C,0)=\{U_\delta U_Y U_\delta\}\{U_\delta U_X U_\delta\}\{U_\delta U_Y U_\delta\}\{U_\delta U_X U_\delta\}. \tag{4-4}$$

With aid of the two identities [1]:

$$\begin{aligned} U\exp\{-iA\}U^{-1}&=\exp\{-iUAU^{-1}\};\\ U\exp\{-iA\}U^{-1}&=\exp\{-iUAU^{-1}\}U, \end{aligned} \tag{4-5}$$

which are always valid for unitary operators U, all terms are collected into small rotations and recombined through lowest order in the Baker Campbell Hausdorff expansion [18].

In terms of the phase ψ which is accumulated between the pulses, $\psi=2\pi\delta(\tau_w-\tau_p)$, and with the convenient definitions:

$$a=\frac{2\delta}{\nu_{RF}}\left\{1+\frac{\Delta\nu_{RF}}{\nu_{RF}}\right\};\ b=\pi\left\{-\frac{\delta^2}{2\nu_{RF}^2}+\frac{\Delta\nu_{RF}}{\nu_{RF}}\right\}, \tag{4-6}$$

the rotation error through lowest order following the *XYXY* cycle reduces to the form:

$$U(\tau_C,0)=\exp\{+i[(b^2-a^2)\cos\psi-2ab\sin\psi]S_z\}. \tag{4-7}$$

The condition $U(\tau_C,0)=\pm 1$ holds for an ideal echo sequence, where no apparent spin evolution occurs over the cycle. Since ψ can assume any value for long windows, the resonance offset effect most generally enters in second

order $O(\delta^2 / \nu_{RF}^2)$ as a rotation about the z axis, although the performance is compensated to $O(\delta^3 / \nu_{RF}^3)$ when $\psi = (2n+1)\pi/2$. In other words, the compensation in $XYXY$ benefits from the phase evolution during the windows. Since the rotation error is oriented along the z axis, the performance of the sequence is much worse for transverse magnetization than for recovery of longitudinal magnetization.

A similar derivation can be performed for the cycle $XX\overline{XX}$, leading to the analogous expression:

$$U(\tau_C, 0) = \exp\left\{+i\left[(a^2 - b^2)\sin\psi - 2ab\cos\psi\right]S_z\right\}. \qquad (4\text{-}8)$$

Interestingly, the order of compensation is almost identical for arbitrary ψ, although the performances of $XYXY$ and $XX\overline{XX}$ differ substantially for a given ψ. However, in the windowless limit $\psi \to 0$, the $XX\overline{XX}$ cycle is clearly superior because the residual error from the offset, for instance, is $O(\delta^3 / \nu_{RF}^3)$. Therefore, for windowless applications in the presence of large inhomogeneous local fields, such as heteronuclear spin decoupling, the MLEV-4 cycle [13] is clearly the better framework for the expansion of compensated sequences. On the other hand, the $XYXY$ is advantageous over $XX\overline{XX}$ for the problem of amplitude imbalance [19], where the RF field strength deviates slightly when applied with different phase settings. However, this error is quite small for an optimized RF transmitter ($\leq 0.1\%$), and in any case random fluctuations of this nature cannot be refocused effectively via phase alternation. In practice, the two basic cycles exhibit similar performance in MAS applications. In REDOR experiments [20], for example, XY-8 and MLEV-8 yield comparable signal losses and dephasing curves [21], at least for heteronuclear dipole-dipole couplings ≥ 200 Hz. For

the RF inhomogeneity, the resonance offset, and pulse errors of similar symmetry, the analytic expressions derived here imply very similar performance. Other cycles can also be examined with this approach, but it is interesting to note that only the two examined here yield the same degree of compensation. There appears to be no other four pulse cycle with the property of general tolerance to imperfections in pulse rotations.

The same analysis applied to *XXXX*, the basic Carr Purcell sequence, leads to the expression:

$$U(\tau_C,0) = \exp\left\{i\left(\left[4b\cos\psi/2 - 4a\sin\psi/2\right]S_x + \left[(a^2-b^2)\sin\psi - 2ab\cos\psi\right]S_z\right)\right\}. \tag{4-9}$$

Because there is a large first order error along x, the best performance is obtained when the sequence is applied with the initial condition of transverse magnetization along X, with which it commutes. This approach is the Meiboom Gill modification to the Carr Purcell sequence for multiple echoes. The second term is identical through lowest order to that of $XX\overline{XX}$.

In order to obtain terms of cubic and higher orders in the rotation error, the AHT treatment of the imperfections during the pulses must be calculated through higher order – or alternatively the error can be derived with exact analytic calculations. The recombination of small rotation operators must also be pursued through higher orders. With the assumption of convergence, this framework enables the calculation of the net error through higher order terms in the Baker Campbell Hausdorff expansion [18]:

$$\exp\{A\}\exp\{B\} = \exp\left\{(A+B)+\tfrac{1}{2}[A,B]+\tfrac{1}{12}([A,[A,B]]+[[A,B],B])+\ldots\right\}. \tag{4-10}$$

It is useful to understand the higher orders in order to expand the sequences. For example, the extension of the basic sequences to eight pulses [6, 12], $XYXY \rightarrow XYXY\ YXYX$ and $XX\overline{XX} \rightarrow XX\overline{XX}\ X\overline{XX}X$, cancels the lowest order term along z, but leaves a smaller rotation error about an axis within the transverse plane. This deviation is in turn eliminated by expansions to sixteen pulse cycles via inversion of all phases.

Figure (4-1). Three compensated pulse sequences for multiple pulse echo formation: the Carr Purcell (*XXXX*), *XY*-4 (*XYXY*), and MLEV-4 ($\overline{XXXX}$) schemes of phase alternation. The notation $X(\pi)$ indicates a pulse of net rotation angle π applied with the appropriate phase corresponding to the X axis in the rotating frame. The pulse timings (τ_p, τ_w, and τ_C) used in the analytic derivation of the net rotation error are indicated. In the case of synchronized pulse sequences in rotating samples, the condition $\tau_w = N\tau_R$ (i. e. that the period of pulse application is a multiple of the rotor period) is satisfied in order to obtain an echo. Under these conditions, the periodic resonance offset term recurs to the same value with each application of the π pulse. The pulses are separated by "windows" of length $(\tau_w - \tau_p)$.

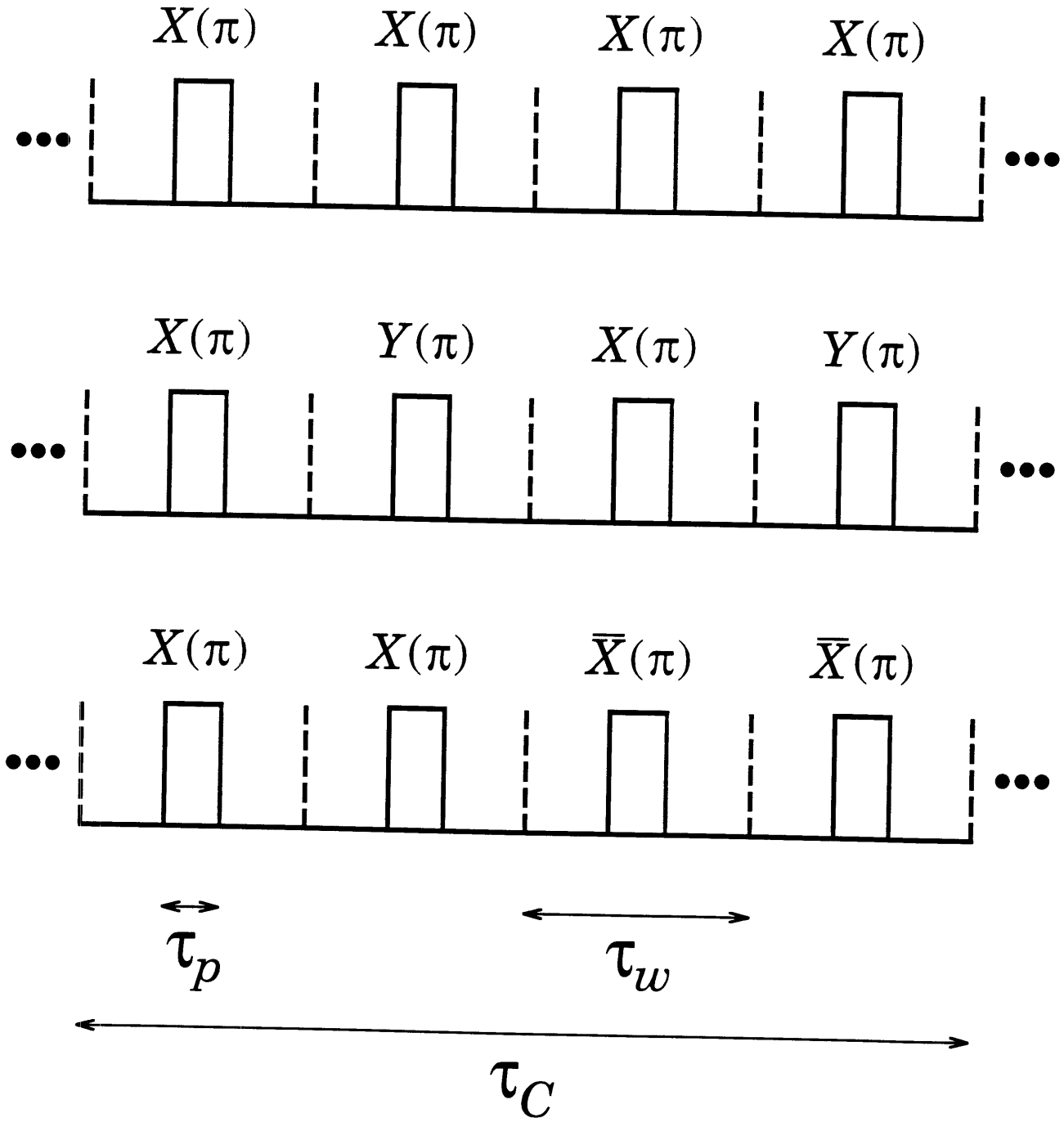
X(π)
X(π)
X(π)
X(π)
X(π)
Y(π)
X(π)
Y(π)
X(π)
X(π)
X̄(π)
X̄(π)
τp
τw
τC

III. Effect of Insufficient Proton Decoupling

A simple model which is useful in understanding the influence of proton decoupling on the performance of a π pulse applied to the dilute spins consists of the basic Hamiltonian:

$$H = \nu_I I_x + \nu_S S_x + d_{IS} \cdot 2 I_z S_z \,, \tag{4-11}$$

where ν_I and ν_S are the RF field amplitudes applied to the heteronuclear spin pair. The S spin, whose echo intensity is observed, is coupled to the I spin via d_{IS}. Although the decoupling field ν_I is typically applied continuously, the S spin RF field is active only for a short time τ_p in order to stimulate a π pulse rotation. During these intervals, the decoupling efficiency is generally reduced because of interference between the two fields. With sample rotation, this discussion again applies to the case $\tau_R >> \tau_p$. However, in the case of strong ^{1}H-^{1}H interactions, spin coherences involving the protons experience dephasing within a short time interval [22], strongly limiting the applicability of long compensated echo sequences to the refocusing of the large local fields which arise from insufficient decoupling. As a consequence, it is important to obtain efficient decoupling on the short time scale τ_p.

The mechanism of decoupling degradation can be understood by examining the time evolution operator during the short interval τ_p when the S spin pulse is applied:

$$U(\tau_p,0) = \exp\{-i\omega_I \tau_p I_x\}\exp\{-i\omega_S \tau_p S_x\}\times \left[T\exp\left\{-i\int_0^{\tau_p} dt\; d_{IS}\cdot 2\tilde{S}_z(t)\tilde{I}_z(t)\right\}\right]. \tag{4-12}$$

The angular frequencies ω_I and ω_S are defined as $\omega_I = 2\pi\,\nu_I$ and $\omega_S = 2\pi\,\nu_S$, and the spin operators are transformed into the toggling frame in order to investigate the joint behavior under the two RF fields. To evaluate the time evolution operator, the AHT approximation is employed under the reasonable assumption that both RF fields dominate the dipolar coupling:

$$U(\tau_p,0) \approx \exp\{-i\omega_I \tau_p I_x\}\exp\{-i\omega_S \tau_p S_x\}\times\exp\{-i\,H_D^{(0)}\tau_p\}. \tag{4-13}$$

where:

$$H_D^{(0)} = \frac{1}{\tau_p}\int_0^{\tau_p} dt\; d_{IS}\cdot 2\tilde{I}_z(t)\tilde{S}_z(t). \tag{4-14}$$

The evaluation of Eq. (4-14) leads to the following expression:

$$\begin{aligned} H_D^{(0)} = {} & d_{IS}\cdot I_z S_z\left\{\frac{\sin\{(\omega_I+\omega_S)\tau_p\}}{(\omega_I+\omega_S)\tau_p}+\frac{\sin\{(\omega_I-\omega_S)\tau_p\}}{(\omega_I-\omega_S)\tau_p}\right\} \\ & + d_{IS}\cdot I_z S_y\left\{\frac{1-\cos\{(\omega_I+\omega_S)\tau_p\}}{(\omega_I+\omega_S)\tau_p}-\frac{1-\cos\{(\omega_I-\omega_S)\tau_p\}}{(\omega_I-\omega_S)\tau_p}\right\} \\ & + d_{IS}\cdot I_y S_z\left\{\frac{1-\cos\{(\omega_I+\omega_S)\tau_p\}}{(\omega_I+\omega_S)\tau_p}+\frac{1-\cos\{(\omega_I-\omega_S)\tau_p\}}{(\omega_I-\omega_S)\tau_p}\right\} \\ & + d_{IS}\cdot I_y S_y\left\{\frac{\sin\{(\omega_I+\omega_S)\tau_p\}}{(\omega_I+\omega_S)\tau_p}-\frac{\sin\{(\omega_I-\omega_S)\tau_p\}}{(\omega_I-\omega_S)\tau_p}\right\}. \end{aligned} \tag{4-15}$$

Three cases deserve special attention. First, within the toggling frame approach, when the RF fields are matched in amplitude at the Hartmann Hahn condition $\omega_S = \omega_I$ [23], the coherent averaging effect of the dipolar coupling is spoiled by interference between the simultaneous modulations of the I and S spin operators. This resonance condition is fulfilled in cross polarization experiments [24] in order to stimulate rotating frame magnetization exchange. The effective dipolar coupling $H_D^{(0)}$ assumes the well-known form of a flip-flop interaction in the rotating frame defined along the x direction:

$$H_D^{(0)} = d_{IS} \cdot \left\{ I_z S_z + I_y S_y \right\}. \tag{4-16}$$

In order to minimize dephasing of the signal in spin echo experiments, this dipolar recoupling condition must clearly be avoided. However, in the case of a π pulse applied to the S spin, where $\omega_S \tau_p = \pi$, an especially large mismatch is required in order to reduce signal losses to an acceptable level. For example, if the Hartmann Hahn condition is mismatched by a factor of two, i. e. $\omega_I = 2\omega_S$, then the dipole-dipole interaction is still not eliminated even through zeroth order:

$$H_D^{(0)} = -\frac{2}{3\pi} d_{IS} \cdot I_z S_y + \frac{4}{3\pi} d_{IS} \cdot I_y S_z \,. \tag{4-17}$$

In fact, to eliminate $H_D^{(0)}$ over the course of the π pulse, the condition $\omega_I = 3\omega_S$ must be fulfilled. For more general pulse sequences, this stringent condition is relaxed somewhat. For τ_p such that $\omega_S \tau_p = 2\pi$, a case which is

realized in cases such as cross polarization where CW fields are employed, $H_D^{(0)}$ vanishes under the condition $\omega_I = 2\omega_S$, which is easier to fulfill.

On the other hand, over a single cycle τ_p of the decoupling field such that $\omega_I \tau_p = 2\pi$, the coupling vanishes in the absence of the S spin RF field. Since the efficiency of the decoupling field is reduced roughly according to the expression $\omega_I \rightarrow \omega_I - \omega_S$, it is necessary to apply particularly strong proton RF fields during double resonance echo experiments to minimize the decay of S spin coherences. In practice, the signal losses are reduced continuously as the decoupling field and the Hartmann Hahn ratio ω_I/ω_S are increased, as implied by Eq. (4-15); however, this simple model provides insight into the slow convergence which is observed. In Figures (4-2) and (4-3), the signal losses of both the CO_2 (which lacks an attached proton) and CH_2 resonances of glycine with one π pulse per rotor period [2] exhibit great improvements as the mismatch condition reaches $\omega_I = 3\omega_S$. The signal decay is also attenuated strongly with increasing ω_I for a fixed Hartmann Hahn ratio. It is not always practical to reduce ω_S for the purpose of achieving the condition $\omega_I \approx 3\omega_S$, since other finite pulse effects such as resonance offsets require the use of relatively strong RF fields ω_S. Within the limitations of the NMR probe, a compromise must be achieved for particular applications.

In order to interpret some recoupling experiments, it is necessary to provide a quantitative estimate of the time scale of coherence losses into the numerical simulations. To order to account for the attenuation of coherences, which plays an important role in the case of weak dipole-dipole coupling, an exponential model is employed in both the homonuclear π pulse recoupling experiments and in the heteronuclear dephasing experiments described in other chapters. In the absence of pulses, the longitudinal polarization does not decay on the 30 msec time scale because T_1 relaxation is much slower. To

model the loss of coherences from insufficient proton decoupling, an effective rate of decay Γ_p, which is the same for the longitudinal and transverse spin magnetizations, is chosen during the pulses.

In order to account for the somewhat faster observed transverse decay, an effective T_2 is also selected to match the observed rate of echo decay. This framework accounts for the observed multiple pulse echo intensities reasonably well in polycrystalline solids, and it provides a route to incorporating these influences explicitly in a way which is computationally tractable. The exponential model is most appropriate at lower decoupling fields and for protonated resonances, where the Hartmann Hahn depolarization effect is especially significant. Although this approach provides effective relaxation parameters for multiple pulse experiments, it is more appropriate to apply a single pulse echo experiment in measuring the true homogeneous T_2 due to molecular motion. With a single pulse, the depolarization effect does not accumulate with time.

Experimental Procedure. The echo experiments discussed here were performed at 317 MHz for protons with a home-built spectrometer and double resonance probe with a 7 mm double bearing MAS assembly (Doty Scientific, Columbia, SC). The echo sequence consists of one π pulse applied per rotor period with the *XYXY YXYX* $\overline{XYXY}$ $\overline{YXYX}$ (*XY*-16) compensation scheme. The analog phase splitters were balanced within 0.1° and the amplitudes balanced within 0.1%. The RF field amplitudes are indicated in the figures. Echo intensities from samples of polycrystalline $^{13}CO_2$-labeled and $^{13}CH_2$ glycine, recrystallized with ten-fold dilution in natural abundance material, were acquired with the isotropic peaks placed on resonance at 4800 ± 2 Hz spinning speed. With a 69.4 kHz decoupling field, the observed full widths at half maximum (FWHM) of the $^{13}CO_2$ and $^{13}CH_2$ glycine resonance lines are

35 Hz and 85 Hz, respectively; and with a 54.3 kHz decoupling field, 34 Hz and 111 Hz, respectively. The additional line-broadening in the methylene line arises from insufficient decoupling power, but this contribution does not behave homogeneously in these experiments.

Figure (4-2). Echo decay signals of the CO_2 resonance of glycine as a function of several ^{13}C and ^{1}H RF field amplitudes in double resonance MAS experiments: (a) decay of longitudinal polarization; (b) decay of transverse X magnetization. The Hartmann Hahn depolarization effect discussed in the text is observed even in this unprotonated system. In 30 msec, a total of 144 pulses is applied. HF indicates the proton decoupling (high frequency) field strength, while LF indicates the ^{13}C RF field strength (low frequency). In addition, the dashed lines shown are simulation results with the parameters $\Gamma_p = 0.03$ kHz, $T_2 = 100$ ms at HF 69.4 kHz, LF 24.3 kHz; $\Gamma_p = 0.15$ kHz, $T_2 = 83$ ms at HF 54.3 kHz, LF 24.3 kHz. The evolution of the isolated spins is calculated explicitly including the CSA and finite pulses, in addition to the exponential decay parameters.

(a)

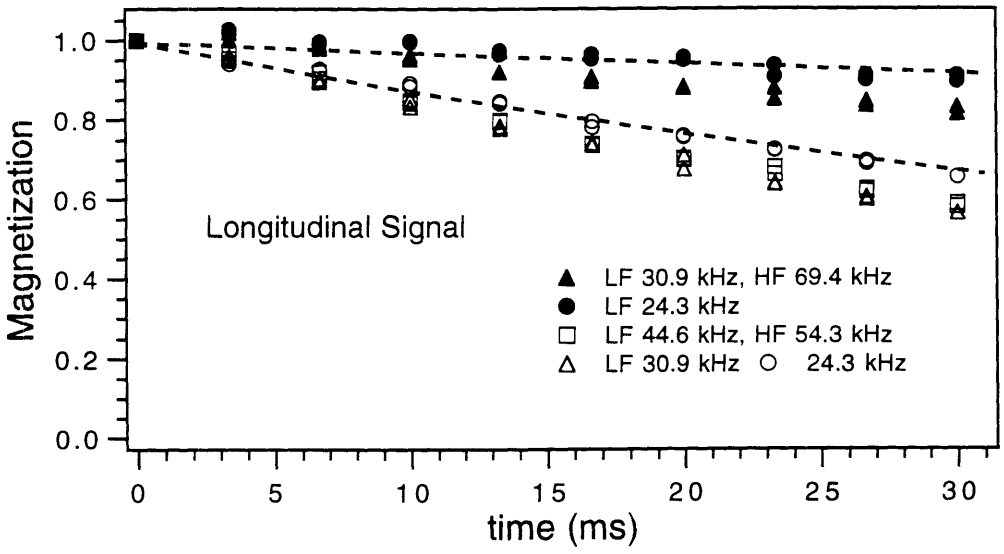
Magnetization
1.0
0.8
0.6
0.4
0.2
0.0
0
5
10
15
20
25
30
time (ms)
Longitudinal Signal
LF 30.9 kHz, HF 69.4 kHz
LF 24.3 kHz
LF 44.6 kHz, HF 54.3 kHz
LF 30.9 kHz
24.3 kHz

(b)

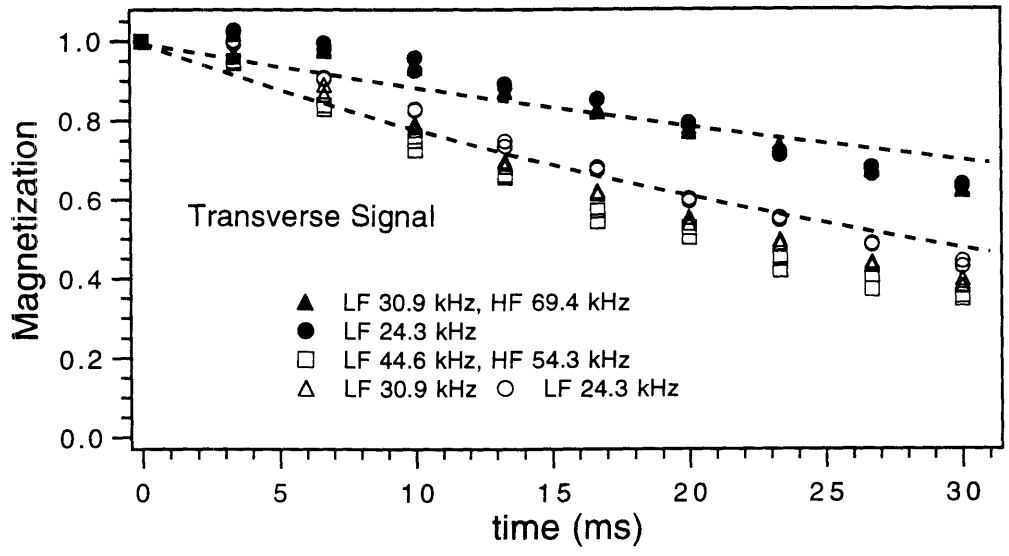
Magnetization
1.0
0.8
0.6
0.4
0.2
0.0
0
5
10
15
20
25
30
time (ms)
Transverse Signal
LF 30.9 kHz, HF 69.4 kHz
LF 24.3 kHz
LF 44.6 kHz, HF 54.3 kHz
LF 30.9 kHz
LF 24.3 kHz

Figure (4-3). Echo decay signals of the CH_2 resonance of glycine as a function of several ^{13}C and ^{1}H RF field amplitudes in double resonance MAS experiments: (a) decay of longitudinal polarization; (b) decay of transverse X magnetization. The transverse decay is somewhat more rapid because of insufficient proton decoupling between the pulses and T_2 relaxation. The dashed lines are simulation results with the parameters $\Gamma_p = 0.45$ kHz, $T_2 = 50$ ms at HF 69.4 kHz, LF 24.3 kHz; $\Gamma_p = 2.50$ kHz, $T_2 = 50$ ms at HF 54.3 kHz, LF 24.3 kHz.

(a)

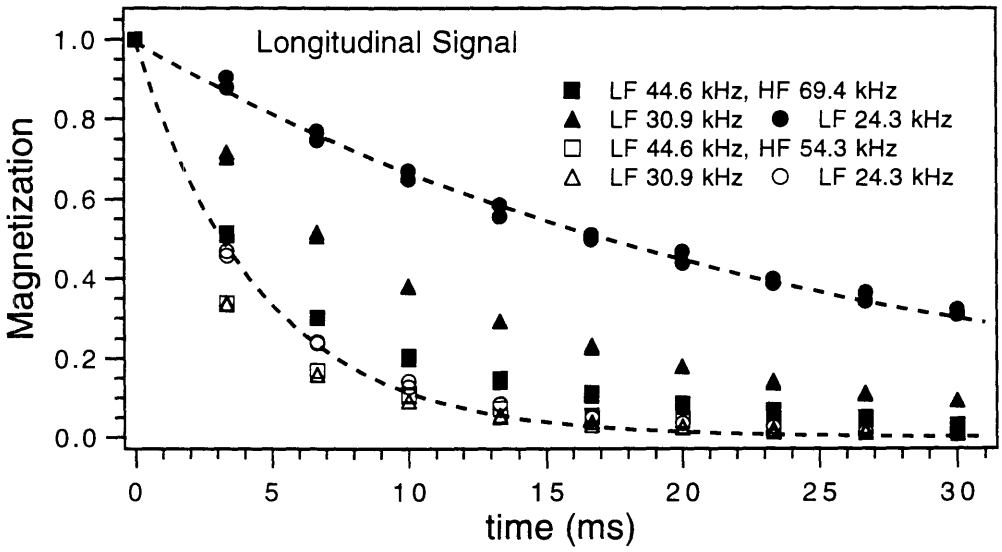
Longitudinal Signal
LF 44.6 kHz, HF 69.4 kHz
LF 30.9 kHz
LF 24.3 kHz
LF 44.6 kHz, HF 54.3 kHz
LF 30.9 kHz
LF 24.3 kHz
Magnetization
time (ms)
0.0
0.2
0.4
0.6
0.8
1.0
0
5
10
15
20
25
30

(b)

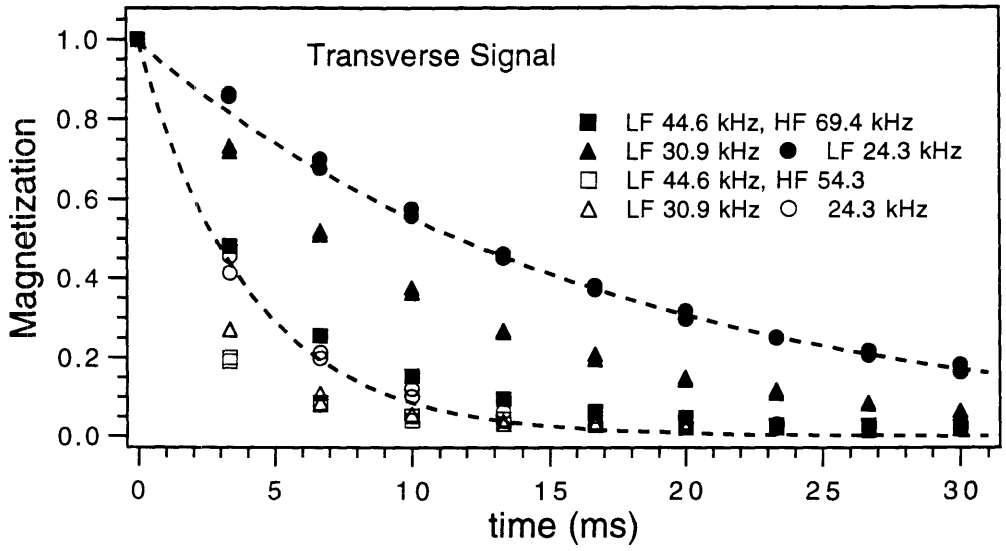
Transverse Signal
LF 44.6 kHz, HF 69.4 kHz
LF 30.9 kHz
LF 24.3 kHz
LF 44.6 kHz, HF 54.3
LF 30.9 kHz
24.3 kHz
Magnetization
time (ms)
0.0
0.2
0.4
0.6
0.8
1.0
0
5
10
15
20
25
30

IV. Conclusion

The analytic framework presented here for calculating the rotation error obtained with compensated echo sequences leads to the conclusion that there is little difference between the basic $XYXY$ and $XX\overline{XX}$ cycles for RF inhomogeneity and resonance offsets, which are important influences in double resonance MAS applications involving dilute spins. For rotor-synchronized pulse sequences, these general conclusions are applicable because the resonance offset assumes the same value at each interval τ_p. However, for alternative MAS echo sequences, such as 8 π pulses per rotor period [25], the resonance offset is constantly changing, invalidating the time-independent analysis discussed here. In the windowless limit where the accumulated phase between the pulses vanishes, $XX\overline{XX}$ is better in principle. For sequences such that $\tau_w = N\tau_R$, because the phase accumulated from the CSA vanishes between the pulses under magic angle spinning, the MLEV-4 cycle is also more favorable for overcoming this perturbation.

However, in practice, the signal decay is frequently dominated by the insufficient decoupling effect, so these subtle distinctions are not easy to observe in MAS experiments. The condition $\omega_I >> 2\omega_S$ must be fulfilled in order to eliminate the heteronuclear coupling completely, necessitating a decoupling field >100 kHz, which is difficult to achieve. Under the conditions in Figures (4-2) and (4-3), numerical simulations of the isolated spins predict signal losses of $\leq 1\%$ after 30 msec in the absence of relaxation effects, even with RF inhomogeneities of $\pm 10\%$. In crystalline solids, the signal relaxation from molecular motion is also extremely slow in most cases and is therefore typically an insignificant contribution to the NMR linewidths of dilute spins

[26]. In hexamethylbenzene, for example, T_2 relaxation contributes less than 2 Hz to the line-broadening in CPMAS experiments [27].

The *XY*-16 sequence compensates partially for the insufficient decoupling effect, but cannot refocus it fully because of the complications of MAS and strong ^1H-^1H interactions. In addition, various random fluctuations in the output of the RF transmitter and the mechanical rotation contribute other possible sources of echo decay. The net loss of the spin coherences can often be modeled adequately with exponential decay parameters. Although the particular cases of RF inhomogeneity and resonance offsets are investigated here, the *XYXY* and MLEV sequences compensate in a similar way for any rotation error which is fixed for each pulse, so other imperfections such as phase transients are similarly corrected.

References for Chapter 4.

[1] C. P. Slichter, *Principles of Magnetic Resonance* (Springer-Verlag, Berlin, 1990).

[2] E. T. Olejniczak, S. Vega, and R. G. Griffin, J. Chem. Phys. **81**, 4804 (1984).

[3] A. C. Kolbert, D. P. Raleigh, and R. G. Griffin, J. Mag. Res. **82**, 483 (1989).

[4] A. E. Bennett, R. G. Griffin, and S. Vega, NMR Basic Principles and Progress **33**, 1 (1994).

[5] A. A. Maudsley, J. Mag. Res. **69**, 488 (1986).

[6] T. Gullion, D. B. Baker, and M. S. Conradi, J. Mag. Res. **89**, 479 (1990).

[7] J. J. Kotyk, J. R. Garbow, and T. Gullion, J. Mag. Res. **89**, 647 (1990).

[8] T. Gullion and J. Schaefer, J. Mag. Res. **92**, 439 (1991).

[9] J. R. Garbow and T. Gullion, J. Mag. Res. **95**, 442 (1991).

[10] T. Gullion and S. Vega, Chem. Phys. Lett. **194**, 423 (1992).

[11] A. E. Bennett, J. H. Ok, R. G. Griffin, and S. Vega, J. Chem. Phys. **96**, 8624 (1992).

[12] A. J. Shaka, S. P. Rucker, and A. Pines, J. Mag. Res. **77**, 606 (1988).

[13] M. H. Levitt, R. Freeman, and T. Frenkiel, J. Mag. Res. **50**, 157 (1982).

[14] O. Weintraub and S. Vega, J. Mag. Res. A **105**, 245 (1993).

[15] W. P. Aue, D. J. Ruben, and R. G. Griffin, J. Chem. Phys. **80**, 1729 (1984).

[16] M. H. Levitt and R. Freeman, J. Mag. Res. **43**, 65 (1981).

[17] M. H. Levitt, Prog. NMR Spectroscopy **18**, 61 (1986).

[18] R. R. Ernst, G. Bodenhausen, and A. Wokaun, *Principles of Nuclear Magnetic Resonance in One and Two Dimensions* (Clarendon Press,

Oxford, 1987).

[19] T. Gullion, J. Mag. Res. A **101**, 320 (1993).

[20] T. Gullion and J. Schaefer, Adv. Mag. Res. **13**, 58 (1989).

[21] A. E. Bennett, unpublished results (1995).

[22] M. Mehring, *Principles of High Resolution NMR in Solids* (Springer-Verlag, Berlin, 1983).

[23] S. R. Hartmann and E. L. Hahn, Phys. Rev. **128**, 2042 (1962).

[24] A. Pines, M. G. Gibby, and J. S. Waugh, J. Chem. Phys. **59**, 569 (1973).

[25] J. H. Ok, R. G. S. Spencer, A. E. Bennett, and R. G. Griffin, Chem. Phys. Lett. **197**, 389 (1992).

[26] D. L. VanderHart, W. L. Earl, and A. N. Garroway, J. Mag. Res. **44**, 361 (1981).

[27] B. A. Cowans and J. B. Grutzner, J. Mag. Res. A **105**, 10 (1993).

Chapter 5.

Frequency-Selective Heteronuclear Dipolar Recoupling

I. Introduction

Several methods have recently been introduced for the purpose of restoring dipolar couplings into magic angle spinning experiments [1]. These techniques are useful for the measurement of internuclear distances [2, 3] and, more generally, for filtering and correlation experiments in polycrystalline materials [4-7]. For homonuclear spin pairs, the rotational resonance (R2) experiment [8, 9] provides a technique which is frequency-selective in that only pairs of spins whose chemical shift difference matches a multiple of the spinning frequency, i. e. $\Delta\delta = m\nu_R$, are recoupled. In the case of heteronuclear spins, a particularly successful recoupling technique has been the Rotational Echo Double Resonance (REDOR) experiment [10-12]. The dipolar dephasing trajectory obtained with REDOR is ideally non-selective with respect to the frequencies of the nuclear spins.

However, there are cases where an approach which recouples heteronuclear spins only at certain frequencies is of interest. Two examples are organic samples with multiple isotope labels and inorganic samples with broad inhomogeneous linewidths [13]. Here, a method is introduced for restoring heteronuclear couplings which is spectrally selective – in particular, the dipole-dipole coupling is restored to the MAS experiment only at exact resonance and at multiples of the spinning frequency [14]. Analogous multiple pulse experiments are also applicable to static solids, and a selective Spin Echo Double Resonance (SEDOR) experiment [15, 16] which yields information about relative chemical shift anisotropy tensor orientations is introduced.

Figure (5-1) illustrates the basic pulse sequence which is used to monitor the decay of S spin magnetization in the presence of coupling to I spins in a

triple resonance dephasing experiment with magic angle spinning. A compensated spin echo sequence [17] of one π pulse per rotor period is applied to the observed S spin in order to refocus its chemical shift interactions [18], while the combined application of pulses to the S and I spin systems leads to frequency-selective dipolar recoupling. This effect can be understood through the use of Average Hamiltonian Theory (AHT) [19-20]. Unfortunately, the basic pulse sequence applied to the I spin in Figure (5-1), $X(\pi/2)\,\overline{X}(\pi/2)$, is poorly compensated with respect to phase transients which occur at the leading and trailing edges of each RF pulse [21-23], and it is also not highly tolerant to resonance offset effects. Consequently, the pulse sequence illustrated in Figure (5-2) is more suitable for difficult applications such as the measurement of weak dipolar couplings. Illustrated in the figure is one half of the complete cycle of pulses applied to the I spin. The entire compensated sequence consists of the following:

$X(\pi/2)\,\overline{X}(\pi)\,\overline{X}(\pi)\,X(\pi)\,X(\pi/2)--X(\pi/2)\,X(\pi)\,\overline{X}(\pi)\,\overline{X}(\pi)\,X(\pi/2)--$,

where the dashes represent delays of one rotor period each. Although this phase alternation scheme was determined primarily through experimentation with numerical simulations, it is essentially a modified MLEV-8 cycle [17], which provides a high degree of compensation for resonance offsets, phase transients, RF inhomogeneity, and other pulse errors. Here $X(\pi/2)$ indicates a $90°$ pulse applied along the X axis in the rotating frame.

Figure (5-1). Basic pulse sequence for the frequency-selective dipolar recoupling (FDR) experiment with observation of dipolar dephasing. Following cross polarization, the spin echo signal of the observed S spins (e. g. ^{13}C) dephases under the the influence of pairs of $\pi/2$ pulses applied to non-observed I spins (e. g. ^{15}N). The length of the dephasing period is incremented in successive experiments, and the signal is acquired and integrated to the obtain the signal intensity (indicated by solid circles) as a function of mixing time. Since cross polarization and proton decoupling are required, an MAS probe simultaneously tuned to three RF channels is employed in heteronuclear recoupling experiments. In addition, the condition of rotor-synchronization (i. e. that one pulse is applied on each channel per rotor period τ_R) must be maintained within a few Hz.

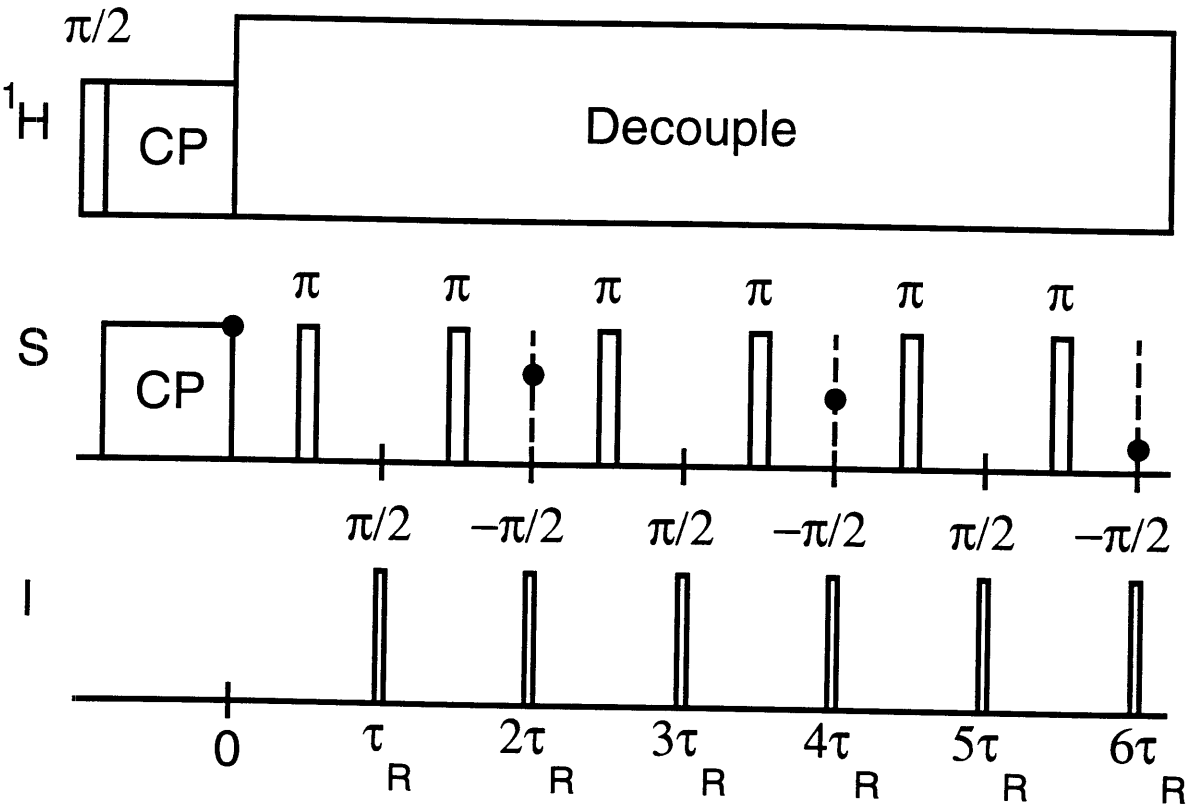
π/2
^{1}H
CP
Decouple
S
CP
π
π
π
π
π
π
π/2
−π/2
π/2
−π/2
π/2
−π/2
I
0
τ R
2τ R
3τ R
4τ R
5τ R
6τ R

Figure (5-2). Compensated pulse sequence for the frequency-selective dipolar dephasing experiment. Only the dilute S and I spin channels in the triple resonance experiment are shown. While the compensated XY-8 sequence $XYXY\ YXYX$ is applied to the S spin, a sequence analogous to MLEV-8 is applied to the I spin channel as follows:
$X(\pi/2)\ \overline{X}(\pi)\ \overline{X}(\pi)\ X(\pi)\ X(\pi/2)--X(\pi/2)\ X(\pi)\ \overline{X}(\pi)\ \overline{X}(\pi)\ X(\pi/2)--$.
Half of the I spin cycle is illustrated in the figure, while the complete sequence occupies twelve rotor cycles. Simultaneous compensation through the level of XY-8 and MLEV-8 on both channels is obtained after multiples of twenty-four rotor periods, the least common multiple of eight and twelve.

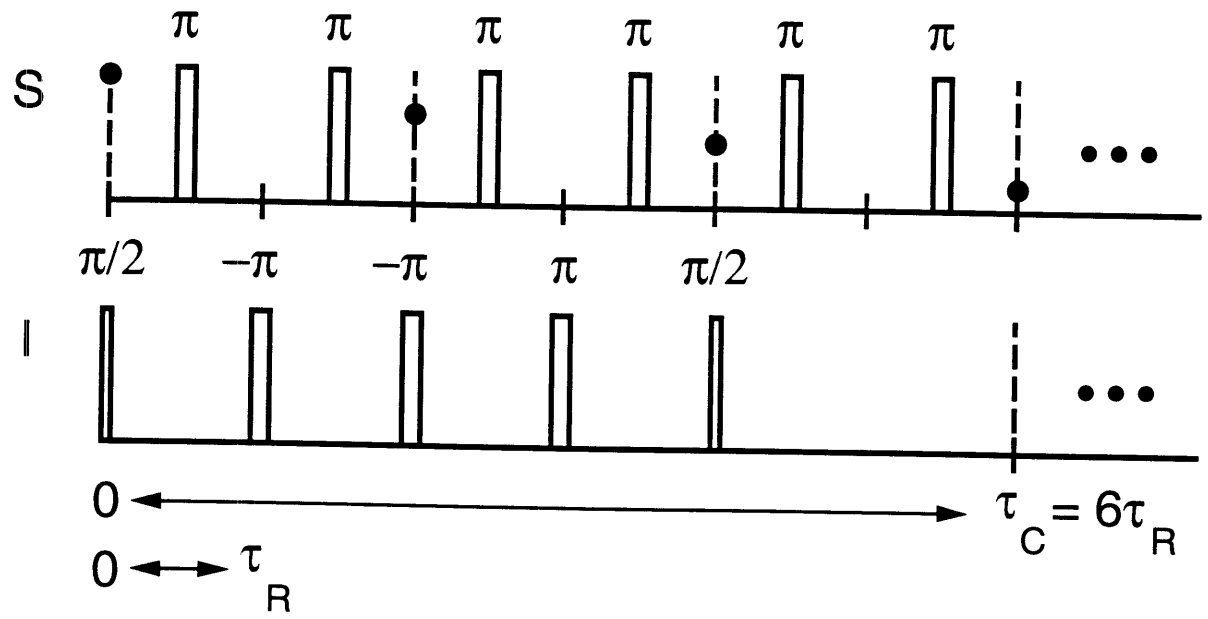
S
I
π
π
π
π
π
π
π/2
−π
−π
π
π/2
0
τ_C = 6τ_R
0
τ_R

II. Average Hamiltonian Analysis

Analysis of the pulse sequence shown in Figure (5-1) by AHT provides a means of understanding how frequency-selectivity is obtained. For the two spin case, the appropriate Hamiltonian includes the chemical shifts of the observed S spin and the non-observed I spin, as well as the heteronuclear dipole-dipole coupling between them. In a toggling frame defined by the RF pulses, the Hamiltonian can be divided as follows:

$$\begin{aligned}\tilde{H}_{\text{int}}(t) &= \tilde{H}_S(t) + \tilde{H}_I(t) + \tilde{H}_{IS}(t) \\ &= \delta_S(t)\tilde{S}_z(t) + \delta_I(t)\tilde{I}_z(t) + d_{IS}(t)\cdot 2\tilde{I}_z(t)\tilde{S}_z(t)\,,\end{aligned} \tag{5-1}$$

where the angular momentum operators A_α acquire time-dependence via the relationship:

$$\tilde{A}_\alpha(t) = U_{RF}^{-1}(t,0)A_\alpha U_{RF}(t,0)\,. \tag{5-2}$$

The pulses applied on the S spin channel act only on S_z in the toggling frame, while $\tilde{I}_z(t)$ acquires its time-dependence from the RF pulses applied near the I spin Larmor frequency. Using the Fourier expansions of the spatial prefactors, the AHT calculation results in the following effective Hamiltonian:

$$\begin{aligned}\tilde{H}_{\text{int}}^{(0)} &= \frac{1}{2}\hat{\delta}_I[0]\{I_z - I_y\} + \frac{1}{2}\bar{d}_{IS}\cdot 2\{I_z + I_y\}S_z \\ &= \frac{1}{\sqrt{2}}\hat{\delta}_I[0]I_{x'} + \frac{1}{\sqrt{2}}\bar{d}_{IS}\cdot 2I_{z'}S_z\,,\end{aligned} \tag{5-3}$$

where $\hat{\delta}_I[0]$ is the isotropic chemical shift (i.e. the frequency shift of the transmitter from resonance), and $\bar{d}_{IS}$ is the effective dipolar coupling constant, which depends on the crystallite orientation via (θ_{IS}, ϕ_{IS}):

$$\bar{d}_{IS} = -\frac{\sqrt{2}}{2\pi^2}\left(\frac{\mu_0}{4\pi}\right)\left\{\frac{\gamma_S \gamma_I \hbar}{r_{IS}^3}\right\}\sin(2\theta_{IS})\sin(\phi_{IS}). \qquad (5\text{-}4)$$

Here, the angular momentum operators of the I spin have been rearranged in order to simplify further calculations according to the following unitary transformation: $I_{x'} = 1/\sqrt{2}\{I_z - I_y\}$, $I_{y'} = I_y$, $I_{z'} = 1/\sqrt{2}\{I_z + I_y\}$.

Although the AHT approximation has been applied to evaluation of the effective dipolar coupling [1, 14], the disappearance of the I spin chemical shift anisotropy (CSA) from the effective Hamiltonian is an exact result for δ-function pulses, since the I spin chemical shift commutes with the other terms in the spin Hamiltonian during the complete rotor periods placed between the I spin pulses. Likewise, the S spin chemical shift $\tilde{H}_S(t)$ always commutes with the rest of the Hamiltonian and therefore cancels entirely from the dipolar dephasing dynamics. With strong RF pulses, large chemical shift anisotropies are therefore not expected to impair the measurement of weak dipole-dipole couplings, even in the case of ^{31}P nuclei, where the magnitude of the CSA can exceed 500 ppm [24].

In REDOR experiments, π pulse sequences with various timings are applied to both the S and I spins in order to spoil the rotational refocusing of the dipolar coupling [11]. In a toggling frame defined by the π pulses, the chemical shift term of the I spin also commutes with the heteronuclear coupling at all times and consequently does not influence the dynamics of S spin evolution. Therefore, REDOR experiments are not spectrally selective.

In the simple case where one π pulse is applied per rotor period to each spin, and the S and I spin pulses are placed completely out of phase, the effective Hamiltonian for REDOR dephasing adopts the simple form [25]:

$$\tilde{H}_{\text{int}}^{(0)} = \bar{d}_{IS} \cdot 2I_z S_z \,. \tag{5-5}$$

In the frequency-selective extensions presented here, the effective dipolar coupling is scaled down by $1/\sqrt{2}$ relative to the interaction recovered in REDOR experiments, because the dipolar interaction is averaged about two orthogonal directions in spin space.

Since the transformed operators $I_{z'}$ and $I_{x'}$ are orthogonal, the expression given by Eq. (5-3) is identical to the Hamiltonian which describes heteronuclear spin decoupling with a single phase RF field. Under the influence of the effective Hamiltonian, the transverse magnetization of the S spin evolves according to the following expression, which is valid for synchronous sampling at times $t = n\tau_C$:

$$\langle S_x(t)\rangle = \left\{\frac{\hat{\delta}_I^2[0]}{\hat{\delta}_I^2[0]+\bar{d}_{IS}^2}\right\} + \left\{\frac{\bar{d}_{IS}^2}{\hat{\delta}_I^2[0]+\bar{d}_{IS}^2}\right\} \cos\left\{2\pi\sqrt{\tfrac{1}{2}\left(\hat{\delta}_I^2[0]+\bar{d}_{IS}^2\right)}\,t\right\}. \tag{5-6}$$

At exact resonance, where $\hat{\delta}_I[0] = 0$, the dipolar dephasing trajectory proceeds under a scaled dipole-dipole coupling, as in REDOR experiments:

$$\langle S_x(t)\rangle = \cos\left\{\frac{1}{\sqrt{2}} \cdot 2\pi \bar{d}_{IS} t\right\}. \tag{5-7}$$

In the spin dynamics, $\hat{\delta}_I[0]$ plays the role of the decoupling field. In the limit where $\hat{\delta}_I[0]$ greatly exceeds the dipolar coupling $\bar{d}_{IS}$, the dephasing

trajectory is quenched, and $\langle S_x(t)\rangle = 1$ at all times. More generally, the selectivity of the pulse sequence is determined by the magnitude of dipolar constant $\overline{d}_{IS}$.

With the compensated version of the frequency-selective sequence shown in Figure (5-2), the effective Hamiltonian is modified somewhat:

$$\tilde{H}_{\text{int}}^{(0)} = \frac{1}{3}\hat{\delta}_I[0]I_z + \frac{2}{3}\overline{d}_{IS}\cdot 2I_xS_z\,. \tag{5-8}$$

The dipolar coupling is scaled down by 2/3 in this case, which is slightly smaller than the scaling factor of $1/\sqrt{2}$ recovered with the first sequence. The effective frequency offset is reduced even further. The smaller resonance offset is of possible advantage in observing weak dipolar couplings because the frequency dispersion from inhomogeneous line-broadening is reduced, and consequently does not promote undesirable quenching of the dephasing effect in the neighborhood of resonance.

The compensated version of the sequence also provides a simple means of time-reversing a dipolar dephasing trajectory. With phase reversal of all pulses on the I spin channel, the effective dipolar coupling constant appearing in Eq. (5-8) is inverted in sign, i. e. $\overline{d}_{IS} \rightarrow -\overline{d}_{IS}$. Therefore, a rotor-synchronized interval of dephasing, followed by a similar period where the phases of all the I spin pulses are rotated by π, refocuses the formation of non-observable two spin coherences from the S spin magnetization, resulting in a complete echo of the signal.

III. Dipolar Dephasing Experiments

Figure (5-3) demonstrates the dephasing trajectories observed in polycrystalline 2-^{13}C-^{15}N-glycine with the basic pulse sequence of Figure (5-1). For comparison, the REDOR dephasing curve at resonance, obtained by changing the I spin pulse lengths according to $\pi/2 \rightarrow \pi$, is also shown, illustrating the somewhat faster dephasing trajectory obtained with π pulses. The directly bonded spin pair has a dipolar coupling constant of -950 Hz, corresponding to an internuclear distance of 1.48 Å according to neutron diffraction [26]. The signal trajectory is renormalized with respect to the signal decay observed without pulses on the I spin channel (^{15}N in this example) [2]. In this way, the influence of other contributions to the signal decay is removed. On resonance, a scaled REDOR dephasing trajectory is observed with the frequency-selective sequence. In both cases, the signal disappears at long times because of the inhomogeneous distribution of crystallite orientations, and therefore dipolar couplings, present in a powder sample. Off resonance, the quenching of the dipolar recoupling effect is demonstrated.

The simulations involve exact numerical calculation of the evolution of the S spin transverse magnetization in the two spin system, including the effect of finite pulses. However, even with the relatively weak RF pulses employed here, the finite pulse effect is insignificant, and simulations with δ-function pulses yield the same results as the finite pulse calculations within ± 0.02, where the initial magnetization is defined as unity. Although the agreement between the experiments and simulations is quite good, the AHT trajectories differ somewhat from the exact results because the cycle time of two rotor periods (830 ms at 2.41 kHz spinning speed) is not extremely short

compared to the inverse of the 950 Hz coupling strength, and consequently higher order terms in the Magnus expansion make a significant contribution. In contrast, the AHT result for REDOR in Eq. (5-5) is exact with δ-function pulses because the toggling frame Hamiltonian always commutes with itself at different times, and the trajectories predicted by AHT and the numerical calculations are therefore in close agreement. In both cases, the finite widths of the pulses have little effect and can be neglected.

Experimental Procedures. All of the results obtained in this chapter were obtained on a 7.4 T home-built NMR spectrometer (79.9 MHz for ^{13}C). The sample discussed here is 2-^{13}C-^{15}N-glycine, 99% enriched in both isotopes. The experiment was conducted with a spinning speed of 2.410 kHz using an home-built triple resonance probe with a commercially available 5 mm double bearing MAS assembly (Doty Scientific Inc., Columbia, SC). The $\pi/2$ pulse lengths were 3.1 μs for ^{1}H (with the corresponding decoupling power strength), 4.8 μs for ^{13}C, and 5.4 μs for ^{15}N, and the trajectory was sampled every two rotor periods. Rotor-synchronization was maintained within ± 5 Hz by means of an home-built spinning speed controller.

Figure (5-3). Magnetization dephasing trajectories of the ^{13}C (S spin): (a) on and off of resonance (by 1 kHz) on the ^{15}N (I spin) RF channel for 2-^{13}C-^{15}N-glycine; (b) comparison of the basic frequency-selective sequence with the analogous non-selective pulse scheme obtaining by modifying the I spin pulses according to $\pi/2 \rightarrow \pi$, with the ^{15}N on resonance. The experimental trajectories, numerical simulations with finite pulses, and the dephasing curves predicted by AHT are shown. Numerical calculations with delta-function pulses (i. e. infinitely short and strong for a given total flip angle) yield imperceptibly different results from those obtained with finite pulses in the case shown here.

(a)

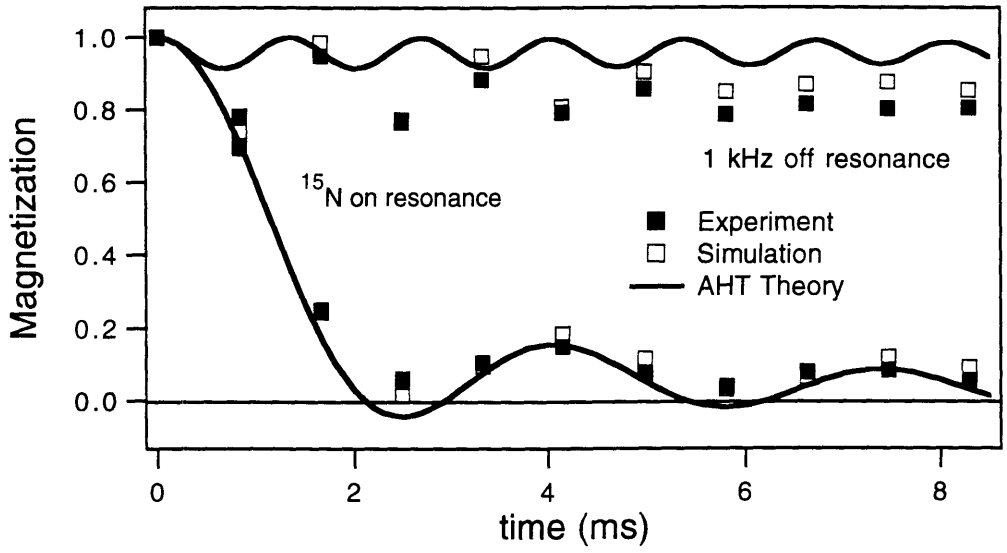
Magnetization
1.0
0.8
0.6
0.4
0.2
0.0
0
2
4
6
8
time (ms)
^{15}N on resonance
1 kHz off resonance
Experiment
Simulation
AHT Theory

(b)

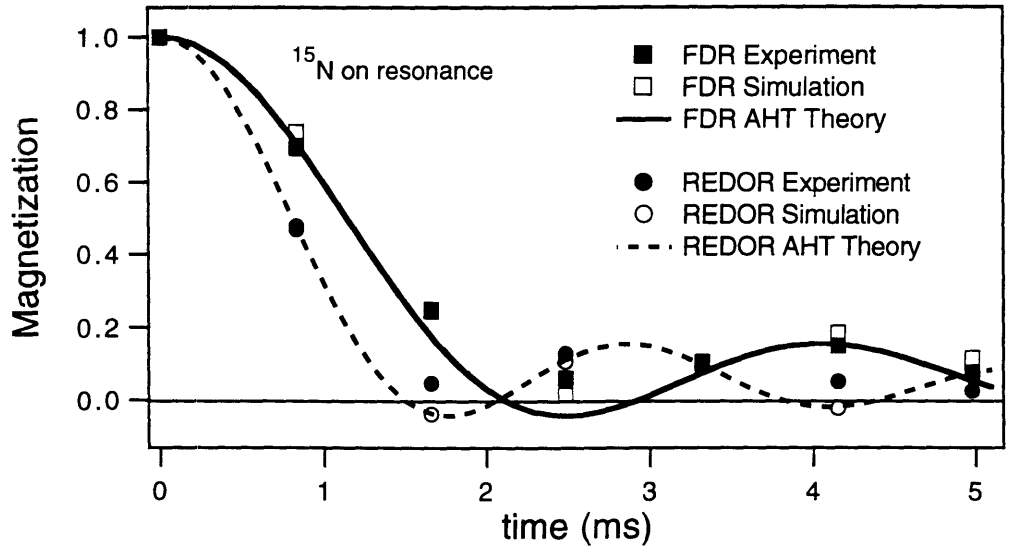
Magnetization
1.0
0.8
0.6
0.4
0.2
0.0
0
1
2
3
4
5
time (ms)
^{15}N on resonance
FDR Experiment
FDR Simulation
FDR AHT Theory
REDOR Experiment
REDOR Simulation
REDOR AHT Theory

A second example is the case of 1-^{13}C-^{15}N-glycine, where the dipolar coupling is weaker (i. e. -200 Hz coupling constant corresponding to 2.49 Å [26]). In Figure (5-4), several dephasing trajectories obtained with the compensated sequence are shown with increasing I spin resonance offsets. At resonance, and even more so in the immediate neighborhood of resonance, there are some discrepancies between the simulations and experiments. These inconsistencies appear to arise from incoherence in the evolution of the spin system. In addition to T_1 and T_2 relaxation, random fluctuations in the rotor phase, the RF excitation, and the synchronization between them contribute possible sources of coherence decay in the two spin system. Especially in the case of protonated nuclei, insufficient proton decoupling is another major source of signal losses.

With the compensated FDR sequence applied on resonance, the spin trajectory proceeds with exchange between the S spin magnetization and two spin coherence according to the following approximate expression:

$$\rho(t) = S_x \cos\left\{\tfrac{2}{3} \cdot 2\pi \bar{d}_{IS} t\right\} + 2S_y I_x \sin\left\{\tfrac{2}{3} \cdot 2\pi \bar{d}_{IS} t\right\}. \qquad (5\text{-}9)$$

With δ-function pulses, the exact trajectory involves at most the four coherences: S_x, $2S_yI_x$, $2S_yI_y$, and $2S_yI_z$. In the current example, finite pulse simulations predict the refocusing of the S spin magnetization within 2% when 12 ms of dephasing is followed by the time reversal sequence for another period of 12 ms. However, in the experiment, 12% of the echo intensity is lost following the complete 24 ms period. This signal loss is straightforward to treat with the adoption of an exponential decay model.

In the usual way [2, 10], the experimental background decay of the S spin magnetization is eliminated by renormalization of the signal with the

reference intensity obtained without pulses applied to the ^{15}N spin [2]. The dephasing function which is plotted to reveal the dipolar evolution consists of S/S_0 where S is the signal with I spin pulses, and S_0 is the signal obtained without I spin pulses. Although this approach accounts for the inevitable loss of S spin magnetization during the π pulse train, it fails to include the differential rates of decay among the various spin coherences, which do not cancel from the spin dynamics.

With a single parameter Γ to describe the differential decay rates of the two spin coherences, $2S_yI_x$, $2S_yI_y$, and $2S_yI_z$, relative to the single spin coherence S_x, the δ-function simulations yield good agreement with the experimental results acquired with several offsets of the ^{15}N frequency from resonance. The dipole-dipole coupling constant of -195 Hz (corresponding to an internuclear distance of 2.51 Å) matches the results better than the neutron diffraction value of -200 Hz. In the simulations, the choice of dephasing constant $\Gamma = 25$ Hz leads to recovery of only 81% of the echo intensity after 24 ms in a simulation where 12 ms of dephasing is followed by 12 ms of time reversal refocusing. The influence of the incoherence parameter Γ on the results is greatest for small departures from resonance, because at those values there is considerable formation of two spin coherence during the trajectory, followed by its partial refocusing at longer times. Consequently, the faster decay rates of the two spin coherences compared to the S spin magnetization has the largest impact for these trajectories. Similar considerations are possibly of significance in the measurement of extremely weak dipole-dipole couplings (i. e. approximately 20-100 Hz) using REDOR dephasing experiments, where distortions in the trajectory have been observed at long times [27, 28].

The AHT treatment becomes inappropriate for the case of large resonance offsets. Although it properly predicts the quenching of the dephasing trajectory with increasing offset, it fails to predict the harmonics which are observed with the frequency-selective sequence. Specifically, with the basic sequence, where full rotor periods of evolution are placed between the pulses, trajectories for which the resonance offset is any multiple of the spinning frequency, $\hat{\delta}_I[0] = m\nu_R$, are indistinguishable from the behavior on resonance. For the sequence in Figure (5-2), two rotor periods of chemical shift evolution are required in order to achieve favorable tolerance to RF pulse errors; therefore, harmonic behavior is observed at all frequencies which satisfy the condition $\hat{\delta}_I[0] = {}^1\!/_2\, m\nu_R$. Alternative trial compensation schemes employing at most one rotor period of free evolution under the frequency offset were unfortunately found to be susceptible to RF inhomogeneity.

Figure (5-4). Dipolar dephasing trajectories with ^{13}C observation in 1-^{13}C-^{15}N-glycine. The experimental results and the corresponding δ-function pulse simulations with and without the differential decay parameter $\Gamma = 25$ Hz for the two spin coherences are shown. The influence of finite pulse lengths is again negligible in this example. The O parameter indicates the offsets of the RF transmitter on the ^{15}N channel from resonance.

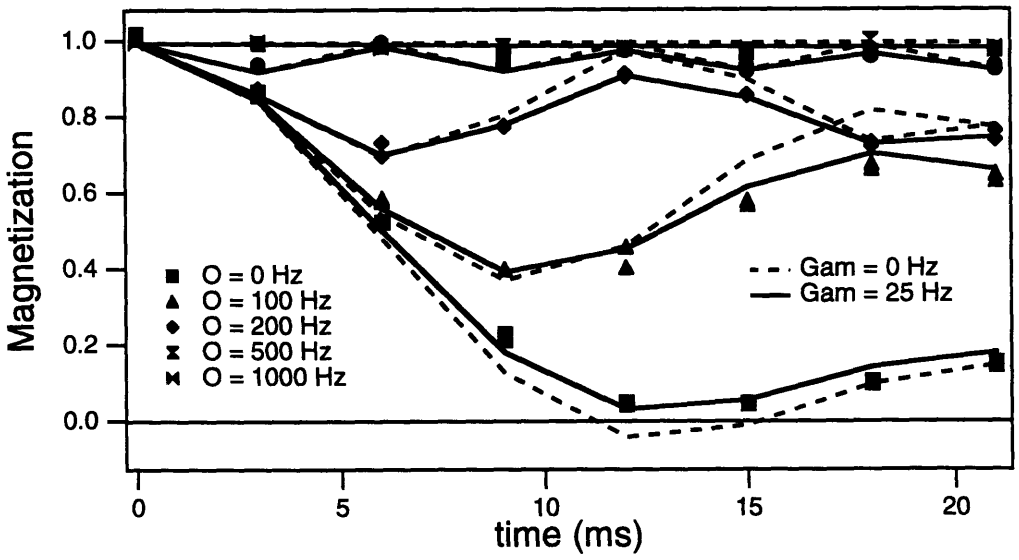
Magnetization
1.0
0.8
0.6
0.4
0.2
0.0
0
5
10
15
20
time (ms)
O = 0 Hz
O = 100 Hz
O = 200 Hz
O = 500 Hz
O = 1000 Hz
Gam = 0 Hz
Gam = 25 Hz

For the application of recoupling techniques to several spins, a simple test case is the dipeptide glycylglycine, ^{13}C-labeled at the 1- and 4-positions and ^{15}N-labeled at both the N terminus and the peptide bond. Using frequency-selective dipolar dephasing experiments, the couplings of the ^{13}C spins to each ^{15}N can be observed separately. A schematic representation of the four spin system with the relevant heteronuclear interatomic distances is shown in Figure (5-5). The frequencies of the ^{13}C and ^{15}N nuclei are well-resolved, with the latter separated by 76.1 ppm, i. e. 2450 Hz at 32.2 MHz Larmor frequency for ^{15}N. Therefore, the FDR approach can be used to observe dipolar dephasing trajectories independently to each ^{15}N nucleus.

Figure (5-6) provides a demonstration of selective dephasing within the multiple spin environment. With the selection of the NH resonance in the peptide bond, the recoupling effect between the directly bonded ^{15}N-^{13}C pair with dipolar coupling strength -950 Hz is quenched while the $^{13}CH_2$ dephasing trajectory proceeds according to the weaker dipolar coupling of -225 Hz, the known value from its structure determination by X-ray [29] and neutron diffraction [30]. At the same time, the $^{13}CO_2$ proceeds according to its -205 Hz interaction with the NH spin. With the selection of the NH_3 group, it appears that $^{13}CO_2$ dephasing occurs selectively according to its very weak dipole-dipole coupling of -20 Hz to the N-terminus. However, at least some of the dephasing may result from imperfect quenching of the larger interaction from RF pulse and rotor synchronization errors. Further experiments with shorter pulse widths and improved spinning speed control will resolve the extent to which large interactions can be suppressed in practice.

Because of the relatively low RF field amplitudes employed in this experiment, the compensated sequence is employed in order to minimize

resonance offset effects and phase transients, and the dephasing trajectory is sampled every 12 rotor cycles. The trajectories are calculated with a three spin finite pulse simulation. Since there are five intermolecular distances involving the $^{13}CO_2$ and $^{13}CH_2$ resonances which are ≤ 5.4 Å, a simulated curve which is scaled according to the additional couplings is also shown. Here, the finite pulse widths affect the trajectories obtained with weak RF fields somewhat, while the ^{15}N-^{15}N (26 Hz) and ^{13}C-^{13}C (80 Hz) homonuclear couplings are too small to influence the results significantly. More generally, large homonuclear interactions, especially among the non-observed spins, are expected to perturb the results, most notably when the chemical shift differences between the interacting homonuclear spins nearly satisfy the rotational resonance condition [9].

Sample Preparation. The polycrystalline 1-^{13}C-^{15}N-glycine (Cambridge Isotopes Inc., Cambridge, MA) sample, 99% enriched in both isotopes, was recrystallized from deionized water with ten-fold dilution in natural abundance material. The polycrystalline sample of 1,4-^{13}C-1,2-^{15}N-glycylglycine hydrochloride monohydrate was synthesized and kindly provided by Raul Zambrano of Prof. P. Landsbury's group at MIT, and was also recrystallized from deionized water with ten-fold dilution in natural abundance material and packed into a 7 mm sapphire rotor (Doty Scientific, Columbia, SC) for magic angle spinning. Dilution of the labeled material minimizes the influence of intermolecular couplings on the experimental results.

NMR Experiments. In both the glycine and glycylglycine experiments, the compensated sequence in Figure (5-2) was applied with sampling every twelve rotor cycles. The glycine experiment was carried out at 4000 ± 3 Hz spinning frequency, and the glycylglycine trajectories at 3300 ± 5 Hz, using a

7 mm double bearing spinner from Doty Scientific. In the two spin glycine experiments, the pulse lengths employed were 3.3 μs 90° for ^{1}H, 14.0 μs 180° for ^{13}C, and 17.6 μs 180° for ^{15}N. However, in order to avoid signal losses from insufficient proton decoupling, weaker pulses were employed on the dilute spins in the glycylglycine dephasing experiments: 3.6 μs 90° for ^{1}H, 20.4 μs 180° for ^{13}C, and 20.4 μs 180° for ^{15}N.

Numerical Simulations. The two spin δ-function simulations for 1-^{13}C-^{15}N-glycine include the decay of all two spin coherences relative to the S spin magnetization explicitly with the general computational approach described in the first chapter. The dipole-dipole coupling constant of -195 Hz with $\Gamma = 25$ Hz fits the data better than the crystal value of -200 Hz, implying an internuclear distance which is too long by 1%, i. e. 0.02 Å. Similar discrepancies have been observed in TEDOR [7, 31], and these have been attributed to thermal motions [32].

A three spin finite pulse simulation which does not include coherence decay is used for the glycylglycine experiment. With weak pulses, the CSA tensors of the NH and CO_2 nuclei influence the results slightly, and they are included in the calculations with reasonable estimates of all tensor orientations. Relative to CO_2, there are intermolecular interactions to NH_3 groups with interatomic separations: 5.44, 5.11, 5.00, 5.24, and 3.79 Å in the X-ray structure. Although they are only 10% populated with the ^{15}N label in this sample, they lead in principle to an approximately 127% additional dephasing at short times, where a second moment expansion is applicable [2]. The "corrected simulation" points simply involve this scaling of the extent of dipolar dephasing, giving a more realistic trajectory for the diluted sample. The degree of observed experimental decay at 21.8 ms is overestimated by 33% for the 5.41 Å distance, implying a 5% error in the interatomic

separation compared to the corrected simulation, although some portion of the dephasing is possibly from the larger coupling.

The simulation results are usually converged with approximately ≤ 5000 crystallite orientations and forty time points per rotor period.

Figure (5-5). Schematic diagram of the glycylglycine molecule with the relevant heteronuclear internuclear distances shown. The atoms marked with asterices indicate the ^{13}C and ^{15}N labeled nuclei in the sample.

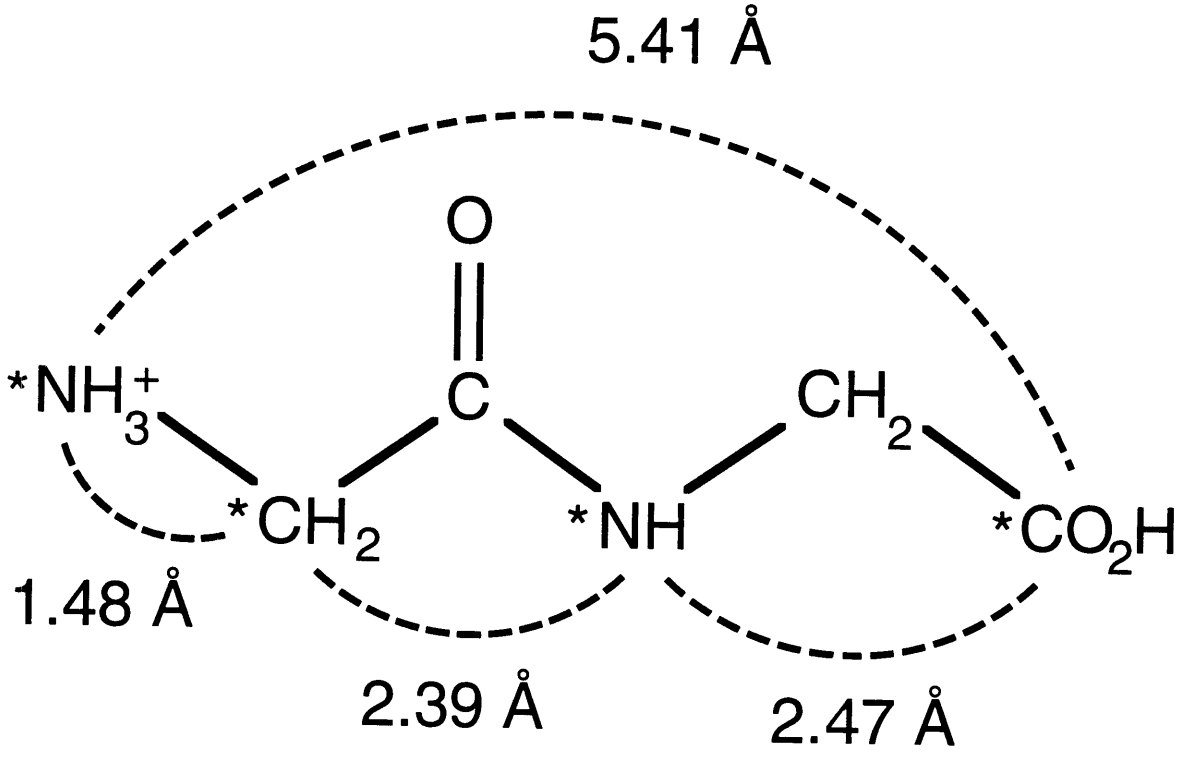
5.41 Å
O
*NH3+
C
CH2
*CH2
*NH
*CO2H
1.48 Å
2.39 Å
2.47 Å

Figure (5-6). Glycylglycine dephasing trajectories with the compensated FDR sequence: (a) $^{13}CO_2$ results, (b) $^{13}CH_2$ results. The selective dipolar recoupling to more weakly coupled resonances can be observed with frequency-resolved ^{15}N peaks. Squares indicate results obtained with the ^{15}N transmitter set on resonance with the $^{15}NH_3$ peak, which is shifted from the ^{15}NH resonance by 2.45 kHz. The circles indicate the corresponding results with frequency selection of the NH group. Open markers represent the simulated dephasing trajectories, which generally agree well the experimental data.

(a)

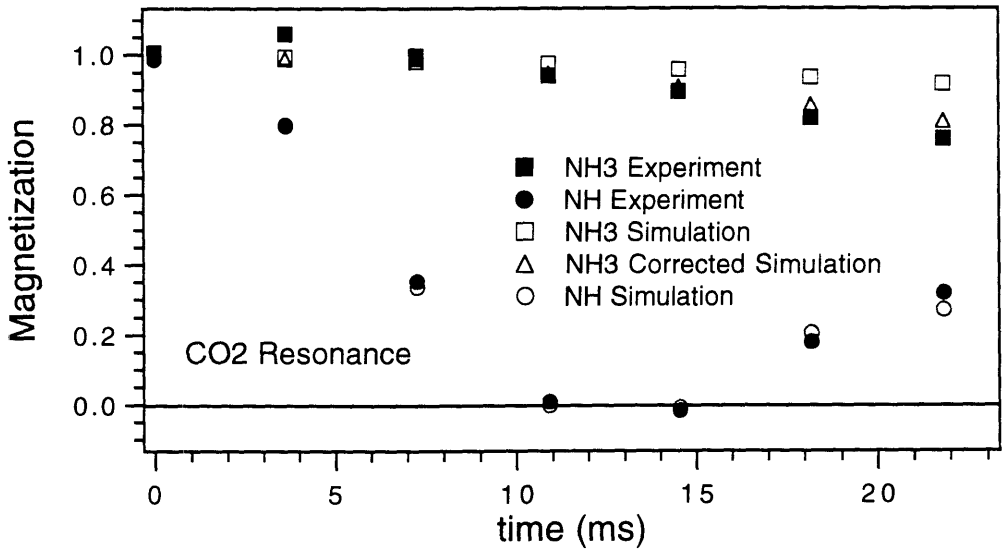
Magnetization
1.0
0.8
0.6
0.4
0.2
0.0
0
5
10
15
20
time (ms)
NH3 Experiment
NH Experiment
NH3 Simulation
NH3 Corrected Simulation
NH Simulation
CO2 Resonance

(b)

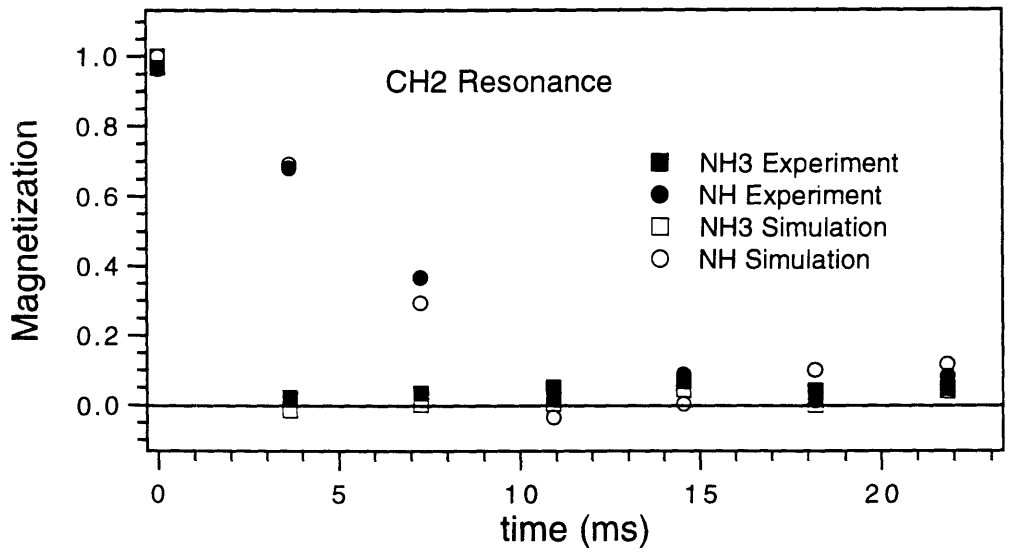
Magnetization
1.0
0.8
0.6
0.4
0.2
0.0
0
5
10
15
20
time (ms)
CH2 Resonance
NH3 Experiment
NH Experiment
NH3 Simulation
NH Simulation

IV. Application to Static Solids

The basic scheme for the frequency-selective multiple pulse analogue to the SEDOR experiment is shown in Figure (5-7). In MAS experiments, the pulses applied to the two RF channels must be out of phase with each other in order to hinder the rotational refocusing of the spin coherences with the greatest efficiency. In stark contrast, the opposite arrangement of the relative phases of the pulses is the most effective timing scheme in static (i. e. non-spinning) experiments. While an echo is formed with respect to the chemical shift evolution of the observed S spin, the simultaneous application of RF pulses to the I and S spins leads to dipolar dephasing [16].

In the static case, with the definition of the I spin shift from resonance δ_I, the time-independent internal spin Hamiltonian has the form:

$$H_{int} = \delta_I I_z + d_{IS}\left\{\frac{1-3\cos^2\theta}{2}\right\}\cdot 2I_z S_z \,, \tag{5-10}$$

where d_{IS} is the dipolar coupling constant and θ is the angle between the internuclear vector and the magnetic field. Again, the S spin chemical shift is neglected because it commutes at all times with the rest of the Hamiltonian during the application of π pulses, and in any case it is averaged out by the overall sequence, which yields an effective Hamiltonian closely paralleling that of Eq. (5-3):

$$\overline{H}^{(0)}_{int} = \frac{1}{\sqrt{2}}\delta_I I_{x'} + \frac{1}{\sqrt{2}} d_{IS}\left\{\frac{1-3\cos^2\theta}{2}\right\}\cdot 2I_{z'}S_z \,. \tag{5-11}$$

In this case, there is no special synchronization condition to fulfill. However, it is desirable to make the cycle time relatively short compared to the inverse of the size the dipolar interaction in order to maximize the validity of the AHT approximation used to derive Eq. (5-11). In the static application as well, dipolar dephasing occurs at the harmonic conditions $\delta_I = 2n\nu_C$, with the definition of the cycling rate $\nu_C = 1/\tau_C$, but this feature is minimized with the choice of a sufficiently short τ_C. On the other hand, the accumulation of finite pulse effects places practical restrictions on τ_C, since the RF duty cycle (which is the fraction of time during which RF power is applied) increases with shorter τ_C.

Although the approach introduced here is quite generally applicable to systems where the I and S spin systems have relatively narrow linewidths, the example discussed here involves an inhomogeneously broadened two spin system, namely, the ^{13}C-^{15}N spin pair in the peptide bond of glycylglycine. In Figure (5-8), the plane of the peptide bond is illustrated with the orientations of the σ_{11} and σ_{22} directions of the principal axis system (PAS) of the ^{13}C nucleus, whose transverse magnetization is observed in the experiment. These axes lie in the plane with the σ_{33} direction oriented in the perpendicular direction. For the ^{15}N spin, the σ_{11} and σ_{22} directions are nearly degenerate and quite difficult to resolve. However, the σ_{33} direction of the ^{15}N CSA tensor and the orientation of the ^{13}C tensor in the molecular reference frame are known from single crystal studies [33, 34].

In many cases, however, the relationship between the CSA and molecular frames cannot be measured directly because of the unavailability of large single crystals. Still, general principles have been developed based on numerous single crystal studies which have established the probable relationship between the CSA tensor and its local electronic environment in

many cases [20, 24]. The most likely orientations of several other carbonyl tensors in peptide bonds have been determined by correlating them to the ^{13}C-^{15}N internuclear vector through the study of static powder spectra. These NMR spectra manifest both the ^{13}C CSA interaction and the ^{13}C-^{15}N dipole-dipole coupling [35]. Further information about molecular structure can be obtained via correlation of the CSA tensors of both spins. For example, with the assumption that the CSA tensors are determined by their local electronic environments, the relative orientation of the ^{13}C and ^{15}N principal axis systems reflects the conformation of the peptide bond.

In a disordered system such as a polycrystalline sample, all possible molecular orientations are represented, and the chemical shift spectrum of the ^{15}N resonance exhibits a broad inhomogeneous lineshape. In Figure (5-9), simulated powder spectra of glycylglycine are shown with and without the dipole-dipole coupling to the ^{13}C spin. In the frequency-selective SEDOR experiment, the transmitter frequency is placed in the neighborhood of the spectrum corresponding to orientations where the σ_{33} direction of the ^{15}N CSA points along the magnetic field. At sufficiently long times, dipolar dephasing proceeds preferentially in portions of the ^{13}C CSA lineshape corresponding to tensor orientations which are in turn correlated with the selected region of the ^{15}N CSA. Although the strength of the dipolar coupling, which is also orientation-dependent, plays an important role in the dephasing trajectory, the behavior at long times (i. e. greater than the inverse of dipolar coupling constant) is dominated by the frequency offset effect. The net result is that the ^{13}C lineshape after dephasing sensitively reflects the relative orientations of the ^{13}C and ^{15}N CSA tensors.

In Figure (5-10), this effect is demonstrated. Since the σ_{33} direction of the ^{15}N PAS lies between the σ_{11} and σ_{22} directions of the ^{13}C CSA tensor,

spectral intensity develops selectively in the ^{13}C dephasing difference NMR spectrum in the corresponding region. The difference spectrum between the static echo signal with and without the application of pulses to the ^{15}N channel also exhibits limited amplitude near σ_{33}. This intensity, however, arises from the harmonic dephasing effect. Since the dipolar evolution is unquenched at all ^{15}N frequencies which are multiples of 5 kHz (i. e. twice the cycling rate of the pulse sequence), dephasing also occurs near σ_{33} to a limited degree. Simulations predict a reduction of dephasing in this region with a faster sequence. Although an uncompensated pulse scheme is applied in this experiment and the signal to noise ratio is quite poor, the difference lineshape agrees reasonably well with the simulation. More generally, numerical simulations reveal that the details of the powder difference lineshape are highly sensitive to small changes in the relative tensor orientations.

Experimental Techniques. The polycrystalline sample of 3-^{13}C-^{15}NH-glycylglycine hydrochloride monohydrate, labeled at the peptide bond, is diluted to 10% in natural abundance material. This experiment was carried out at 317 MHz for protons using an home-built triple resonance probe tuned to a single coil. The $\pi/2$ pulse lengths were 6.0 μs for ^{1}H, 13.3 μs for ^{13}C, and 12.7 μs for ^{15}N. The ^{13}C π pulses were phase-alternated according to the *XY*-16 scheme. The total dephasing time is 3.2 ms (>> longer than the inverse of 1310 Hz, the dipolar coupling constant, which corresponds to an internuclear separation of 1.33 Å [29]) with $\tau_C = 400\ \mu s$.

Lineshape Simulations. The lineshape simulations consist of the exact propagation of the ^{13}C magnetization in the two spin system for the 3.2 ms mixing period with finite pulses. Because of the broad character of the inhomogeneous lineshapes, a total of 500,000 crystallite orientations are

included in the calculations, and 500 Hz of Lorenztian line-broadening is applied to the results for ^{13}C and 250 Hz to the ^{15}N simulations. All of the CSA and dipole-dipole orientational parameters are available from the literature [33, 34]: the $(\sigma_{11}, \sigma_{22}, \sigma_{33})$ principal values of the ^{13}C CSA tensor are $(-115.6, -48.6, +40.6)$ ppm with respect to benzene, and $(+33.0, +43.6, +188.6)$ ppm for the ^{15}N tensor relative to saturated aqueous $^{15}NH_4Cl$ solution.

Figure (5-7). Basic pulse sequence for the frequency-selective dipolar dephasing experiment in non-spinning samples. The spin echo signal of the observed S spins (e. g. ^{13}C) dephases under the the influence of pairs of $\pi/2$ pulses applied to non-observed I spins (e. g. ^{15}N), but here the pulses are applied simultaneously. Although only the dilute spin channels are shown, cross polarization and proton decoupling are also applied in the experiment discussed here, so a triple resonance probe is again required. The pulse cycle time is twice the separation period between application of the pulses: $\tau_C = 2\tau_p$. Harmonic recoupling occurs when $2\pi\delta_I = 2\pi n$, which implies $\delta_I = 2n\nu_C$.

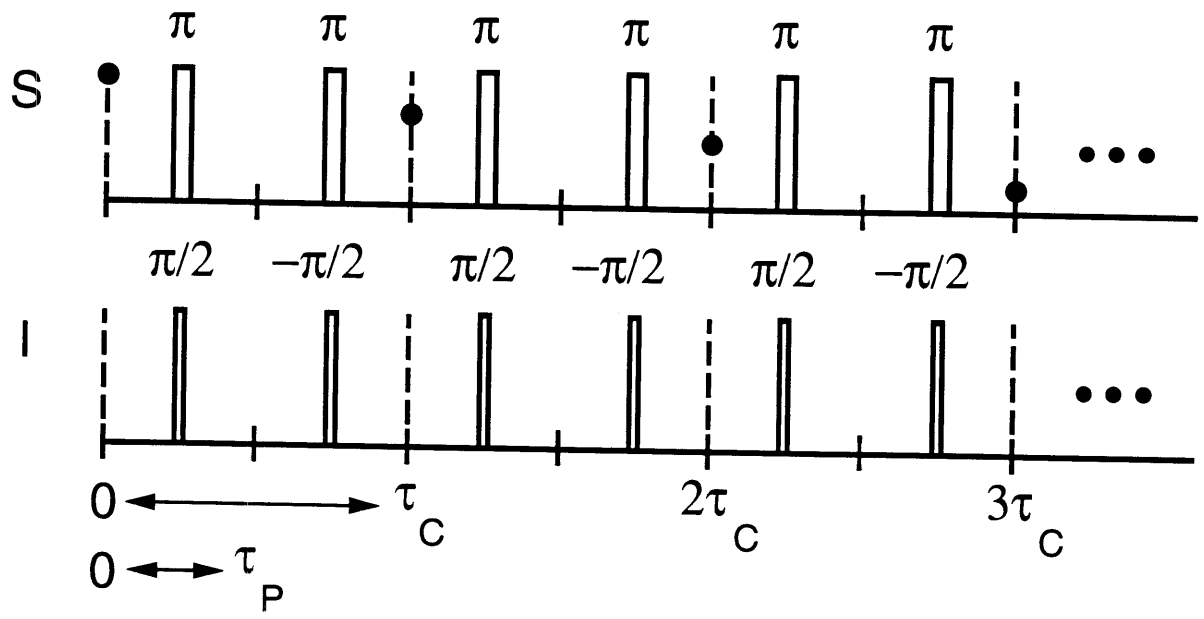
S
π
π
π
π
π
π
π/2
−π/2
π/2
−π/2
π/2
−π/2
I
0
τ C
2τ C
3τ C
0
τ P

Figure (5-8). Schematic diagram of the peptide bond in glycylglycine where the directions of the CSA directions of the ^{13}C and ^{15}N nuclei in the plane are illustrated. The σ_{33} direction of the ^{13}C tensor is close to perpendicular to the planar peptide bond, but the σ_{11} and σ_{22} directions of the ^{15}N tensor are not resolved because of their near degeneracy.

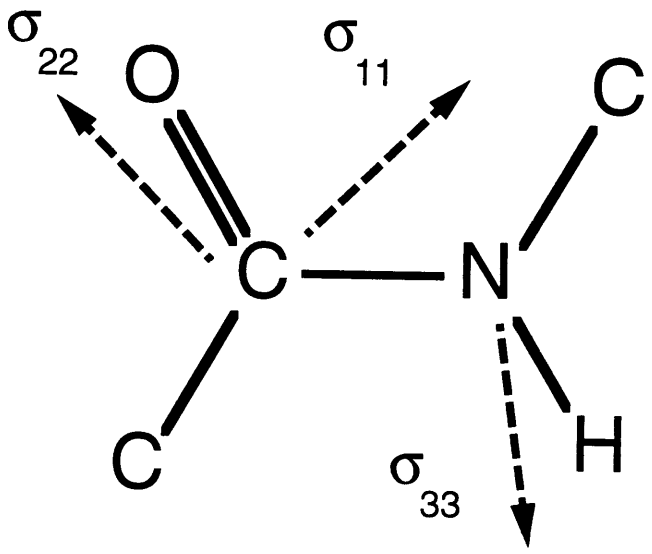
σ22
O
σ11
C
C
N
C
H
σ33

Figure (5-9). Lineshape simulations of the (a) ^{13}C and (b) ^{15}N NMR spectra of polycrystalline glycylglycine selectively labeled at the peptide bond. Because the ^{15}N CSA interaction has a narrower inhomogeneous distribution averaged over the powder sample, the heteronuclear dipole-dipole coupling has a larger influence on the ^{15}N lineshape than on the ^{13}C spectrum. The ^{15}N lineshape also exhibits near axial symmetry arising from the approximate degeneracy of the σ_{11} and σ_{22} directions of its chemical shift tensor.

(a)

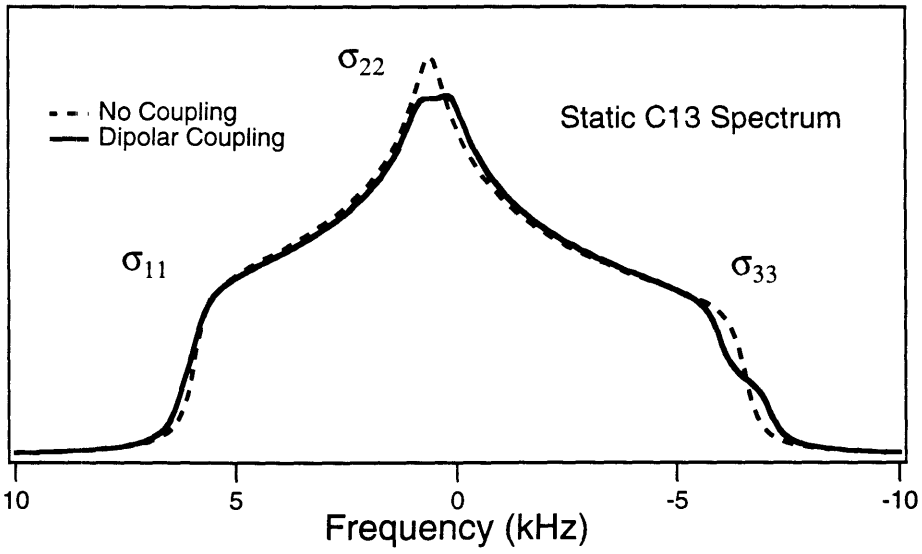
σ22
No Coupling
Dipolar Coupling
Static C13 Spectrum
σ11
σ33
10
5
0
-5
-10
Frequency (kHz)

(b)

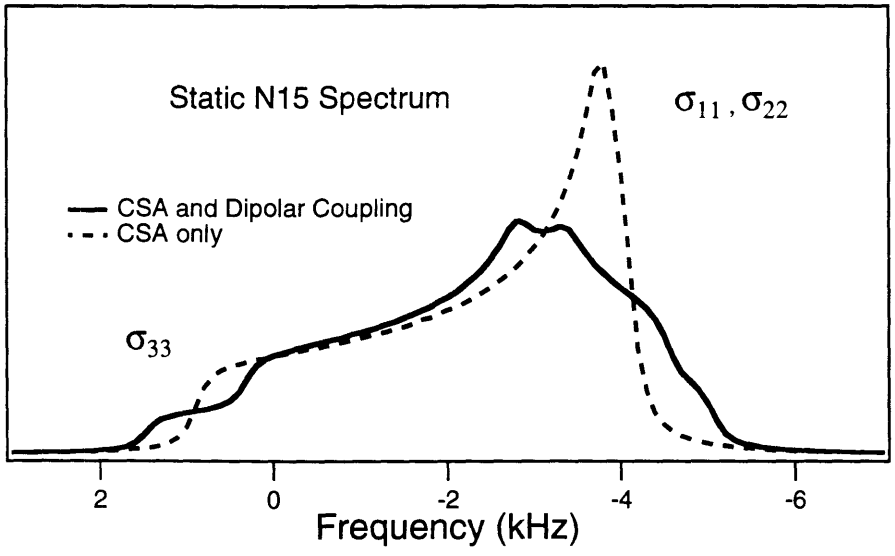
Static N15 Spectrum
σ11 , σ22
CSA and Dipolar Coupling
CSA only
σ33
2
0
-2
-4
-6
Frequency (kHz)

Figure (5-10). Experimental and simulated dephasing difference lineshape of ^{13}C after 3.2 ms mixing with the frequency-selective sequence applied at the ^{15}N frequency corresponding to its σ_{33} CSA orientation. The experimental spectrum is scaled to a similar amplitude as the simulated lineshape, and the simulated static ^{13}C spectrum without dephasing is also provided for comparison. Dipolar dephasing is selectively enhanced in the region between σ_{11} and σ_{22} of the ^{13}C CSA tensor and likewise inhibited between σ_{22} and σ_{33}.

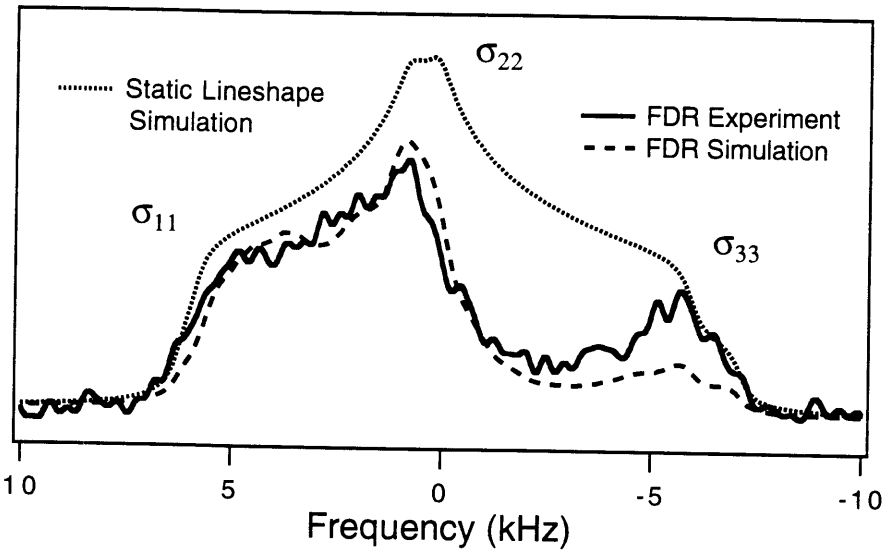
Static Lineshape Simulation
FDR Experiment
FDR Simulation
σ22
σ11
σ33
10
5
0
-5
-10
Frequency (kHz)

V. Conclusion

In cases where frequency-selectivity is desirable, the approach described here is a useful complement to REDOR and SEDOR experiments. One application of frequency-selective recoupling is the simultaneous measurement of internuclear distances between an observed spin and several non-observed spins in samples with multiple isotope labels. A related possibility is the de-selection of unwanted dipolar couplings arising from the natural abundance background in REDOR experiments [2, 12]. A second application, demonstrated here with a static sample, is the observation of the heteronuclear coupling in a spin pair with the selection of one portion of an inhomogeneous lineshape. For application to very broad lineshapes, selective SEDOR experiments have already been performed with weak refocusing pulses on the non-observed spin [36]. Although the correlation of frequency and dipolar coupling strength is also possible using two-dimensional techniques in the case of a spin pair, the multiple pulse approach is one-dimensional [37] and therefore provides an efficient means of obtaining information selectively in systems exhibiting a poor signal to noise ratio. In addition, since the FDR approach is based upon an Average Hamiltonian argument, it is straightforwardly applicable to heteronuclear coherence transfer methods such as TEDOR [7, 31].

In the heteronuclear dephasing experiments discussed here (couplings ≥ 200 Hz), the influence of finite pulse widths on the observed trajectories is quite small with RF fields ≥ 30 kHz, and calculations based on δ-function pulses are often sufficient for REDOR and the frequency-selective sequences. Furthermore, in the case of REDOR experiments, since the AHT approach is exact with δ-function pulses [1], the universal form of the dephasing curve

obtained from an isotropic distribution of internuclear vector orientations [2, 11] is usually sufficient. However, it appears that differences in the effective rates of decay between the single spin and the two spin coherences can have a significant influence on the observed dephasing trajectories. A single differential decay parameter has been introduced here in order to interpret the frequency-selective results for a variety of resonance offsets.

In the multiple spin case, experiments with distinct resonances in both the observed and non-observed spin systems provide a route to several internuclear distances within a single sample. For example, in the case of a system containing two S spins and two I spins, a combination of frequency-selective heteronuclear measurements, along with separate homonuclear recoupling experiments, could yield as many as six distance constraints to aid in the determination of molecular structure. To date, most recoupling experiments have involved the accurate measurement of the dipole-dipole coupling in a single spin pair [1]. In future years, however, it seems likely that frequency-selective approaches, including the experiment presented here and the rotational resonance method, will be important means of obtaining a larger number of internuclear distances from the same sample, which will lead to the much more efficient acquisition of structural information from solid state NMR experiments.

References for Chapter 5.

[1] A. E. Bennett, R. G. Griffin, and S. Vega, NMR Basic Principles and Progress **33**, 1 (1994).

[2] Y. Pan, T. Gullion, and J. Schaefer, J. Mag. Res. **90**, 330 (1990).

[3] D. P. Raleigh, F. Creuzet, S. K. Das Gupta, M. H. Levitt, and R. G. Griffin, J. Am. Chem. Soc. **111**, 4502 (1989).

[4] A. E. Bennett, J. H. Ok, R. G. Griffin, and S. Vega, J. Chem. Phys. **96**, 8624 (1992).

[5] N. C. Nielsen, F. Creuzet, R. G. Griffin, and M. H. Levitt, J. Chem. Phys. **96**, 5668 (1992).

[6] R. Tycko and S. O. Smith, J. Chem. Phys. **98**, 932 (1992).

[7] A. Hing, S. Vega, and J. Schaefer, J. Mag. Res. **96**, 205 (1992).

[8] D. P. Raleigh, M. H. Levitt, and R. G. Griffin, Chem. Phys. Lett. **146**, 71 (1988).

[9] M. H. Levitt, D. P. Raleigh, F. Creuzet, and R. G. Griffin, J. Chem. Phys. **92**, 6347 (1990).

[10] T. Gullion and J. Schaefer, J. Mag. Res. **81**, 196 (1989).

[11] T. Gullion and J. Schaefer, Adv. Mag. Res. **13**, 58 (1989).

[12] A. M. Christensen and J. Schaefer, Biochem. **32**, 2868 (1993).

[13] R. Tycko, G. Dabbagh, S. R. Kurtz, and J. P. Goral, Phys. Rev. B **45**, 13452 (1992).

[14] A. E. Bennett, L. R. Becerra, and R. G. Griffin, J. Chem. Phys. **100**, 812 (1994).

[15] M. Emshwiller, E. L. Hahn, and D. E. Kaplan, Phys. Rev. **118**, 414 (1960).

[16] C. P. Slichter, *Principles of Magnetic Resonance* (Springer-Verlag,

Berlin, 1990).

[17] T. Gullion, D. B. Baker, and M. S. Conradi, J. Mag. Res. **89**, 479 (1990).

[18] E. T. Olejniczak, S. Vega, and R. G. Griffin, J. Chem. Phys. **81**, 4804 (1984).

[19] U. Haeberlen and J. S. Waugh, Phys. Rev. **175**, 453 (1968).

[20] U. Haeberlen, *High Resolution NMR in Solids: Selective Averaging* (Academic Press, New York, 1976).

[21] W.-K. Rhim, D. D. Elleman, L. B. Schreiber, and R. W. Vaughan, J. Chem. Phys. **60**, 4595 (1974).

[22] M. Mehring and J. S. Waugh, Rev. Sci. Inst. **43**, 649 (1972).

[23] T. M. Barbara, J. F. Martin, and J. G. Wurl, J. Mag. Res. **93**, 497 (1991).

[24] M. Mehring, *Principles of High Resolution NMR in Solids* (Springer-Verlag, Berlin, 1983).

[25] A. Schmidt and S. Vega, Isr. J. Chem. **32**, 215 (1992).

[26] P. G. Jönsson and Å. Kvick, Acta. Cryst. B **28**, 1827 (1972).

[27] S. M. Holl, G. R. Marshall, D. D. Beusen, K. Kociolek, A. S. Redlinski, M. T. Leplawy, R. A. McKay, S. Vega, and J. Schaefer, J. Am. Chem. Soc. **114**, 4830 (1992).

[28] G. R. Marshall, D. D. Beusen, K. Kociolek, A. S. Redlinski, M. T. Leplawy, Y. Pan, and J. Schaefer, J. Am. Chem. Soc. **112**, 963 (1990).

[29] R. Parthasarathy, Acta. Cryst. B **25**, 509 (1969).

[30] T. F. Koetzle, W. C. Hamilton, and R. Parthasarathy, Acta. Cryst. B **28**, 2083 (1972).

[31] A. Hing, S. Vega, and J. Schaefer, J. Mag. Res. A **103**, 151 (1993).

[32] E. R. H. van Eck and W. S. Veeman, J. Mag. Res. A **109**, 250 (1994).

[33] R. E. Stark, L. W. Jelinski, D. J. Ruben, D. A. Torchia, and R. G. Griffin, J. Mag. Res. **55**, 266 (1983).

[34] G. S. Harbison, L. W. Jelinski, R. E. Stark, D. A. Torchia, J. Herzfeld, and R. G. Griffin, J. Mag. Res. **60**, 79 (1984).

[35] T. G. Oas, C. J. Hartzell, T. J. McMahon, G. P. Drobny, and F. W. Dahlquist, J. Am. Chem. Soc. **109**, 5956 (1987).

[36] Z. Wang, J.-P. Ansermet, C. P. Slichter, and J. H. Sinfelt, J. Chem. Soc. Faraday Trans. **84**, 3785 (1988).

[37] D. P. Weliky, G. Dabbagh, and R. Tycko, J. Mag. Res. A **104**, 10 (1993).

Chapter 6.

Improved Heteronuclear Decoupling in Rotating Solids

I. Introduction

In the presence of a sufficiently strong proton decoupling field, the resonance offset effect is the principal mechanism of ^{1}H line-broadening in solid state magic angle spinning NMR spectra of dilute spins, such as ^{13}C, ^{15}N, and ^{31}P [1]. This is the case even though the ^{1}H offsets from exact resonance are small compared to any reasonable RF field amplitude. In rotating solids, the frequency shift of the decoupling field from resonance originates from two sources. One is the dispersion of the isotropic chemical shifts in the proton spectrum ($\leq$ 10 ppm), and this contribution represents the fundamental difficulty encountered in solution NMR spectroscopy. However, a crystallite in a powdered sample which is spinning about the magic angle also experiences a range of proton frequencies which are sampled over the course of a rotor cycle. As a consequence, it is impossible to set the ^{1}H RF transmitter precisely "on resonance" even for an isolated proton [2].

In addition to resonance offsets, a particularly important consideration in multiple pulse decoupling is the necessity of minimizing undesirable "cycling sideband" intensities that arise from the application of an RF field which is not large relative to the spin-spin couplings in the system [3]. Specifically, under conditions of low power, undesirable artifactual spectral lines of low intensity appear along the baseline in the NMR spectrum. The cycling sideband problem is exacerbated further by destructive interference between the pulse sequence and the amplitude modulation of the interactions imposed by sample rotation in MAS experiments. These effects are particularly pronounced in the case of relatively long decoupling sequences based on composite pulses, such as the COMARO-2 sequence designed for liquid crystal applications [4-6], as well as many other sequences employed in

solution spectroscopy [7-9], such as WALTZ-16 [10]. In the limit of high power relative to the spin-spin coupling, these sequences retain their decoupling efficiency even when the resonance offset is as large as a significant fraction of the RF field strength; for example, in the case of COMARO-2, the bandwidth is approximately one half of the RF amplitude in frequency units [6]. Theoretical efforts have focused on increasing resonance offset compensation in order to facilitate the use of lower RF field strengths and thereby minimize sample heating in solution applications [8, 11, 12]. The development of these broad-banded methods has been reviewed by Shaka and Keeler [3].

However, with the typical proton RF field amplitudes (60-100 kHz) which are employed in MAS experiments, the cycle time of many composite pulse sequences becomes comparable to the rotor period, leading to degradation of the decoupling efficiency. Even without the complicating factor of sample spinning, the association between the cycling sideband problem and increasing resonance offset compensation is an important consideration in the development of ultra-high bandwidth decoupling techniques [9, 13]. Fortunately, the resonance offset effect is relatively small under ordinary MAS conditions, since large decoupling fields (greater than 40 kHz) are necessary to suppress the dipolar couplings between ^{1}H and ^{13}C nuclei, which are in the range of 10-40 kHz for directly bonded spins. A method with smaller bandwidth enhancement than the composite pulse approaches can therefore lead to significant improvement in the observed linewidths. A general approach which compensates for small resonance offsets, but which is very economical with the available decoupling power, is transverse phase modulation in the rotating frame. This approach was first introduced by Anderson and co-workers [14, 15], but was later abandoned

because its range of resonance offset compensation is insufficent for modern solution NMR applications.

More recently, pronounced difficulties in applying proton decoupling to paramagnetic samples, where protons experience a large dispersion of inhomogeneous local magnetic fields, has stimulated great interest in the development of relatively simple excitations which reduce the resonance offset problem in MAS experiments [16-18]. In these cases, the line-broadening can be so serious that even relatively inefficient sequences often yield significant improvements in observed linewidths over CW decoupling. Likewise, in the case of diamagnetic solids, interest in the decoupling problem has arisen from the deterioriating quality of CW decoupling observed in the regime of high spinning speeds [19-21], as well as the increasing significance of the resonance offset effect in solid state experiments which are performed in ever increasing magnetic fields [22]. For the most part, the line-broadening observed at high spinning speeds appears to be attributable to the reduction of the homonuclear proton linewidth under fast spinning [19, 23], which attenuates the favorable line-narrowing influence, or "self-decoupling" effect, exerted by the homonuclear couplings among protons [24, 25].

The linewidths obtained in diamagnetic solids with CW decoupling can be improved when the influence of small resonance offsets is compensated while at the same time the available decoupling power is applied with the greatest possible efficiency. The development of undesirable dynamical artifacts associated with sample spinning and broad-banded sequences must be suppressed. Since these objectives are somewhat conflicting, it appears that the ideal decoupling sequence should provide a limited degree of offset compensation, but no more than necessary, and simultaneously perform well

with large heteronuclear couplings under sample rotation. An additional consideration in designing solid state decoupling sequences is the role of homonuclear couplings among protons. The decoupling pulse sequence must perform well in the presence of a network of strong homonuclear couplings, and in order to compete with the results obtained with CW decoupling – whose performance benefits from the "self-decoupling" effect provided by homonuclear interactions [24, 25] – the ideal sequence should also exploit this line-narrowing influence, rather than eliminate it via coherent averaging.

In order to improve upon CW decoupling, a flexible implementation of the coherent phase modulation approach involving two pulses is introduced here, which generally requires non-orthogonal phase shifts and approximates the type of excitation first introduced by Anderson and Freeman [14] and more recently analyzed by Shaka and Keeler [3]. This approach improves the dipolar linewidths of ordinary diamagnetic solids in powdered samples at high magnetic field, and it performs well up to a spinning frequency of at least 12 kHz. Related multiple-frequency excitation techniques have already been exhibited improvements in the MAS spectra of paramagnetic samples [18]. The two pulse phase modulation (TPPM) approach presented here reduces the degradation of CW decoupling in ^{13}C NMR spectra from resonance offsets present in the system, including the ^{1}H chemical shift anisotropy, as well as other fields which resemble the Zeeman term in the spin Hamiltonian, such as magnetic susceptibility fields and heteronuclear couplings to additional nuclei, such ^{15}N and ^{14}N [1, 2].

In general, these local fields are anisotropic and oscillatory under mechanical rotation. In this chapter, several theoretical aspects of phase modulation decoupling under strong interactions and MAS are addressed,

including the impact of RF inhomogeneity, and calculations of the dynamical evolution of a model crystallite of the CH_2 group are presented in order to illustrate the role of oscillatory interactions. Experimental MAS spectra of several polycrystalline model compounds demonstrate that the linewidth improvements are quite general, even in compounds with large homonuclear ^1H-^1H interactions. For solid state experiments, where the greatest difficulties have been the poor spectral resolution and signal-to-noise ratio [25], the improved ^{13}C lineshapes presented here provide significant enhancements in both resolution and sensitivity.

II. Experimental Results with TPPM Decoupling

The TPPM decoupling sequence consists of the following: application of RF pulses of length τ_p alternating between two phases separated by an angle ϕ. In Figure (6-1), the basic sequences is illustrated within the usual context of a double resonance CPMAS experiment.

All of the spectra presented in this chapter were acquired at room temperature on an home-built solid state NMR spectrometer operating at 397 MHz for protons. The transmitter, provided by Dr. David Ruben and co-workers, has digital phase, amplitude, and frequency-switching capabilities, with a maximum 50 ns transient switching period between the pulses, during which power was applied continuously. In these experiments, windowless application of the pulse sequence is essential. The double resonance probe is also home-built and employs a commercially available 5 mm double bearing spinner assembly (Doty Scientific, Columbia, SC). The RF inhomogeneity experienced by the sample is in the range of 5% to 10%.

Figure (6-2) demonstrates the improvement which is obtained in the case of polycrystalline tyrosine hydrochloride monohydrate spinning at 10 kHz with an RF field amplitude of 75.8 kHz. The linewidths of the α- (85 to 52 Hz) and β-^{13}C (120 to 48 Hz) resonances exhibit especially pronounced narrowing under the phase-modulated sequence. The transmitter frequency is optimized with respect to the lineshape of the α-^{13}C resonance (second centerband line from the left). In the region of the ring carbon resonances, the spectral lines corresponding to the monoprotonated carbons are improved to a lesser degree, but their linewidths are already relatively narrow under CW decoupling (i. e. 55-67 Hz). In fact, even the linewidths of the unprotonated resonances are reduced significantly. The CW decoupling full widths at half maximum (FWHM), which range from 55-120 Hz, are all converged by application of the TPPM sequence to a minimum of 50 ± 5 Hz.

Figure (6-3) demonstrates striking improvement in the resolution of the two ^{13}C resonances in calcium formate, which arise from the non-equivalence of the two formate ions in the crystal structure. The spectral lines are separated by 0.8 parts per million (ppm) [26], i. e. 80 Hz in this experiment. In this more unusual case, CW decoupling is relatively inefficient because of the weak intermolecular couplings among the protons in calcium formate, which provide little assistance in quenching the heteronuclear interaction via the "self-decoupling" effect. As a consequence, the ^{13}C linewidths degrade more quickly than usual with increasing spinning frequency, and compensated methods are therefore of particular utility. In fact, Tekely *et. al.* [19] have already shown that the low-frequency phase-inversion technique of Grutzner and Santini [27] leads to substantial improvements in the linewidths under similar conditions.

In general, there is some optimal combination of pulse length τ_p and total modulation angle ϕ to apply with the TPPM sequence, which depends on several factors, including the MAS frequency, the RF field strength, and the system under study. This dependence is pursued here as a function of spinning speed for the 4-CH_2 group in 1,4-^{13}C-2-^{15}N-glycylglycine hydrochloride monohydrate (ten-fold diluted in natural abundance material) with an RF field of 69.4 kHz (i. e. corresponding to a 90° pulse length of 3.6 μs). At 4 kHz spinning speed, Figure (6-4) illustrates the joint dependence of the FWHM on the pulse length and phase angle in a contour plot, which exhibits a stable global minimum in the ^{13}C linewidth of 60 Hz. At 8 kHz spinning speed, additional local minima are observed, but a stable global minimum persists. Similar trends are observed for the methylene resonance of ^{15}N-2-^{13}C-glycine. Figure (6-5) summarizes the enhancement in the optimized FWMH as a function of spinning speed at the slightly higher RF power level of 75.8 kHz. With empirical optimization, the pulse length τ_p is somewhat shorter than the flip angle π in these experiments, which is the approximate value expected with a small modulation angle ϕ.

The largest improvements are found at high and low spinning speeds, where CW decoupling performs with reduced efficiency.

Figure (6-1). Pulse sequence for the CPMAS experiment with the addition of phase modulation TPPM decoupling on the ^{1}H channel. A small hatched region of the decoupling period is expanded in order to illustrate the rapid alternation of the phase of the RF excitation between values $-\phi/2$ and $+\phi/2$ with overall period $2\tau_p$, which is repeated throughout the acquisition of the FID.

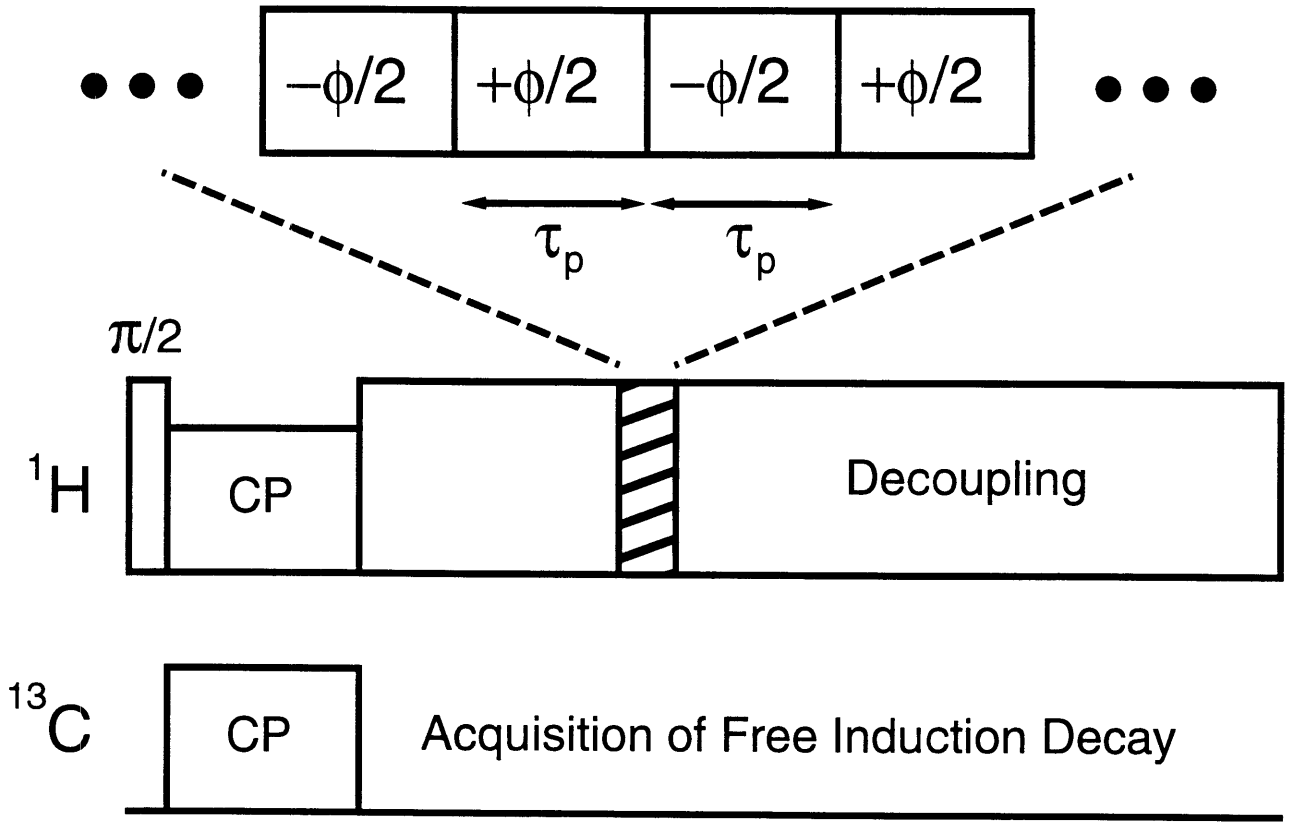
−ϕ/2
+ϕ/2
−ϕ/2
+ϕ/2
τp
τp
π/2
1H
CP
Decoupling
13C
CP
Acquisition of Free Induction Decay

Figure (6-2). CPMAS spectra of tyrosine hydrochloride monohydrate at 10 kHz spinning with a 75.8 kHz ^{1}H decoupling RF field (which corresponds to a 3.3 μs π/2 pulse length). The ^{1}H transmitter frequency is optimized for the α-^{13}C resonance, the second centerband line from the right. A comparison is given between the CW and TPPM results with the parameters $\phi = 15°$ and $\tau_p = 6.0\ \mu s$. From left to right, the nine centerband lines in the spectrum correspond to the O- (carbonyl), ζ, δ, δ', γ, ε, ε', δ, δ', α, and β-^{13}C resonances of the amino acid, respectively.

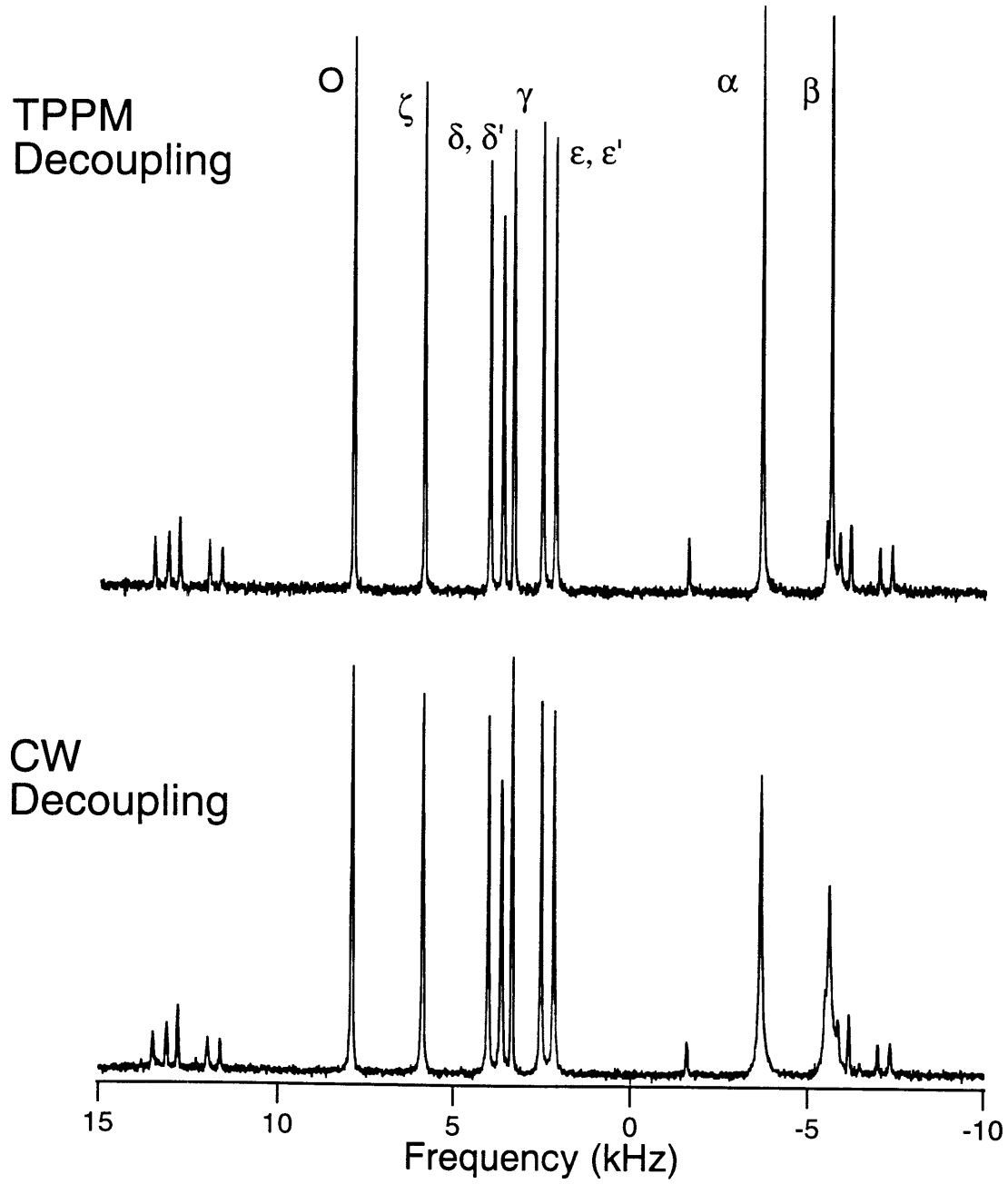
TPPM
Decoupling
O
ζ
δ, δ'
γ
ε, ε'
α
β
CW
Decoupling
15
10
5
0
-5
-10
Frequency (kHz)

Figure (6-3). The centerbands of the CPMAS spectra of calcium formate at 10.7 kHz spinning frequency with CW and TPPM decoupling obtained using the parameters: $\phi = 75°$, $\tau_p = 7.5\ \mu s$. An RF field strength of 62.5 kHz (4.0 μs π/2 pulse length) is applied. The non-equivalent formate ions are separated by 80 Hz in their centerband positions.

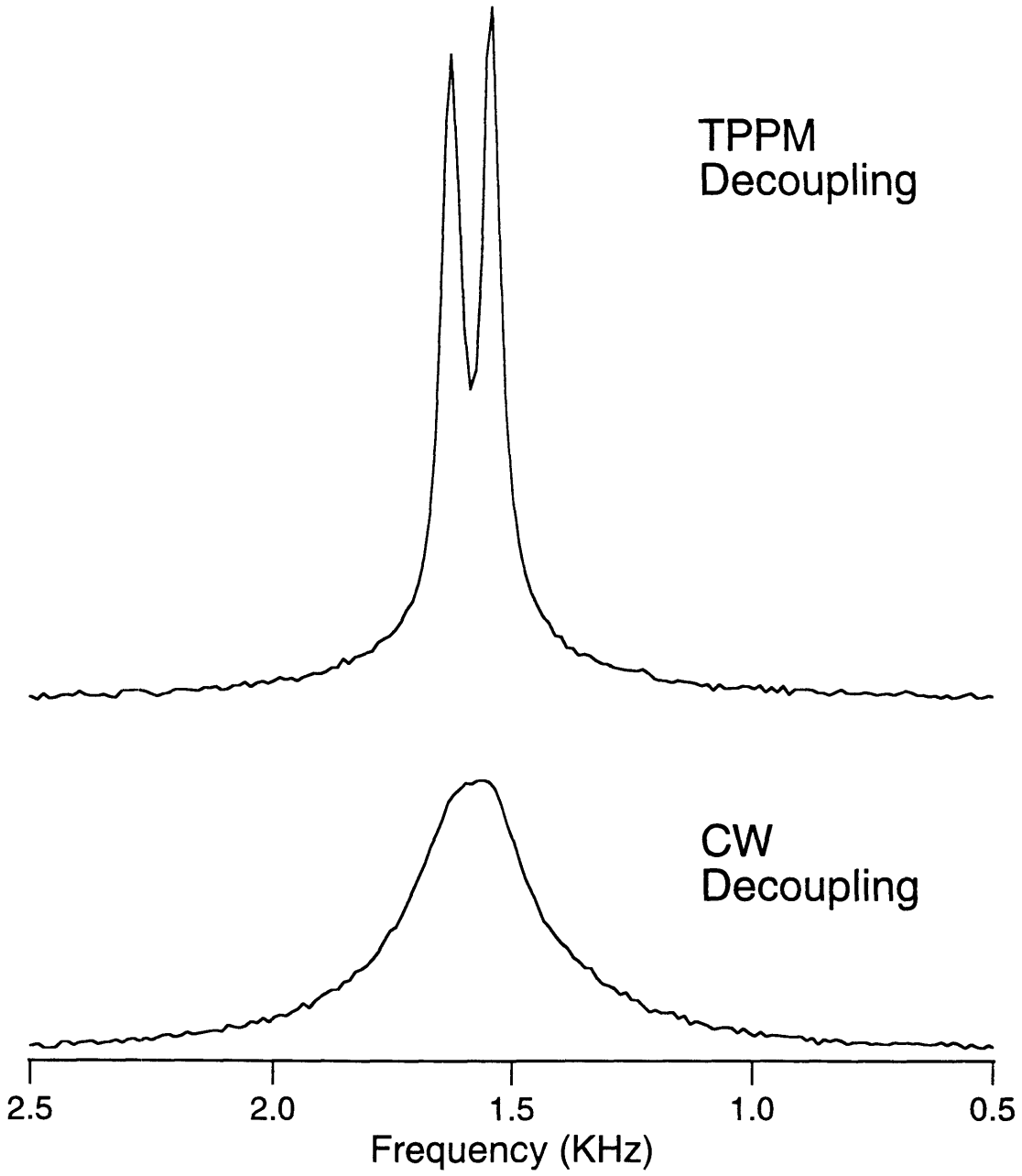
TPPM
Decoupling
CW
Decoupling
2.5
2.0
1.5
1.0
0.5
Frequency (KHz)

Figure (6-4). Contour plot of the linewidths (defined as the full width at half maximum in Hz) of the 4-CH_2 resonance of 1,4-^{13}C-4-^{15}N-glycylglycine hydrochloride monohydrate as a function of the pulse width (expressed in units of flip angle in degrees) and phase modulation angle (also in degrees) at 4 kHz spinning speed. The RF field strength is 69.4 kHz (3.6 μs $\pi/2$ pulse length).

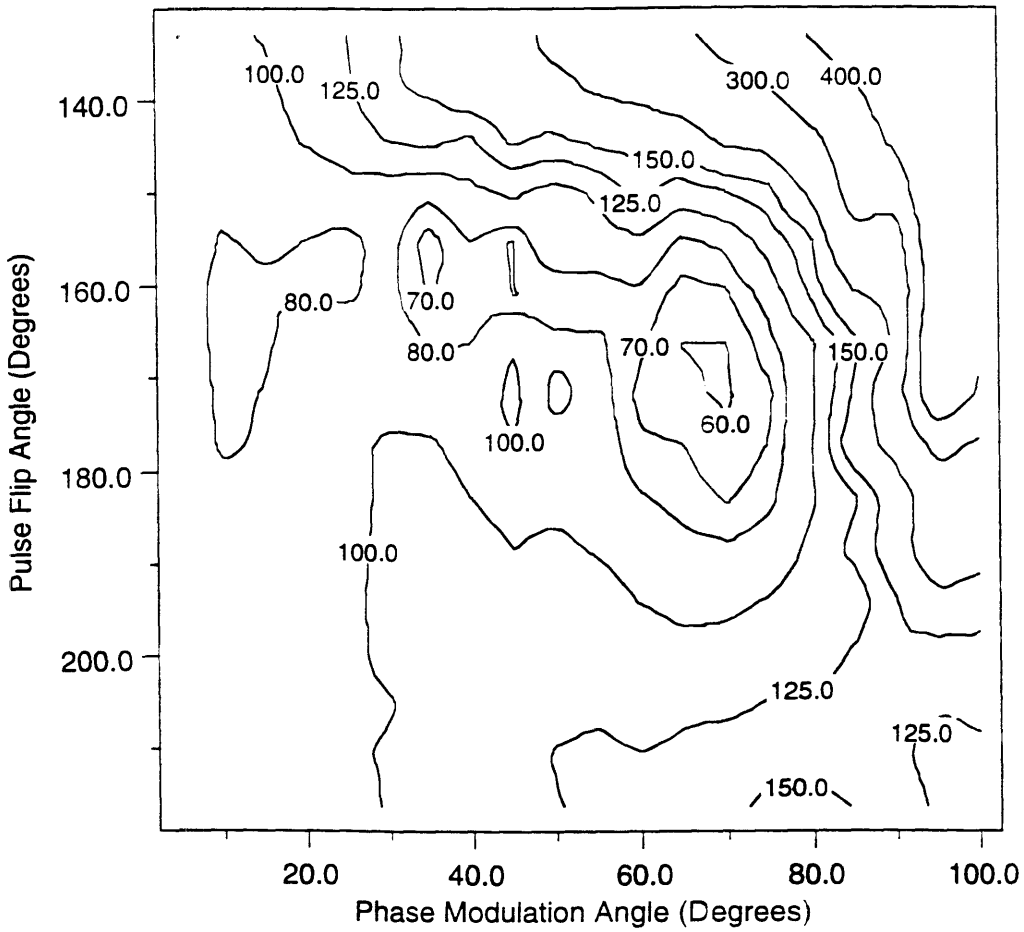
100.0
125.0
300.0
400.0
150.0
125.0
80.0
70.0
80.0
70.0
150.0
60.0
100.0
100.0
125.0
125.0
150.0
140.0
160.0
180.0
200.0
Pulse Flip Angle (Degrees)
20.0
40.0
60.0
80.0
100.0
Phase Modulation Angle (Degrees)

Figure (6-5). (a) Plot of the FWHM of the 4-CH_2 resonance of 1,4-^{13}C-4-^{15}N-glycylglycine hydrochloride monohydrate as a function of spinning frequency under CW and TPPM decoupling with optimized parameters. The RF field strength on the ^{1}H channel is 75.8 kHz. Line-broadening effects other than decoupling inefficiency lead to a linewidth of 35 ± 5 Hz. (b) The corresponding optimal pulse lengths (flip angle in degrees) and modulation angles (also in degrees) are shown as a function of spinning speed. Although the optimal flip angle corresponding to τ_p is only mildy dependent on the spinning speed, the phase angle ϕ has considerable spinning speed dependence.

(a)

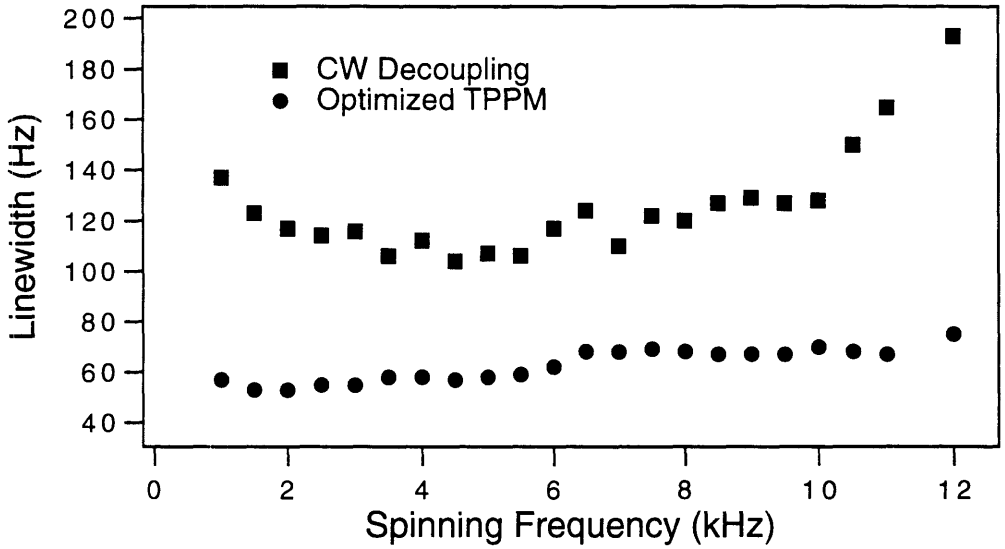
200
180
160
140
120
100
80
60
40
Linewidth (Hz)
CW Decoupling
Optimized TPPM
0
2
4
6
8
10
12
Spinning Frequency (kHz)

(b)

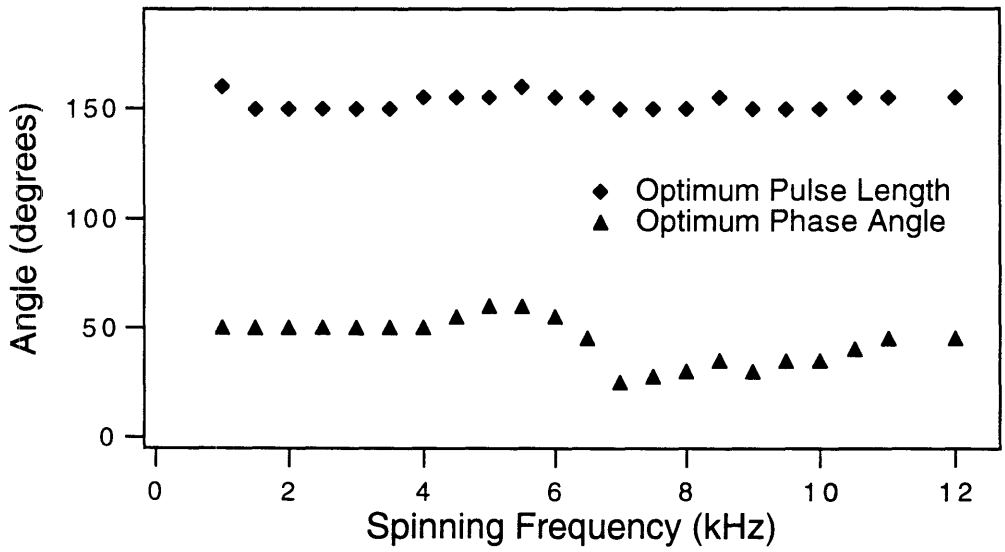
150
100
50
0
Angle (degrees)
Optimum Pulse Length
Optimum Phase Angle
0
2
4
6
8
10
12
Spinning Frequency (kHz)

III. Theory of Transverse Phase Modulation Decoupling

In the most general case, three complications arise in the dynamics of heteronuclear spin decoupling in MAS experiments. First, the decoupling field is typically less than an order of magnitude larger than the heteronuclear coupling to be suppressed in the case of ^{13}C atoms with directly bonded ^{1}H spins. Second, strong homonuclear dipolar interactions are present among the protons in the system, and these have profound effects on CW decoupling via the self-decoupling effect, as well as on the spin dynamics of multiple pulse decoupling. Lastly, when MAS is employed, the amplitude modulation of all internal interactions in the spin Hamiltonian must be considered explicitly.

Ordinarily, the dilute spins which are observed in MAS experiments are essentially independent while the protons form a coupled network. The appropriate Hamiltonian for a single rare spin experiencing chemical shift and heteronuclear interactions is the following:

$$H_{int}(t) = \delta_S(t)S_z + \sum_j D_j(t)\cdot 2S_z I_{zj} + \sum_j \delta_j(t) I_{zj} + \sum_{i<j} A_{ij}(t)\left\{2I_{zi}I_{zj} - I_{xi}I_{xj} - I_{yi}I_{yj}\right\}, \tag{6-1}$$

where S_α represents the α component of the angular momentum operator of the observed spin, and $I_{\alpha j}$ the angular momentum operators of the abundant spins j (i. e. usually ^{1}H, which are not observed but instead decoupled). Although the chemical shift $\delta_S(t)$ of the S spin generally represents the interaction of the greatest interest to the observer, it commutes with the rest

of the Hamiltonian of Eq. (6-1) and can therefore be omitted subsequently from consideration of the spin decoupling dynamics [11].

The parameters $\delta_j(t)$ in Eq. (6-1) represent the various inhomogeneous local fields experienced by the protons in MAS experiments. In typical diamagnetic solids, the local fields $\delta_j(t)$ are at most 5 kHz, say, with a 500 MHz magnetic field strength for protons. In contrast, the heteronuclear couplings $D_j(t)$ between directly bonded ^{13}C and ^{1}H nuclei are much larger, on the order of 10-40 kHz, and the strongest ^{1}H-^{1}H couplings $A_{ij}(t)$ are of similar magnitude. In all cases, the spatial prefactors are time-dependent because of sample spinning. The dipolar couplings are amplitude-modulated at ω_R and $2\omega_R$, where ω_R is the spinning frequency in angular units, with many possible relative phases among the various terms [28]. In general, the terms $\delta_j(t)$ also include a time-independent contribution, which defines the shift of the transmitter from resonance with proton j.

The two pulse phase modulation scheme contributes two additional terms to the rotating frame Hamiltonian:

$$H(t) = H_{\text{int}}(t) + \nu_{RF}\cos(\phi/2)I_x + \Phi(t)\nu_{RF}\sin(\phi/2)I_y\ , \qquad (6\text{-}2)$$

where $\Phi(t)$ is a square-wave function of unit amplitude which represents phase switching with angular frequency $\omega_p = 2\pi/2\tau_p$. Here I_α indicates the total α component of the I spin angular momentum. Only terms that are secular with respect to the dominant term $\nu_{RF}\cos(\phi/2)I_x$, which include the heteronuclear couplings and resonance offsets through first order, must be retained after averaging over the time period $1/\nu_{RF}\cos(\phi/2)$, in the limit of a strong decoupling field strength. With the assumption of small phase modulation angle ϕ, the term $\Phi(t)\nu_{RF}\sin(\phi/2)I_y$ represents a small

transverse excitation, and it is necessary to retain only the portion of it which is resonant with the dominant "spin lock" field $\nu_{RF}\cos(\phi/2)I_x$. The following result is obtained with the additional assumption of very slow spinning relative to the primary time scale of decoupling $1/\nu_{RF}\cos(\phi/2)$:

$$H_{eff}(t) = \nu_{RF}\cos(\phi/2)I_x + \frac{2}{\pi}\nu_{RF}\sin(\phi/2)\left\{\cos(\omega_p t)I_y + \sin(\omega_p t)I_z\right\}$$
$$+\sum_j \frac{1}{2\nu_{RF}\cos(\phi/2)}\left\{\delta_j^2(t) + D_j^2(t)\right\}I_{xj} + \sum_j \frac{1}{\nu_{RF}\cos(\phi/2)}\delta_j(t)D_j(t)\cdot 2S_z I_{xj} \quad (6\text{-}3)$$
$$-\frac{1}{2}\sum_{i<j} A_{ij}(t)\left\{2I_{xi}I_{xj} - I_{yi}I_{yj} - I_{zi}I_{zj}\right\}.$$

The separation of time scales which is assumed relative to the MAS modulation of the spatial prefactors amounts to an adiabatic assumption which is justified in the limit $\nu_{RF}\cos(\phi/2) >> 2\nu_R$.

The first term in Eq. (6-3) represents the dominant Zeeman-like field, which defines the direction along which "good quantum numbers" can be defined. In the second term, only the first Fourier coefficient of the small excitation transverse to I_x is retained, and the rotating wave which is far off resonance with the field along I_x is neglected. The third term represents a second order shift in the main field amplitude. The fourth and most important contribution to Eq. (6-3) corresponds to the scaled residual coupling between the dilute spin and the protons. Although this term in the spin Hamiltonian is linear in a small offset $\delta_j(t)$ from resonance, the homonuclear coupling contribution in the fifth term generates the well-known self-decoupling effect, which leads to a quadratic, rather than linear, dependence of the ^{13}C linewidth on the offset term $\delta_j(t)$ [25]. In order to obtain further linewidth reduction, a resonance condition with respect to the

dominant field, i. e. $\omega_p / 2\pi \approx \nu_{RF} \cos(\phi / 2)$, must be fulfilled. In practice, this condition indicates that τ_p should be set approximately to the π pulse length in the regime of small ϕ.

To calculate the effect of the second field on the effective heteronuclear coupling, a second rotating frame transformation is carried out in order to eliminate the time-dependence of the transverse field, in a way similar to the treatment discussed by Shaka and Keeler [3]. The residual spin interactions are evaluated to lowest order after averaging over a second period $1/\nu_{RF} \sin(\phi / 2)$. On longer time scales, this transformation is expected to lead to an excellent approximation, since the final secular terms involving $\delta_j(t)$ and $D_j(t)$ in Eq. (6-3) are quite small compared to the cycle time of averaging. However, in the case of solids, it is also necessary to overcome the proton-proton couplings which remain after the first rotating frame transformation, necessitating the application of a large RF field amplitude ν_{RF}, given that the phase angle ϕ is constrained to be small by construction. Another difficulty with the second rotating transformation is that the secondary averaging time scale is not necessarily much shorter than the rotor period, which calls the adiabatic assumption with respect to sample rotation into question.

In spite of these difficulties, a second rotating frame transformation illustrates how additional line-narrowing can be obtained [3]. Since it is impossible to satisfy the resonance condition $\nu_p = \nu_{RF} \cos(\phi / 2)$ simultaneously at all points in an inhomogeneous RF coil, there is in general a distribution of small shifts $\Delta\nu_{RF} = \nu_p - \nu_{RF} \cos(\phi / 2)$ from resonance, leading to the following effective Hamiltonian after transformation into the second rotating frame:

$$H_{\text{eff}}(t) = \sum_j \frac{\pi}{2}\left\{\frac{\delta_j^2(t)+D_j^2(t)}{2\nu_{RF}^2\sin(\phi/2)\cos(\phi/2)}+\frac{\Delta\nu_p}{\nu_{RF}\sin(\phi/2)}\right\}$$
$$\times\left\{\frac{\delta_j(t)}{\nu_{RF}\cos(\phi/2)}\right\}D_j(t)\cdot 2S_zI_{yj}+\frac{1}{4}\sum_{i<j}A_{ij}(t)\left\{2I_{yi}I_{yj}-I_{xi}I_{xj}-I_{zi}I_{zj}\right\} \qquad (6\text{-}4)$$
$$+\frac{2}{\pi}\nu_{RF}\sin(\phi/2)I_y\ .$$

For sufficiently large $\nu_{RF} >> |\delta_j(t)|, |D_j(t)|, |\Delta\nu_{RF}|$, according to Eq. (6-4), the effective coupling is greatly scaled down compared to the CW decoupling result. Although the various spatial factors remain time-dependent in the final expression, time-independent couplings emerge from products such as $\delta_j(t)\cdot D_j(t)$. Upon truncation in the second rotating frame, the homonuclear couplings are also scaled down by an additional factor of $\times -1/2$.

Since it is necessary to partially average the proton-proton interactions along a new direction in the interaction frame, it is expected that the secondary line-narrowing process is most effective in the limit of large RF fields. However, in cases where the homonuclear couplings are weak, greater relative improvements over CW decoupling are expected in the regime of reduced decoupling power. Lastly, the breakdown of the adiabatic assumption under fast spinning implies that explicit calculations are necessary in order to assess the efficacy of line-narrowing by simple phase modulation techniques. In the applications presented here, the characteristic cycling frequency $(2/\pi)\nu_{RF}\sin(\phi/2)$ in the second rotating frame is on the order of 10-20 kHz, i. e. comparable to the oscillation frequencies imposed by MAS, which are as great as $2\nu_R = 24$ kHz at 12 kHz spinning speed.

IV. Numerical Calculations with TPPM Decoupling

Because of the great complexity of the time-dependent spin system under phase-alternated pulses, magic angle spinning, and proton-proton interactions, a model problem is investigated here via numerical simulations in order to understand the spin dynamics. In a rotating sample with realistic parameters, the assumption of adiabaticity leading to Eq. (6-4) is problematic, and the combined effects of homonuclear couplings and sample spinning are difficult to follow analytically. The simplest model problem which exhibits these complications is a representative CH_2 fragment. This model has already found use in the study of CW decoupling in static single crystals at high magnetic field [22]. An appropriate internal spin Hamiltonian is the following:

$$\begin{aligned} H_{\text{int}}(t) &= \delta_1(t)I_{z1} + \delta_2(t)I_{z2} + D_1(t)\cdot 2S_zI_{z1} + D_2(t)\cdot 2S_zI_{z2} \\ &\quad + A_{12}(t)\left\{2I_{z1}I_{z2} - I_{x1}I_{x2} - I_{y1}I_{y2}\right\}, \end{aligned} \tag{6-5}$$

where:

$$\begin{aligned} \delta_1(t) &= 1.0\cos(\omega_R t) + 1.0\cos(2\omega_R t), \\ \delta_2(t) &= 1.0\cos(\omega_R t) + 1.0\cos(2\omega_R t), \\ D_1(t) &= 5.0\cos(\omega_R t) + 5.0\cos(2\omega_R t), \\ D_2(t) &= 5.0\cos(\omega_R t + \pi/2) + 5.0\cos(2\omega_R t + \pi/2), \\ A_{12}(t) &= 10.0\cos(\omega_R t + \pi/4) + 10.0\cos(2\omega_R t + \pi/4). \end{aligned} \tag{6-6}$$

These parameters for the resonance offsets and dipolar couplings – heteronuclear $D_j(t)$ and homonuclear $A_{12}(t)$ – are reasonably typical of an arbitrary methylene group crystallite orientation with a large ^1H-^1H

interaction. In a real polycrystalline sample, of course, there is an isotropic distribution of crystallite orientations to consider, in addition to many dipolar couplings of longer range, but this simple model is sufficient to provide some basic insights into the combined dynamics of mechanical rotation and RF excitation.

In these calculations, the decoupling field is nominally applied at exact resonance, so there is no time-independent contribution to the resonance offset term. However, the anisotropic fields contribute local fields which reduce the decoupling efficiency. In the rotating system, since it is impossible to be at exact resonance at all times, the transmitter frequency is generally optimized to minimize the linewidth contribution from the isotropic chemical shifts. The free induction decay (FID) of the S spin under the Hamiltonian of Eq. (6-5) is defined as follows:

$$\langle S_x(t)\rangle = \mathrm{Tr}\{U(t,0)\rho(0)U^{-1}(t,0)S_x\}, \tag{6-7}$$

and is calculated by exact numerical evaluation of the time evolution operator $U(t,0)$, followed by application to the density matrix corresponding to initial transverse magnetization $\rho(0) = 2S_x$. No synchronous relationship between the modulations of magic angle spinning and the externally applied RF pulses is assumed, since the experiments are in general performed asynchronously. Consequently, the time evolution operator for the entire FID is calculated. For sufficiently short time steps, the Hamiltonian is taken to be time-independent, and its two 2 by 2 blocks (each corresponding to one value of the quantum number m_S where $m_S = \pm 1/2$), are diagonalized and exponentiated using the Cayley-Klein parameters for the Hamiltonian submatrices [11, 29].

In all cases, the typical RF field amplitude ν_{RF} of 75.76 kHz (corresponding to a 3.3 μs proton $\pi/2$ pulse length) is employed in the calculations. The FID trajectories are shown for two spinning speeds, 2 kHz and 10 kHz, with comparison of the results obtained at 20° and 50° phase modulation angle ϕ. The pulse length τ_p is varied in the neighborhood of its optimum value in order to illustrate the influence of deviations from the ideal setting. Since an error in pulse length behaves almost in the same way as a deviation in the RF field strength, these trajectories also illustrate the consequences of RF inhomogeneity within this simple model. The free induction decays for four pulse lengths τ_p are plotted, and the CW result is illustrated as a solid line in Figures (6-6), (6-7), and (6-8). Since no S spin chemical shift is included in the simulations, the oscillations in the FID are purely the consequence of unwanted dipolar evolution arising from the heteronuclear couplings experienced by the dilute S spin. Perfect decoupling is therefore obtained when $\langle S_x(t) \rangle = 1$ at all times, reflecting no apparent influence from the protons. On the other hand, rapid oscillations in the FID and spurious cycling behavior with large amplitude reflect poor decoupling performance.

The simulations of the model problem are consistent with the observation that the optimal phase modulation angle becomes more sensitive to the spinning speed under fast MAS and that it tends to decrease at higher spinning speeds. In the simulations shown at 2 kHz spinning speed, illustrated in Figures (6-6) and (6-7), the time scale of FID evolution is greatly increased compared to the CW result. With the addition of the proton-proton interaction in Figure (6-7), a reduction in the efficiency of the phase-modulated decoupling sequence is observed, indicating imperfect "spin locking" of the ^{1}H-^{1}H coupling in the second rotating frame. Here, the most

important effect in determining the optimal phase modulation angle ϕ is the improvement with respect to RF inhomogeneity which is achieved by using a greater amplitude in the phase alternation. For practical applications, where an inhomogeneous distribution of field amplitudes is present within the RF coil, a dispersion of pulse lengths is expected within the sample. In Eq. (6-4), the deviation from the ideal phase modulation rate plays the role of a secondary resonance offset in the decoupling effect generated in the second rotating frame. In direct analogy to the case of CW decoupling in the first rotating frame, this line-broadening effect can be reduced by raising the field strength $(2/\pi)\nu_{RF}\sin(\phi/2)$ or by employing a more homogeneous coil.

In the case of vanishing homonuclear interactions, simulations exhibit similar behavior at 10 kHz spinning frequency. However, when the large coupling $A_{12}(t)$ is introduced, as shown in Figure (6-8), the secondary decoupling effect becomes less stable at the larger modulation angle of 50° as spurious oscillations develop with small deviations in the pulse length τ_p. Because of the attenuation of the homonuclear interaction at higher spinning speeds, the result obtained with the smaller phase angle of 20° is better at 10 kHz than at 2 kHz spinning frequencies, although the sensitivity to RF inhomogeneity is somewhat increased for the same reason under rapid sample spinning. In all cases, the ^{1}H-^{1}H couplings degrade the quality of phase-modulation decoupling, although they also reduce the sensitivity of the FID somewhat to the pulse length τ_p and consequently to the RF inhomogeneity.

Figure (6-6). Simulations of the free induction decay in the CH_2 model problem defined by Eqs. (6-5) and (6-6) at 2 kHz spinning speed, omitting the proton-proton interaction. The phase modulation angles are: (a) $\phi = 20°$; (b) $\phi = 50°$. The TPPM trajectories with several values of τ_p (in units of μs) are shown in order to illustrate the sensitivity of the results with respect to the pulse length and deviations in the RF field amplitude.

(a)

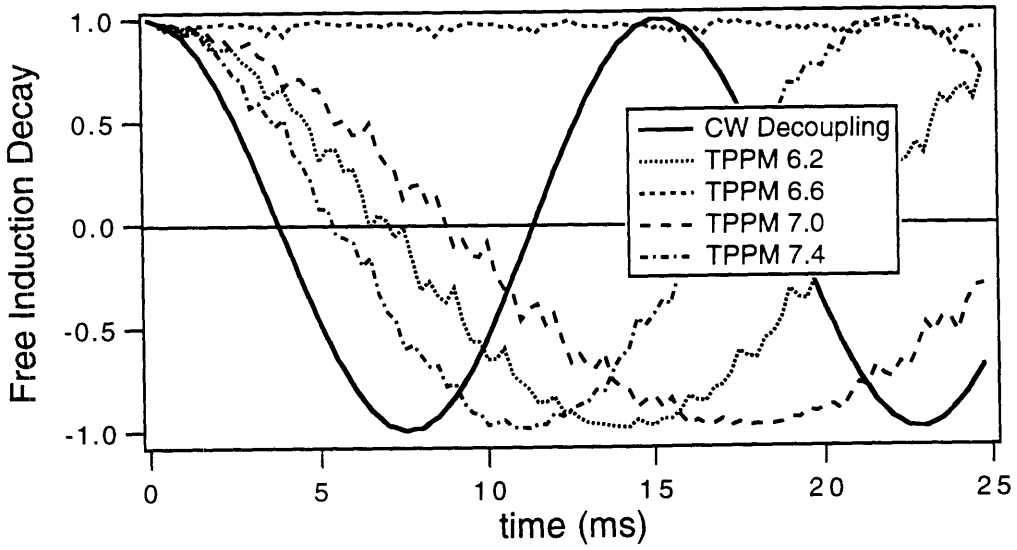
1.0
0.5
0.0
-0.5
-1.0
Free Induction Decay
0
5
10
15
20
25
time (ms)
CW Decoupling
TPPM 6.2
TPPM 6.6
TPPM 7.0
TPPM 7.4

(b)

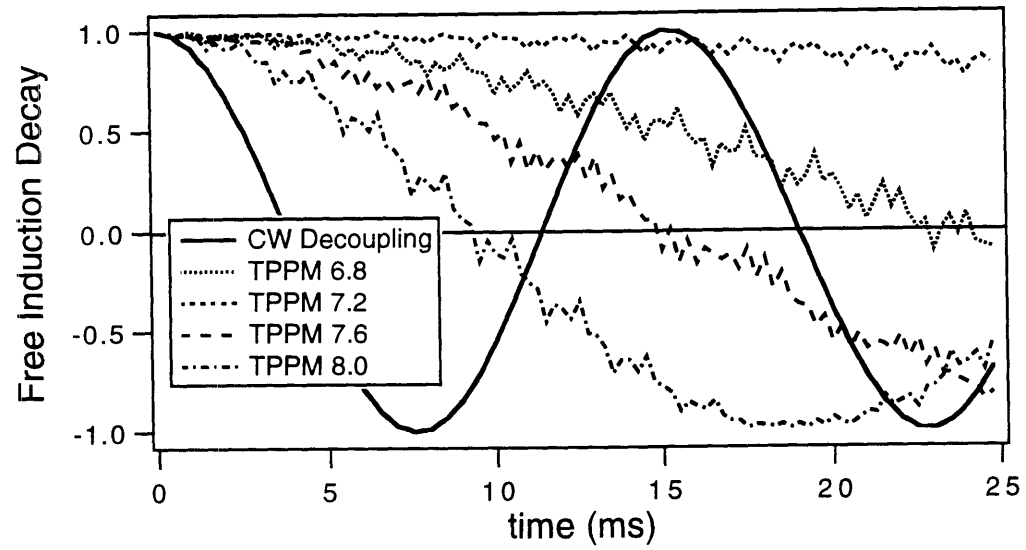
1.0
0.5
0.0
-0.5
-1.0
Free Induction Decay
0
5
10
15
20
25
time (ms)
CW Decoupling
TPPM 6.8
TPPM 7.2
TPPM 7.6
TPPM 8.0

Figure (6-7). Simulations of the free induction decay in the CH_2 model problem defined by Eqs. (6-5) and (6-6) at 2 kHz spinning speed, including the proton-proton interaction. The phase modulations angles are: (a) $\phi = 20°$; (b) $\phi = 50°$. The TPPM trajectories with several values of τ_p (in units of μs) are shown.

(a)

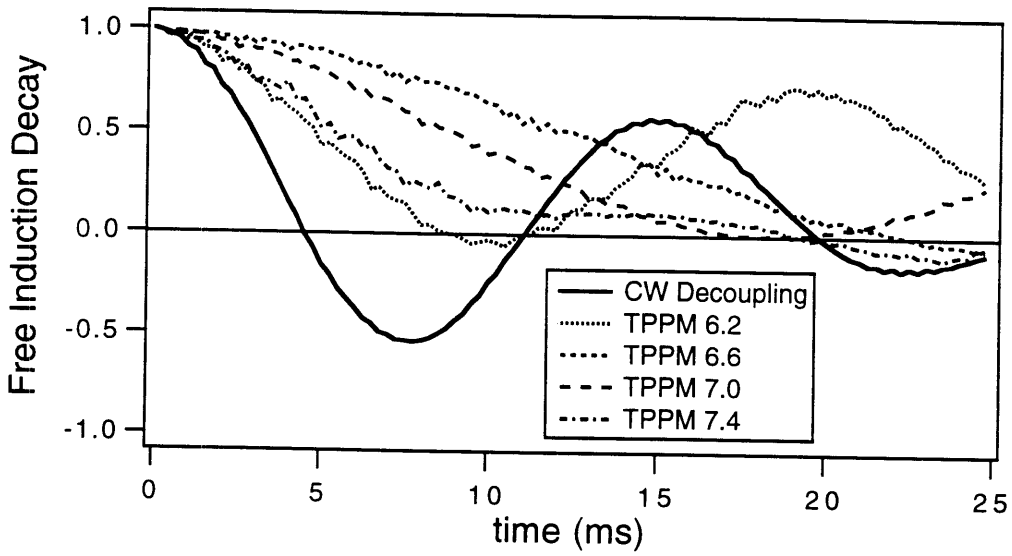
1.0
0.5
0.0
-0.5
-1.0
Free Induction Decay
0
5
10
15
20
25
time (ms)
CW Decoupling
TPPM 6.2
TPPM 6.6
TPPM 7.0
TPPM 7.4

(b)

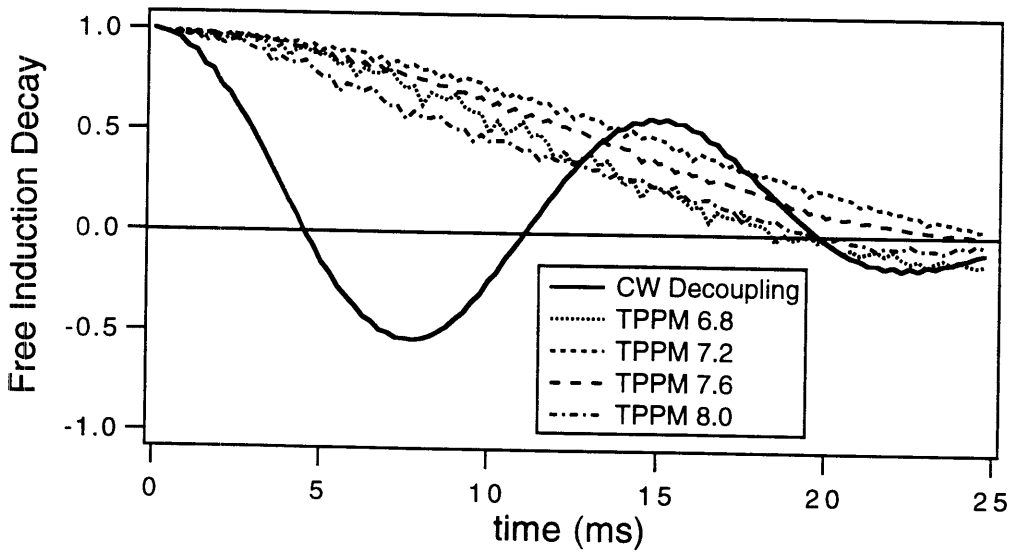
1.0
0.5
0.0
-0.5
-1.0
Free Induction Decay
0
5
10
15
20
25
time (ms)
CW Decoupling
TPPM 6.8
TPPM 7.2
TPPM 7.6
TPPM 8.0

Figure (6-8). Simulations of the free induction decay in the CH_2 model problem defined by Eqs. (6-5) and (6-6) at 10 kHz spinning speed, including the proton-proton interaction. The phase modulations angles are: (a) $\phi = 20°$; (b) $\phi = 50°$. The TPPM trajectories with several values of τ_p (in units of μs) are shown.

(a)

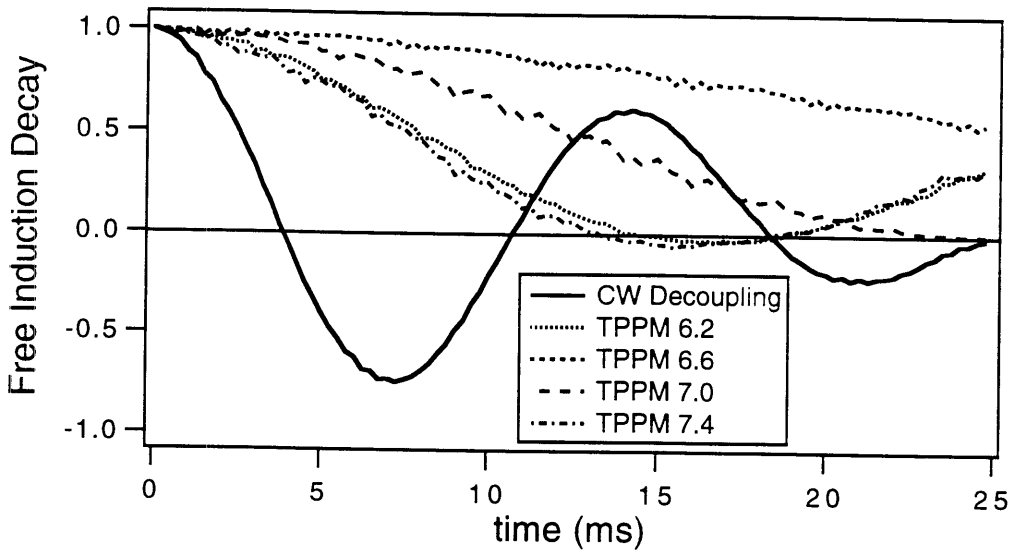
1.0
0.5
0.0
-0.5
-1.0
Free Induction Decay
0
5
10
15
20
25
time (ms)
CW Decoupling
TPPM 6.2
TPPM 6.6
TPPM 7.0
TPPM 7.4

(b)

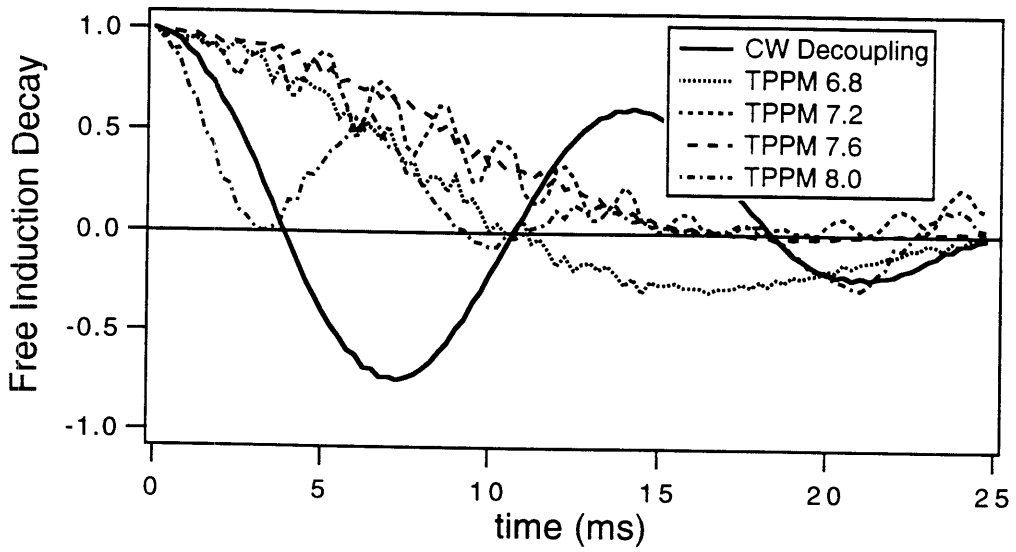
1.0
0.5
0.0
-0.5
-1.0
Free Induction Decay
0
5
10
15
20
25
time (ms)
CW Decoupling
TPPM 6.8
TPPM 7.2
TPPM 7.6
TPPM 8.0

V. Influence of Homonuclear Interactions on Continuous-Wave Decoupling in Rotating Samples

The influence of homonuclear interactions among protons in decoupling experiments on static solid samples has been the subject of much interest [25]. In particular, these couplings are effective in quenching the heteronuclear linewidth either in the presence or absence of a decoupling field, in cases where they dominate the heteronuclear interactions [1]. In static solids, one consequence is that CW decoupling is more efficient than otherwise expected in the presence of resonance offsets, and the change from linear to quadratic linewidth dependence on shifts from resonance is well-known and frequently observed in NMR spectra. This conversion parallels a shift from a lineshape of largely gaussian character (i. e. inhomogeneous) to a more Lorentzian (i. e. homogeneous) functional form, where the flip-flop terms of the homonuclear interactions are treated as agents of random fluctuation in the heteronuclear couplings within a suitable interaction frame [24, 25]. A second consequence of strong homonuclear interactions is that the CW decoupling field strength must exceed not only the heteronuclear linewidth, but also the homonuclear couplings, in order to promote significant additional dipolar line-narrowing.

The application of magic angle spinning modifies this general picture somewhat. To obtain an expression for the approximate spin Hamiltonian with CW decoupling, the angle ϕ is set to zero in Eq. (6-3), and for convenience the "tilted frame" is adopted, where I_{zj} is defined to lie along the RF field direction in the rotating frame:

$$H_{eff}(t) = \nu_{RF} I_z + \sum_j \frac{1}{2\nu_{RF}} \left\{ \delta_j^2(t) + D_j^2(t) \right\} I_{zj} + \sum_j \frac{1}{\nu_{RF}} \delta_j(t) D_j(t) \cdot 2 S_z I_{zj}$$
$$- \frac{1}{2} \sum_{i<j} A_{ij}(t) \left\{ 2 I_{zi} I_{zj} - \frac{1}{2} \left[I_{+i} I_{-j} + I_{-i} I_{+j} \right] \right\} . \qquad (6\text{-}8)$$

With a large separation of time scales between the RF field amplitude ν_{RF} and the spinning frequency ν_R, i. e. $\nu_{RF} >> 2\nu_R$, the effective Hamiltonian of Eq. (6-8) provides an excellent approximation to the low frequency behavior of the system. Without the homonuclear interactions appearing in the fourth term, the approximate Hamiltonian of Eq. (6-8) commutes with itself at different times, and it is therefore inhomogeneous in the MW sense [30]. Consequently, contributions to the small residual coupling in the third term are completely eliminated if they oscillate at some multiple of the spinning speed, even in the slow spinning regime. In computer simulations on the simple model system of an isolated CH group, the spin system appears to evolve only under the static contribution to Eq. (6-8) to an excellent approximation, and this contribution is independent of the spinning speed.

With expansions of the resonance offsets and heteronuclear couplings in their Fourier series, the S spin experiences the following coupling in the absence of homonuclear interactions:

$$H_{coupling}(t) = \sum_j \sum_{m=-2}^{+2} \sum_{n=-2, n\neq 0}^{+2} \frac{1}{\nu_{RF}} \hat{\delta}_j[m] \hat{D}_j[n] \exp\{ i(m+n)\omega_R t \} \cdot 2 S_z I_{zj} , \qquad (6\text{-}9)$$

which can be divided into contributions from the average shift of the transmitter from resonance ($m = 0$) and the anisotropic offsets ($m \neq 0$):

$$H_{coupling}(t) = \sum_j \frac{1}{\nu_{RF}} \hat{\delta}_j[0] \sum_{n=-2,n\neq 0}^{+2} \hat{D}_j[n] \exp\{in\omega_R t\} \cdot 2S_z I_{zj} \,,$$
$$+ \sum_j \sum_{m=-2,m\neq 0}^{+2} \sum_{n=-2,n\neq 0}^{+2} \frac{1}{\nu_{RF}} \hat{\delta}_j[m] \hat{D}_j[n] \exp\{i(m+n)\omega_R t\} \cdot 2S_z I_{zj} \,, \qquad (6\text{-}10)$$

In the inhomogeneous system, the first term disappears completely, since the dipolar coupling is fully amplitude-modulated. However, both static ($m = -n$) and oscillating ($m \neq -n$) residual couplings arise from the second term. The net result is that finite line-broadening arises only from the oscillating resonance offsets, while an overall shift of the transmitter frequency from resonance is expected to have no effect. However, the addition of the homonuclear flip-flop operators $\left[I_{+i}I_{-j} + I_{-i}I_{+j}\right]$ causes the failure of the Hamiltonian of Eq. (6-8) to commute with itself at different times. Since the quality of rotational refocusing is therefore degraded, the homonuclear interactions are expected to increase the line-broadening from the static offsets $\hat{\delta}_j[0]$, which are under experimental control. This situation contrasts fundamentally with the case of static solids, where the homonuclear interactions assist the decoupling field by quenching the heteronuclear interactions. The anisotropic contribution contains both static and oscillating terms, so an overall expectation of the qualitative effect of homonuclear couplings does not emerge directly from Eq. (6-10).

This perspective provides a qualitative framework for understanding the dependence of ^{13}C linewidths on resonance offsets in rotating polycrystalline samples. As the spinning speed is increased, an increase in the linewidths of ^{13}C resonances is generally observed [19, 20, 23], and this effect is generally attributed to a reduction in the favorable influence of the homonuclear couplings [19, 23], although it is possible that rotational interference also

plays a subtle role [20]. These interactions are themselves amplitude-modulated, but their spin Hamiltonian is not self-commuting in general. As a consequence, their influence on the spin dynamics is removed slowly as the spinning speed is increased, and it is eliminated with great efficiency only when the spinning speed significantly exceeds the proton linewidth [30]. With optimization of the transmitter frequency, the homonuclear interactions are a line-narrowing influence on the dilute spins in this commonly accepted picture, but their favorable influence is increasingly attenuated with higher spinning frequencies.

On the other hand, it is clear *a priori* that homonuclear interactions have the opposite effect in the case of static shifts from resonance. They are detrimental to the efficient decoupling of the isotropic contribution to the resonance offset effect. Consequently, the sensitivity of ^{13}C linewidths to the transmitter offsets $\hat{\delta}_j[0]$ is reduced in principle as the spinning speed is increased (in the fast MAS limit). In calcium formate, the protons are relatively isolated from each other, and their homogeneous linewidth (FWHM) is only $\approx$ 2 kHz at 4.3 kHz spinning speed in the 100% ^{13}C-labeled sample. Figure (6-9) illustrates the relative insensitivity of the ^{13}C centerband lineshape to small transmitter offsets and the increasingly inhomogeneous character obtained at higher spinning speeds. As the spinning speed is increased from 4 kHz to 8 kHz, the splitting between the two non-equivalent formate ions becomes unresolved, yet the lineshape becomes almost insensitive to small resonance offsets.

In the case of the methylene resonance, the sensitivity of the linewidths to transmitter frequency shown in Figure (6-10) is well-described by quadratic functions at both 2 and 10 kHz spinning speeds – the fitted curves are also plotted – while the curvature is greatly reduced at higher spinning

speeds (i. e. ≥ 5 kHz). Simultaneously, at least for all spinning speeds ≤ 10 kHz, the TPPM approach yields further improvements in the resonance offset tolerance of the ^{13}C lineshapes. In these experiments, however, although the offset dependence of the TPPM lineshapes is also well-described by a quadratic functional form, the curvature increases somewhat with spinning speed.

The paradox that the optimized linewidth grows larger with increasing spinning speed, while at the same time the offset sensitivity decreases, is observed here in both the cases of strong and weak ^1H-^1H interactions. Although it is very difficult to estimate the simultaneous influences of MAS and ^1H-^1H quantitatively in a many-body system of coupled spin-1/2 nuclei, the considerations discussed here are the most likely explanations for these general trends.

Figure (6-9). Experimental lineshapes of the 100% ^{13}C-labeled calcium formate centerband as a function of the transmitter frequency in increments of 2 kHz from the optimal setting at 4 kHz (bottom) and 8 kHz spinning speeds (top) at 100 MHz Larmor frequency for ^{13}C. The RF field strength is 65.8 kHz. At 4 kHz spinning frequency, the 80 Hz splitting between the non-equivalent ions in the crystal structure is partially resolved under optimal conditions.

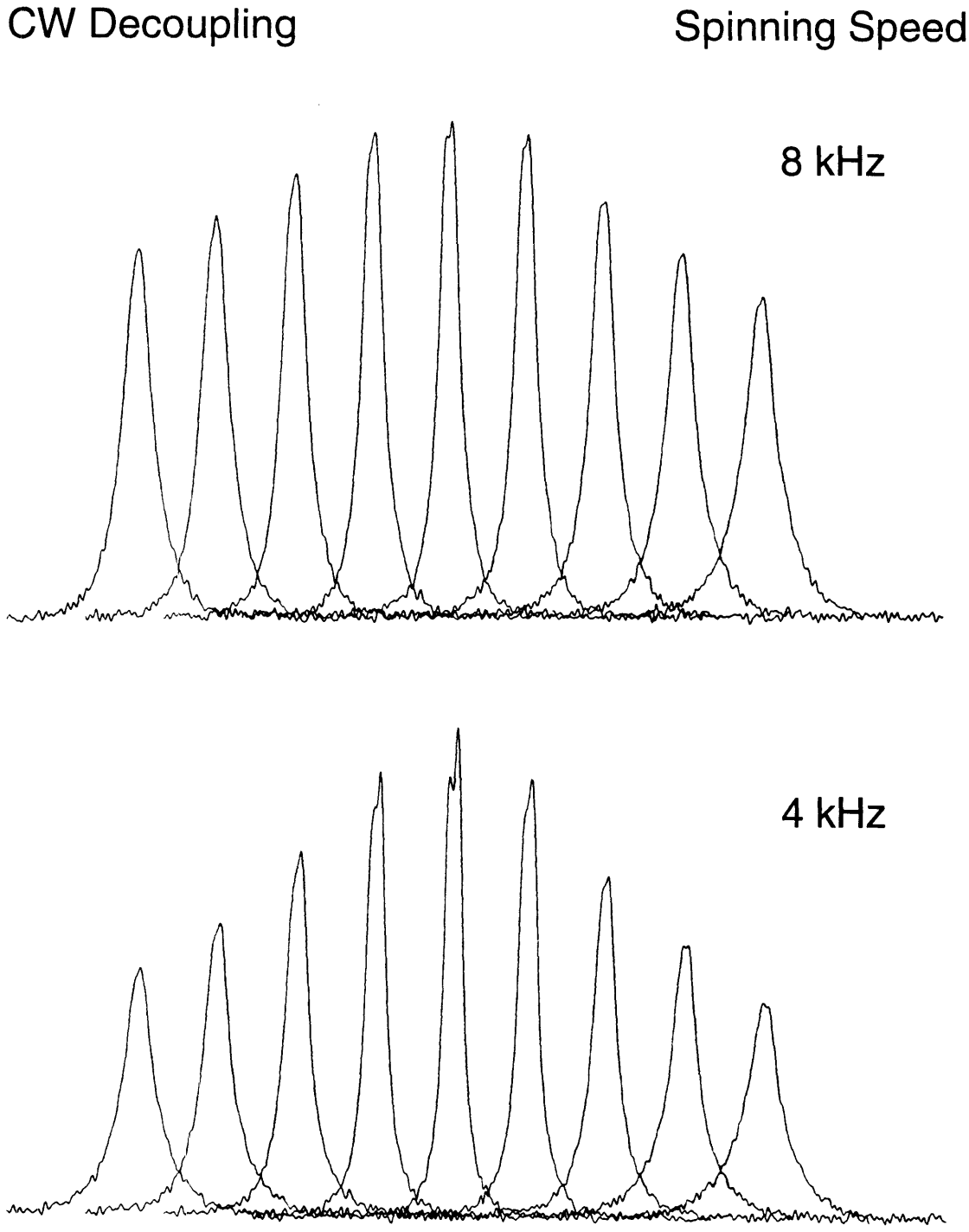
CW Decoupling
Spinning Speed
8 kHz
4 kHz

Figure (6-10). Linewidths of the 4-CH_2 resonance of 1,4-^{13}C-4-^{15}N-glycylglycine hydrochloride monohydrate as a function of the relative frequency of the ^{1}H transmitter at (a) 2 kHz and (b) 10 kHz spinning speeds under both CW and TPPM decoupling. The RF field strength is 73.5 kHz. The TPPM parameters are $\tau_p = 6.2\mu s$, $\phi = 45°$ at 2 kHz; and $\tau_p = 6.0\mu s$, $\phi = 15°$ at 10 kHz spinning speeds. Up to at least 10 kHz, the offset dependences fit a quadratic function quite well for both CW and TPPM decoupling. From 2, 4, 6, 8, to 10 kHz spinning speeds, respectively, the curvature of the FWHM dependence on the offset decreases as follows: 12.9, 7.4, 6.1, 5.3, 4.8 Hz/kHz^2 for CW decoupling; and increases as follows: 1.4, 1.7, 2.2, 2.2, 2.4 Hz/kHz^2 for TPPM decoupling. The inhomogeneous contribution to the methylene linewidths is approximately 35 ± 5 Hz.

(a)

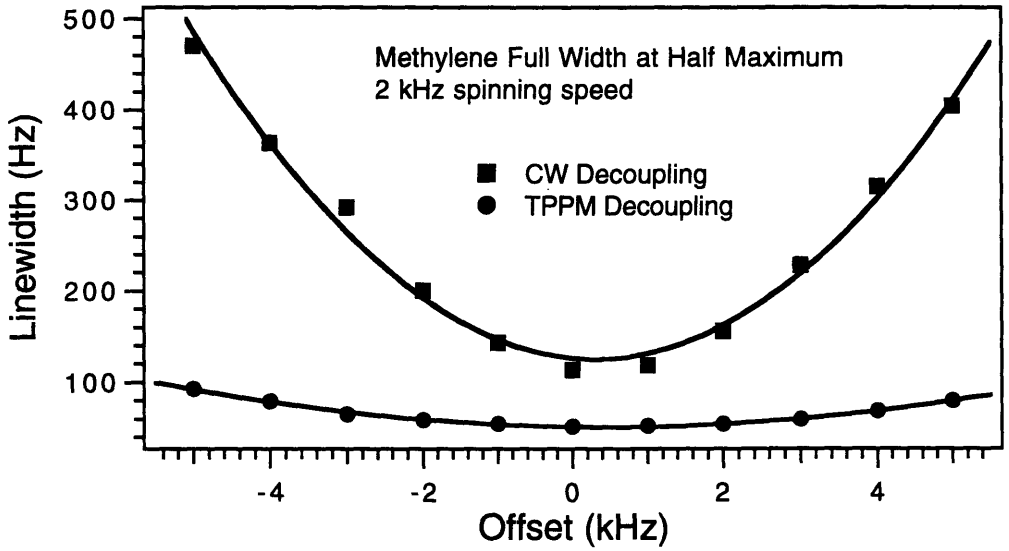
Methylene Full Width at Half Maximum
2 kHz spinning speed
CW Decoupling
TPPM Decoupling
Linewidth (Hz)
500
400
300
200
100
-4
-2
0
2
4
Offset (kHz)

(b)

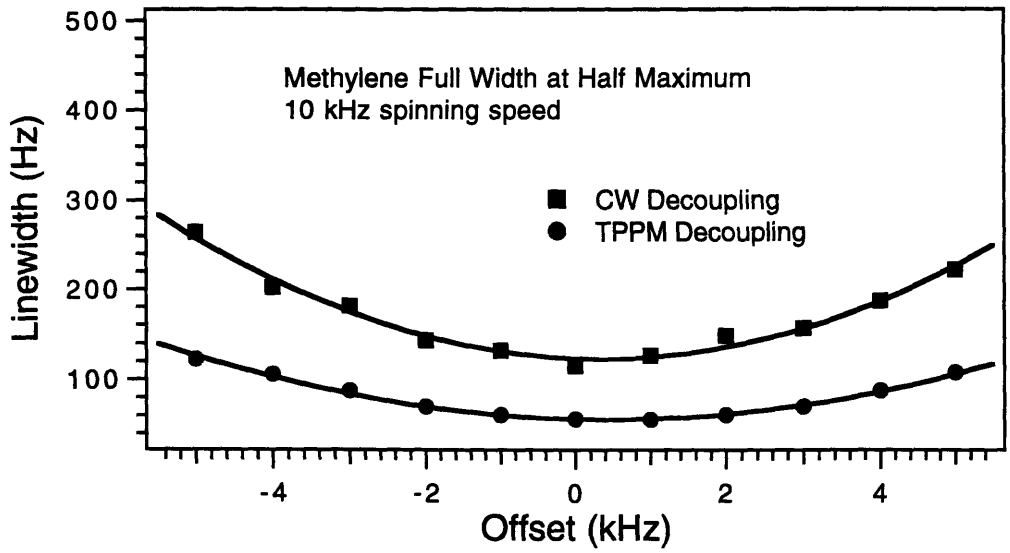
Methylene Full Width at Half Maximum
10 kHz spinning speed
CW Decoupling
TPPM Decoupling
Linewidth (Hz)
500
400
300
200
100
-4
-2
0
2
4
Offset (kHz)

VI. Rotational Interference Effects in Composite Pulse Decoupling

The COMARO-2 sequence consists of the following supercycle of composite 90° pulses: $XYXYXY\ X\bar{Y}X\bar{Y}X\bar{Y}$ [4, 6]. Each net 90° rotation is comprised of the composite rotation 385° $\overline{320}$° 25°, which operates via the approximate coherent averaging of Zeeman-like terms in the spin Hamiltonian through zeroth and first orders [31]. Consequently, the removal of the heteronuclear dipole-dipole coupling accompanies each net 90° rotation with simultaneous compensation for resonance offset effects. The supercycle leads to the coherent averaging of the homonuclear couplings, and further reduction in the heteronuclear couplings, on a longer time scale. For these reasons, the sequence provides decoupling which is robust with respect to large heteronuclear and homonuclear couplings, and which at the same time provides tolerance to large resonance offsets. Therefore, for solids and liquid crystals, it is more suitable than other compensated sequences which have been developed for solution NMR spectroscopy [3] based on composite pulses [32]. With the addition of magic angle spinning, however, the performance of this sequence and similar ones is degraded because of rotational interference effects [5, 16]. This problem has motivated the development of sequences based on simpler excitations [17, 19]. A typical example is the methylene group of sodium propionate. While the ^{13}C linewidth is 196 Hz at 4.9 kHz spinning speed with a CW decoupling field of 73.5 kHz on resonance, only 397 Hz is obtained with COMARO-2 at 100 MHz Larmor frequency for ^{13}C.

Figure (6-11) illustrates how the model CH_2 crystallite discussed earlier behaves under the COMARO-2 sequence. Without the ^1H-^1H interaction, highly efficient decoupling is obtained even with deviations of ±5% in the nominal RF field strength. However, the addition of the homonuclear

coupling leads to a low frequency cycling sideband whose amplitude is unstable with respect to small deviations in the RF field. It is therefore the combination of MAS and the homonuclear interactions which causes degradation of decoupling performance.

Because the homonuclear couplings are weak in calcium formate, its COMARO-2 linewidths compare more favorably to those obtained with CW decoupling. Figure (6-12) shows how COMARO-2 is able to resolve the small splitting in the ^{13}C spectrum at several spinning speeds. The broadening at the base reflects the inhomogeneous distribution of cycling sidebands at low frequency which accompany long composite pulse sequences in rotating samples. For the relatively isolated CH moiety, sharply defined destructive interference between the RF and MAS modulations occurs at resonance conditions where the time scales of the two excitations are approximately synchronized. In the spectra shown in Figure (6-11), the ^{1}H RF field strength is 65.8 kHz, yielding a cycle time of $\tau_C = 369.9\ \mu s$ for the COMARO-2 sequence. The sample rotation induces maximum deterioration of the lineshape at 8 kHz, where the condition $\tau_C \approx 3\tau_R$ is approximately satisfied. The corresponding TPPM lineshapes acquired with $\tau_p = 9.5\ \mu s$ and $\phi = 90°$ are also shown. Apart from the result at 10 kHz spinning speed, for which the phase angle ϕ is too large, the splitting is greatly enhanced without the additional undesirable perturbations in the ^{13}C spectrum.

Figure (6-13) demonstrates the experimental and simulated spectra obtained with precise synchronization of MAS and the decoupling pulse cycle. The simulated lineshapes are obtained from exact calculations of the isolated CH pair with parameters appropriate for calcium formate. For this system, the ^{13}C and ^{1}H CSA tensors, including their orientations in the molecular frame, are known from single crystal studies [33-35]. An additional 45 Hz of

exponential line-broadening is added to the simulated free induction decays in order to compare them directly with the experimental spectra. Line-broadening resulting from the ^{1}H CSA interaction, which contributes oscillatory resonance offsets, is predicted by the CW simulation. Similar simulations omitting this interaction predict an essentially vanishing linewidth. With COMARO-2 decoupling, the regeneration of powder spectra resulting from rotational interference is also demonstrated. The ^{1}H CSA interaction is not necessary to predict this behavior because the coherent averaging of the heteronuclear coupling itself is partially spoiled by the interplay between MAS and the phase modulated RF field.

The numerical calculations do not include several important effects, including imperfections in the application of the sequence (particularly the RF inhomogeneity), weak homonuclear interactions, and heteronuclear couplings of longer range. These factors contribute additional perturbations to the observed lineshapes. In spite of these difficulties, the total centerband FWHM values from the experiments, 200 Hz for CW and 417 Hz for COMARO-2, are reflected reasonably well by the somewhat larger simulated values of 286 Hz and 456 Hz with the two techniques, respectively. More generally, the simulated CW lineshape is virtually insensitive to the spinning speed, since ^{1}H-^{1}H interactions are not included.

Figure (6-11). Simulations of the free induction decay in the CH_2 model problem defined by Eqs. (6-5) and (6-6) at 2 kHz spinning speed with the COMARO-2 decoupling scheme: (a) without the proton-proton interaction, and (b) with the proton-proton interaction. The CW results are also shown for comparison, as well as the COMARO-2 trajectories with the nominal RF field of 75.76 kHz, and deviations in it corresponding to $75.76 \pm 5\%$ kHz. In the context of MAS, the ^1H-^1H interaction and the RF inhomogeneity lead jointly to instability in the quality of heteronuclear decoupling.

(a)

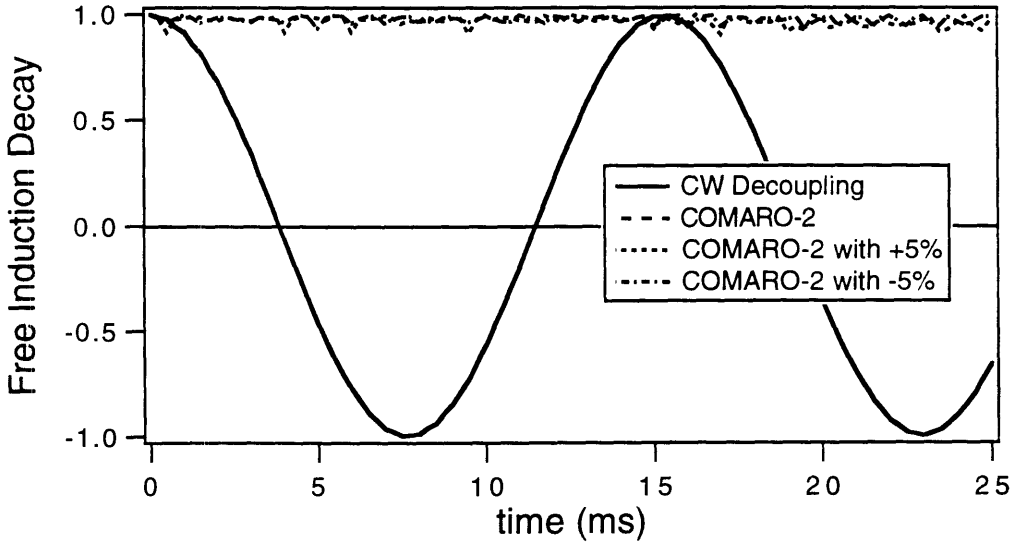
1.0
0.5
0.0
-0.5
-1.0
Free Induction Decay
0
5
10
15
20
25
time (ms)
CW Decoupling
COMARO-2
COMARO-2 with +5%
COMARO-2 with -5%

(b)

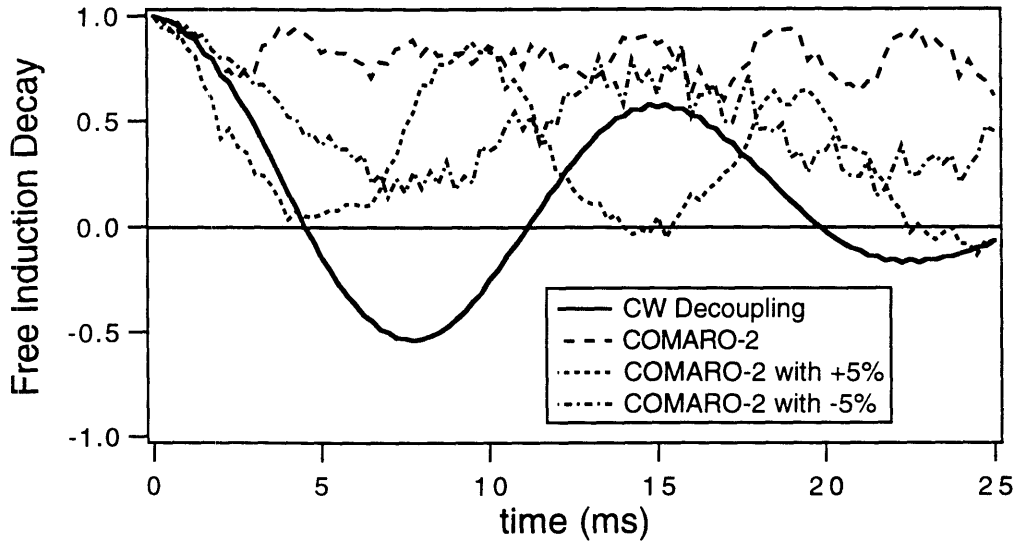
1.0
0.5
0.0
-0.5
-1.0
Free Induction Decay
0
5
10
15
20
25
time (ms)
CW Decoupling
COMARO-2
COMARO-2 with +5%
COMARO-2 with -5%

Figure (6-12). Experimental ^{13}C centerband lineshapes of 100% ^{13}C-labeled calcium formate with an ^{1}H decoupling field strength of 65.8 kHz applied on resonance. Spectra at several spinning speeds are shown with CW, COMARO-2, and TPPM decoupling. The TPPM cycle is implemented with the parameters: $\tau_p = 9.5\ \mu s$ and $\phi = 90°$. The reduced centerband intensity in the slow spinning regime results mostly from the dispersion of spectral intensity among the sidebands arising from the ^{13}C CSA interaction, which is not shown. In these experiments, pulses can only be set within 0.1 μs, so the elements of the 90° composite pulse are rounded to the closest appropriate value.

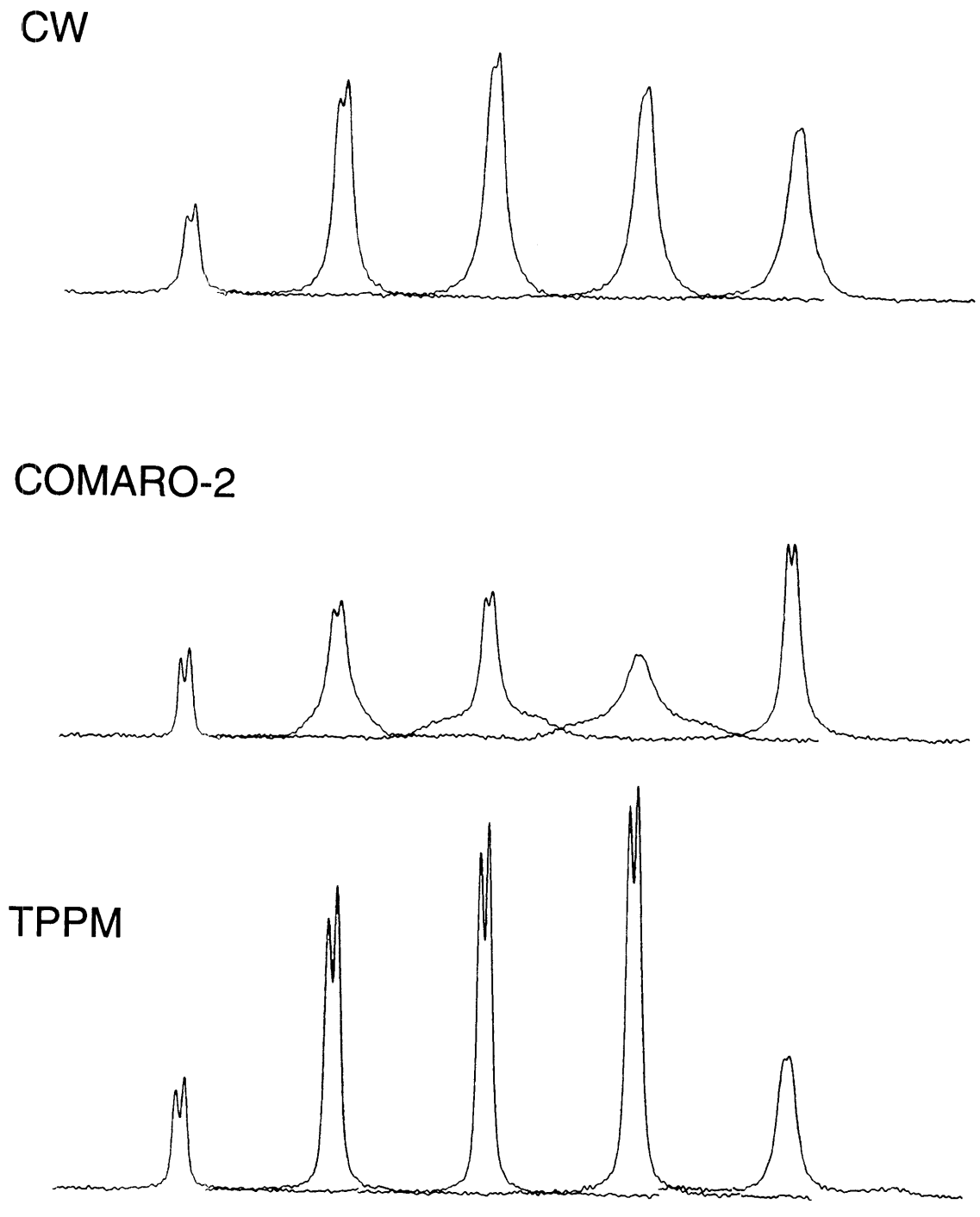
CW
COMARO-2
TPPM
2 kHz
4 kHz
6 kHz
8 kHz
10 kHz
Spinning Speed

Figure (6-13). Simulated and experimental MAS spectra of calcium formate comparing CW and COMARO-2 decoupling performance under rotor synchronization at 2.622 kHz spinning speed with a 64.1 kHz RF field. The simulations include all parameters for the isolated heteronuclear two spin system with CSA and dipolar parameters for calcium formate. The finite line-broadening under CW decoupling and the degradation of the COMARO-2 lineshapes are predicted. An additional 45 Hz of exponential line-broadening is added to the simulated spectra prior to Fourier transformation in order to account for the estimated linewidth from sources other than insufficient decoupling. In the computer simulation of CW decoupling performance, the 80 Hz splitting is not resolved.

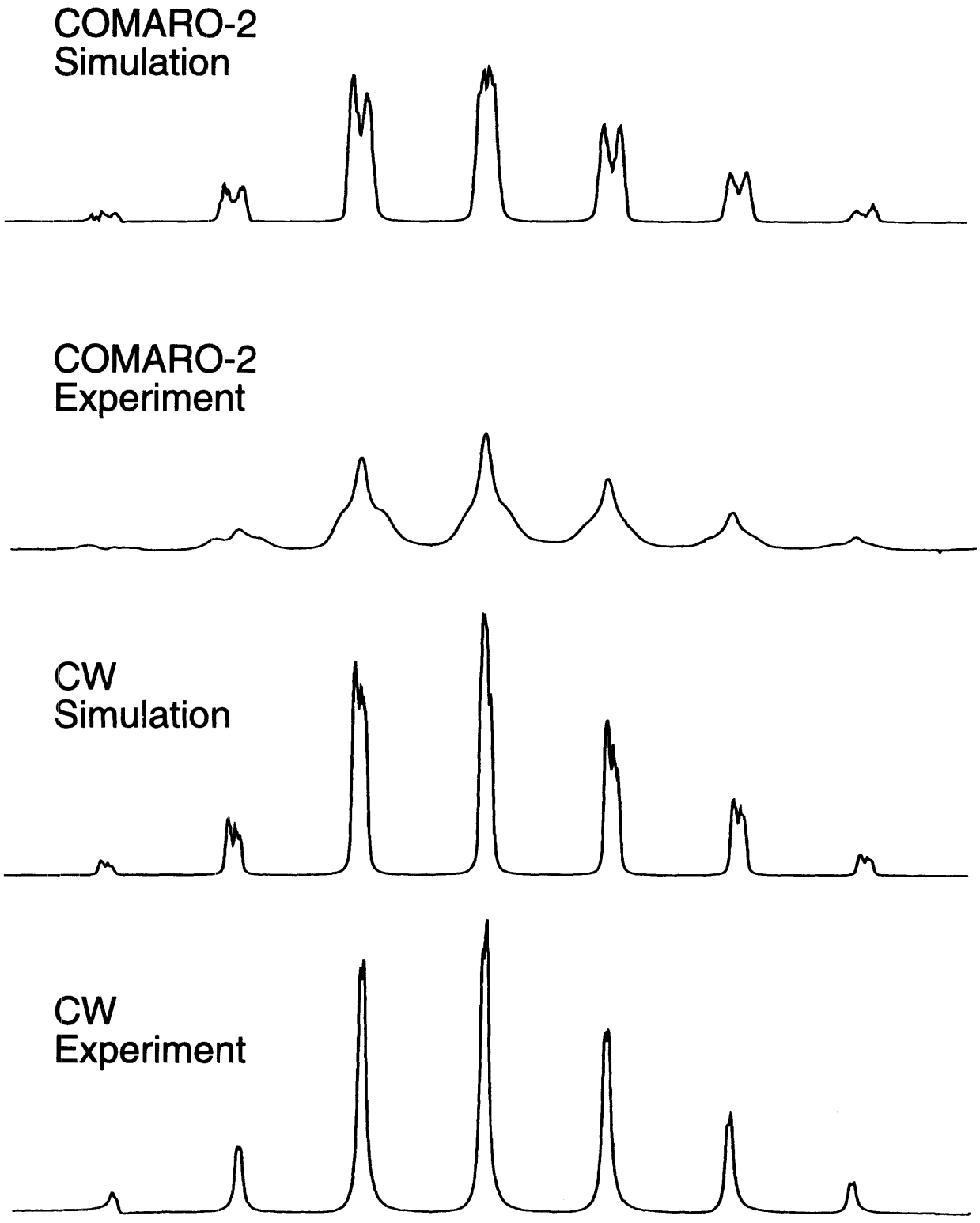
COMARO-2
Simulation
COMARO-2
Experiment
CW
Simulation
CW
Experiment

VII. Conclusion

In our examples, the advantage of the TPPM approach relative to CW decoupling persists even when strong proton-proton couplings are present in the spin system, although these interactions impede the efficiency of the method to some extent. The theoretical treatment of TPPM decoupling predicts that the relative improvement over CW irradiation increases as the RF field strength is raised. Greater improvement is expected for shorter ^1H pulse widths, while at sufficiently low decoupling power levels, no enhancement is expected because of insufficient decoupling field amplitude in the second rotating frame, where the homonuclear linewidth is scaled down further only by $\times -1/2$. In the first rotating frame, it is well-known that a certain minimum level of RF power (20-40 kHz in many organic molecules [1]) is necessary in order to overcome the proton linewidth. These considerations imply that the optimum angle ϕ is a compromise between the favorable effects of large modulation angle on the ^1H-^1H interactions and the RF inhomogeneity, on the one hand, and the constraint that ϕ be a small angle, on the other.

Unfortunately, the addition of MAS complicates this simple picture. Although the TPPM sequence has a short cycle time, it already exhibits cycling sideband behavior in the low frequency regime, ranging from 5-20 kHz in the applications described here. Furthermore, the homonuclear couplings serve to disperse the pattern of cycling sidebands and create additional opportunities for destructive interference with the sample rotation at frequencies $\omega_R / 2\pi$ and $2 \cdot \omega_R / 2\pi$, effects which degrade the decoupling efficiency. In the case of single phase RF irradiation with a weak field, cancellation of the CW decoupling effect via this interference behavior has

been observed at the "rotary resonance conditions" $\nu_{RF} = n\omega_R / 2\pi$ [20, 36]. In the applications of TPPM decoupling to the methylene group examined here, the best FWHM at high spinning speeds is obtained with a somewhat smaller phase modulation angle than in the slow spinning regime because of rotational interference. More generally, sample rotation reduces the efficiency of the averaging process obtained with composite pulse sequences such as COMARO-2, resulting in poor methylene linewidths and distorted lineshapes for the more simple case of an isolated heteronuclear spin pair.

In all of the cases examined so far, the contribution to the ^{13}C linewidth from inefficient proton decoupling is greatly reduced with the TPPM approach. This approach is therefore expected to find general utility in CPMAS experiments on diamagnetic polycrystalline samples, especially in the regime of high magnetic field where the resonance offset effect is increased. In high magnetic fields, it is also advantageous to employ rapid sample spinning in order to reduce the sideband intensities which arise from the CSA, whose magnitude scales linearly with the magnetic field. TPPM decoupling leads to the largest enhancements in this regime, where CW decoupling becomes increasingly inefficient with respect to anisotropic resonance offsets. Greater improvements are also expected with more homogeneous RF coils, particularly at high spinning speeds. The spectra presented here, however, exhibit substantial improvements in ^{13}C spectra with RF inhomogenities of approximately 5-10%.

The compounds discussed here are all diamagnetic organic solids. Although the range of resonance offset compensation is small in this implementation of coherent phase modulation decoupling, the TPPM sequence is also potentially advantageous for application to MAS experiments on moderately paramagnetic solids [16-18], since the sequence is readily

optimized to avoid destructive interference effects and exhibits robust decoupling performance in the presence of large heteronuclear couplings.

References for Chapter 6.

[1] D. L. VanderHart, W. L. Earl, and A. N. Garroway, J. Mag. Res. **44**, 361 (1981).

[2] A. N. Garroway, D. L. VanderHart, and W. L. Earl, Philo. Trans. Roy. Soc. London A **299**, 609 (1981).

[3] A. J. Shaka and J. Keeler, Prog. in NMR Spectroscopy **19**, 47 (1987).

[4] D. Suter, K. V. Schenker, and A. Pines, J. Mag. Res. **73**, 90 (1987).

[5] D. Suter, A. Pines, J. H. Lee, and G. Drobny, Chem. Phys. Lett. **144**, 324 (1988).

[6] K. V. Schenker, D. Suter, and A. Pines, J. Mag. Res. **73**, 99 (1987).

[7] M. H. Levitt and R. Freeman, J. Mag. Res. **43**, 502 (1981).

[8] J. S. Waugh, J. Mag. Res. **49**, 517 (1982).

[9] T. Fujiwara, T. Anai, N. Kurihara, and K. Nagayama, J. Mag. Res. A **104**, 103 (1993).

[10] A. J. Shaka, J. Keeler, T. Frenkiel, and R. Freeman, J. Mag. Res. **52**, 335 (1983).

[11] J. S. Waugh, J. Mag. Res. **50**, 30 (1982).

[12] M. H. Levitt, R. Freeman, and T. Frenkiel, J. Mag. Res. **50**, 157 (1982).

[13] M. R. Bendall, J. Mag. Res. A **112**, 126 (1995).

[14] W. A. Anderson and R. Freeman, J. Chem. Phys. **37**, 85 (1962).

[15] W. A. Anderson and F. A. Nelson, J. Chem. Phys. **39**, 183 (1963).

[16] T. K. Pratum, J. Mag. Res. **88**, 384 (1990).

[17] T. K. Pratum, Chem. Phys. Lett. **172**, 291 (1990).

[18] D. P. Raleigh, C. P. Grey, N. Soffe, and C. M. Dobson, J. Mag. Res. **97**, 1621 (1992).

[19] P. Tekely, P. Palmas, and D. Canet, J. Mag. Res. A **107**, 129 (1994).

[20] T. Nakai and C. A. McDowell, Chem. Phys. Lett. **227**, 639 (1994).

[21] A. E. Bennett, M. Auger, and K. V. Lakshmi, unpublished results (1991).

[22] U. Haeberlen, NMR Basic Principles and Progress **25**, 143 (1990).

[23] I. J. Shannon, K. D. M. Harris, and S. Arumugam, Chem. Phys. Lett. **196**, 588 (1992).

[24] G. Sinning, M. Mehring, and A. Pines, Chem. Phys. Lett. **43**, 382 (1976).

[25] M. Mehring, *Principles of High Resolution NMR in Solids* (Springer-Verlag, Berlin Heidelberg NewYork, 1983).

[26] R. Richarz and H. Sauter, J. Mag. Res. **52**, 308 (1983).

[27] J. B. Grutzner and A. E. Santini, J. Mag. Res. **19**, 178 (1975).

[28] E. T. Olejniczak, S. Vega, and R. G. Griffin, J. Chem. Phys. **81**, 4804 (1984).

[29] J. J. Sakurai and S. F. Tuan, *Modern Quantum Mechanics* (Benjamin/ Cummings Publishing, Menlo Park, 1985).

[30] M. Maricq and J. S. Waugh, J. Chem. Phys. **70**, 3300 (1979).

[31] R. Tycko, H. M. Cho, E. Schneider, and A. Pines, J. Mag. Res. **61**, 90 (1985).

[32] M. H. Levitt, Prog. NMR Spectroscopy **18**, 61 (1986).

[33] J. L. Ackerman, J. Tegenfeldt, and J. S. Waugh, J. Am. Chem. Soc. **96**, 6843 (1974).

[34] H. Post and U. Haeberlen, J. Mag. Res. **40**, 17 (1980).

[35] T. Watanabe and M. Matsui, Acta. Cryst. B **34**, 2731 (1978).

[36] T. G. Oas, R. G. Griffin, and M. H. Levitt, J. Chem. Phys. **89**, 692 (1988).